The APEX Large CO Heterodyne Orion Legacy Survey (ALCOHOLS) ⋆

I. Survey overview

Th. Stanke[1], H. G. Arce[2], J. Bally[3], P. Bergman[4], J. Carpenter[5], C. J. Davis[6], W. Dent[5], J. Di Francesco[7,12], J. Eislöffel[8], D. Froebrich[9], A. Ginsburg[10], M. Heyer[11], D. Johnstone[7,12], D. Mardones[13], M. J. McCaughrean[14], S. T. Megeath[15], F. Nakamura[16], M. D. Smith[17], A. Stutz[18], K. Tatematsu[19], C. Walker[20], J. P. Williams[21], H. Zinnecker[22], B. J. Swift[20], C. Kulesa[20], B. Peters[20], B. Duffy[20], J. Kloosterman[23], U. A. Yıldız[24], J. L. Pineda[24], C. De Breuck[1], and Th. Klein[25]

(Affiliations can be found after the references)

ABSTRACT

Context. The Orion molecular cloud complex harbours the nearest Giant Molecular Clouds (GMCs) and the nearest site of high-mass star formation. Its young star and protostar populations are thoroughly characterized. The region is therefore a prime target for the study of star formation.
Aims. Here, we verify the performance of the SuperCAM 64 pixel heterodyne array on the Atacama Pathfinder Experiment (APEX). We give a descriptive overview of a set of wide-field CO(3-2) spectral line cubes obtained towards the Orion GMC complex, aimed at characterizing the dynamics and structure of the extended molecular gas in diverse regions of the clouds, ranging from very active sites of clustered star formation in Orion B to comparatively quiet regions in southern Orion A. In a future publication, we will characterize the full population of protostellar outflows and their feedback over an entire GMC.
Methods. We present a 2.7 square degree (130 pc^2) mapping survey in the $^{12}CO(3-2)$ transition, obtained using SuperCAM on APEX at an angular resolution of 19″ (7600 AU or 0.037 pc at a distance of 400 pc), covering the main sites of star formation in the Orion B cloud (L 1622, NGC 2071, NGC 2068, Ori B9, NGC 2024, and NGC 2023), and a large patch in the southern part of the L 1641 cloud in Orion A.
Results. We describe CO integrated line emission and line moment maps and position-velocity diagrams for all survey fields and discuss a few sub-regions in some detail. Evidence for expanding bubbles is seen with lines splitting into double components, often in areas of optical nebulosities, most prominently in the NGC 2024 H II region, where we argue that the bulk of the molecular gas is in the foreground of the H II region. High CO(3-2)/CO(1-0) line ratios reveal warm CO along the western edge of the Orion B cloud in the NGC 2023/NGC 2024 region facing the IC 434 H II region. We see multiple, well separated radial velocity cloud components towards several fields and propose that L 1641-S consists of a sequence of clouds at increasingly larger distances. We find a small, seemingly spherical cloud, which we term 'Cow Nebula' globule, north of NGC 2071. We confirm that we can trace high velocity line wings out to the 'extremely high velocity' regime in protostellar molecular outflows for the NGC 2071-IR outflow and the NGC 2024 CO jet, and identify the protostellar dust core FIR4 (rather than FIR5) as the true driving source of the NGC 2024 monopolar outflow.

Key words. ISM: clouds – ISM: kinematics and dynamics – ISM: structure – ISM: bubbles – ISM: jets and outflows – Submillimeter: ISM

1. Introduction

At a distance of 400-500 pc (e.g. Menten et al. 2007; Kounkel et al. 2017; Großschedl et al. 2018; Zucker et al. 2019), the Orion molecular cloud complex harbours the most nearby Giant Molecular Clouds (GMCs) (for an overview see, e.g. Genzel & Stutzki 1989; Bally 2008). The Orion A GMC, in particular, is home to the nearest site of high-mass star formation in the BN/KL complex in the OMC-1 core behind the Orion Nebula H II region. OMC-1 is at the heart of the very dense 'integral-shaped filament', featuring very active low- to intermediate-mass star formation. The L 1641 dark cloud extends over several degrees to the south-east of the Orion Nebula and shows mostly low-mass star formation. Orion B shows star formation mainly concentrated in a few moderate-sized clusters with young stars up to intermediate masses. Orion A and B thus provide the op-

portunity to study star formation in a single cloud complex over a range of environments, from regions directly impacted by massive star formation and H II regions, over moderate-sized clusters, to very quiet regions with mostly isolated star formation.

The CO molecule arguably is the best tracer of the bulk of the molecular gas in clouds due to its high abundance and the low critical densities of its lower-J rotational transitions. Numerous studies presented wide-field observations of CO emission in Orion. Following the first detection in space of CO in the (1-0) transition in the Orion Nebula region by Wilson et al. (1970), the pioneering works of Kutner et al. (1977) and Maddalena et al. (1986) mapped out the overall extent of the Orion GMCs, while Bally et al. (1987) presented the first attempt of resolving the internal spatio-kinematical structure of the Orion A GMC in $^{13}CO(1-0)$. The first attempt at wide-field mapping in the region in the ^{12}CO and $^{13}CO(3-2)$ lines was presented by Kramer et al. (1996), covering the NGC 2023 and NGC 2024 regions in Orion B, including the Horsehead Nebula B33. Further wide field lower-J CO studies in Orion include Castets et al. (1990),

Sakamoto et al. (1994), Nagahama et al. (1998), Aoyama et al. (2001), Wilson et al. (2005), and Nishimura et al. (2015), while a complete coverage of Orion A in the CO(4-3) line has been presented by Ishii et al. (2016).

Recent advancements in receiver technology (sensitivity, bandwidth, multi-pixel heterodyne array receivers) now allow (multi)square degree sized maps to be made on larger telescopes with significant sub-arcminute spatial resolution (e.g. Sakamoto et al. 1997; Shimajiri et al. 2011; Nakamura et al. 2012; Ripple et al. 2013; Berné et al. 2014; Pety et al. 2017; Ishii et al. 2019; Nakamura et al. 2019). In terms of spatial resolution combined with large area coverage, the ^{12}CO, ^{13}CO, and C^{18}O(1-0) survey by Kong et al. (2018), combining CARMA interferometric observations with NRO 45 m observations using the BEARS and FOREST heterodyne receiver arrays, has set new standards, covering 2 square degrees at 7″ spatial resolution. Still, these surveys remain largely limited to the lowest-J transitions, that is the (1-0) and (2-1) lines, due to the challenges posed by performing extensive observations at sub-millimetre wavelengths.

Wide-field surveys in the CO(3-2) line, with adequate sensitivity, spatial resolution, and area coverage, have emerged only recently (e.g. Takahashi et al. 2008). The HARP 16 element receiver array at the JCMT improved significantly on this situation, for example in the course of the JCMT Gould Belt Legacy Survey (Ward-Thompson et al. 2007; Davis et al. 2010; Graves et al. 2010; Buckle et al. 2010, 2012; Curtis et al. 2010; White et al. 2015), but still these studies remain mostly limited to areas of a few hundred to a few thousand square arcminutes.

It is the latest generation of CO mapping surveys that provide the required combination of sensitivity, spatial resolution, and area coverage to study the structure and kinematics of clouds on scales corresponding to the typical dimensions of filaments and cores (∼0.1 pc) and to reveal the full population and extents of molecular outflows driven by protostars in an unbiased way over entire molecular clouds. The 64-pixel SuperCAM Heterodyne array, developed for use at the HHT/SMT on Mount Graham in Arizona, opened up the opportunity to perform wide field observations in the CO(3-2) line at APEX[1] during a visiting run in late 2014 and early 2015. The 7-pixel LASMA array, now operational at APEX, will ensure efficient wide field molecular line mapping in the future.

We have used SuperCAM at APEX to perform a survey of a 2.7 square degree area in the CO(3-2) line in the Orion GMC complex. The purpose of the present paper is to give an overview of the survey and to present the data. The reduced data will be made publicly available (through the ESO archive) for community use, a first example of which can be found in Bally et al. (2018). These data will allow for examining the environments of young stellar objects in the region (e.g. the HOPS protostars) and the effect of environment (e.g. UV irradiation) on the clouds. We will explore the population of protostellar CO outflows in the survey area in a subsequent publication.

The paper is organized as follows. In Sect. 2 we describe the instrument, the observing strategy, and the survey coverage. In Sect. 3 we describe the data reduction procedure, verify the calibration and basic data reduction procedure by comparing our data with previous APEX FLASH+ CO(3-2) spectroscopic mapping observations of NGC 2023 (Sect. 3.1, Sandell et al. 2015),
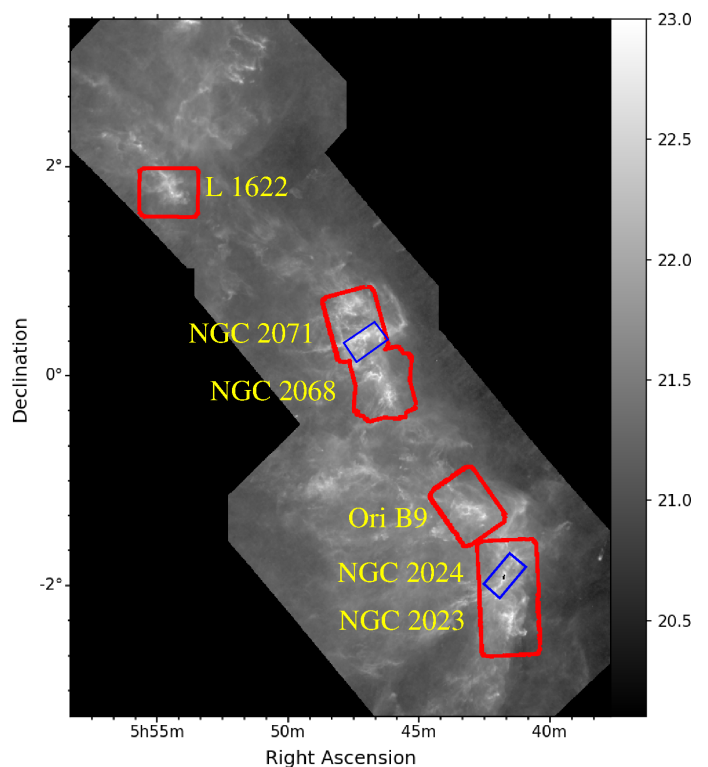
Fig. 1. Column density map (log N_{H} [cm^{-2}]) towards the Orion B GMC (greyscale; based on Herschel dust continuum mapping: Stutz & Kainulainen 2015; Stutz & Gould 2016; Stutz 2018) with the coverage of the ALCOHOLS survey in Orion B overplotted in red. The blue rectangles mark the coverage of the JCMT Legacy Survey of the Gould Belt in the NGC 2024 and NGC 2071 regions (Buckle et al. 2010).

and discuss the noise properties and sensitivity of the survey (Sect. 3.2). In Sect. 4 we present the survey data, discussing each region separately; we discuss spectra integrated over the survey fields, integrated intensity maps, position-velocity cuts, and moment maps (the latter are presented in App. B). We provide a summary and plans for the next steps in Sect. 5. We show noise maps for each survey field in App. A and present moment maps of the CO emission in App. B. Finally, we include 870 μm dust continuum maps[2] taken with Laboca on APEX (App. D), whose main purpose was to obtain sub-millimetre photometry in the course of the HOPS survey (Furlan et al. 2016), but also serve in the present paper to compare the location of dense gas with the CO emission.

2. Observations

We used the SuperCAM heterodyne receiver array (Kloosterman et al. 2012) mounted at the APEX 12 m telescope (Güsten et al. 2006) located on Chajnantor at an elevation of 5100 m to map a total area of ∼2.7 square degrees in the Orion A and Orion B GMCs in the ^{12}CO (3-2) transition at 345.8 GHz. The observations were obtained between December 9 and 25, 2014 (see Table 1), and took a total of 51 hours of telescope time.

SuperCAM consists of a total of 64 heterodyne receivers (individual receivers will be referred to as 'pixels' in the following), of which 49 were operational and connected at the

Table 1. Observing log.

Field	R.A.[a]	Dec.[a]	Size[b]	P.A.[c]	Dates
L 1622	5:54:30.0	1:45:10	27′.5×22′.5	0	2014-12-23
NGC 2071[d]	5:47:25.3	0:29:40	24′.0×32′.5	15	2014-12-14/17/19
NGC 2068[d]	5:46:20.0	-0:04:30	25′.0×32′.5	15	2014-12-11[e]/12
Ori B9	5:43:08.0	-1:14:30	24′.0×32′.5	35	2014-12-22/23
NGC 2024[d]	5:41:34.0	-1:52:00	27′.5×30′.0	3	2014-12-21/22
NGC 2023[d]	5:41:30.0	-2:22:00	27′.5×30′.0	3	2014-12-20/24
L 1641-S (1)[d]	5:40:58.0	-7:54:30	24′.0×32′.5	-5	2014-12-14
L 1641-S (2)[d]	5:42:44.0	-8:16:15	27′.5×35′.0	-5	2014-12-19/20
L 1641-S (3)[d]	5:42:24.0	-8:45:05	40′.0×25′.0	0	2014-12-25
L 1641-S (4)[d]	5:40:58.0	-8:21:20	27′.5×20′.0	0	2014-12-23/24/25

Notes. [a] Coordinates of the adopted fields centre (epoch J2000, as for all coordinates in this paper) [b] Field size in arcminutes [c] Field position angle (in degrees east of north) [d] Fields NGC 2071 and NGC 2068, fields NGC 2023 and NGC 2024, and fields L 1641-S (1)–(4) were combined into larger fields during data reduction. [e] first coverages taken with a position angle of 5°
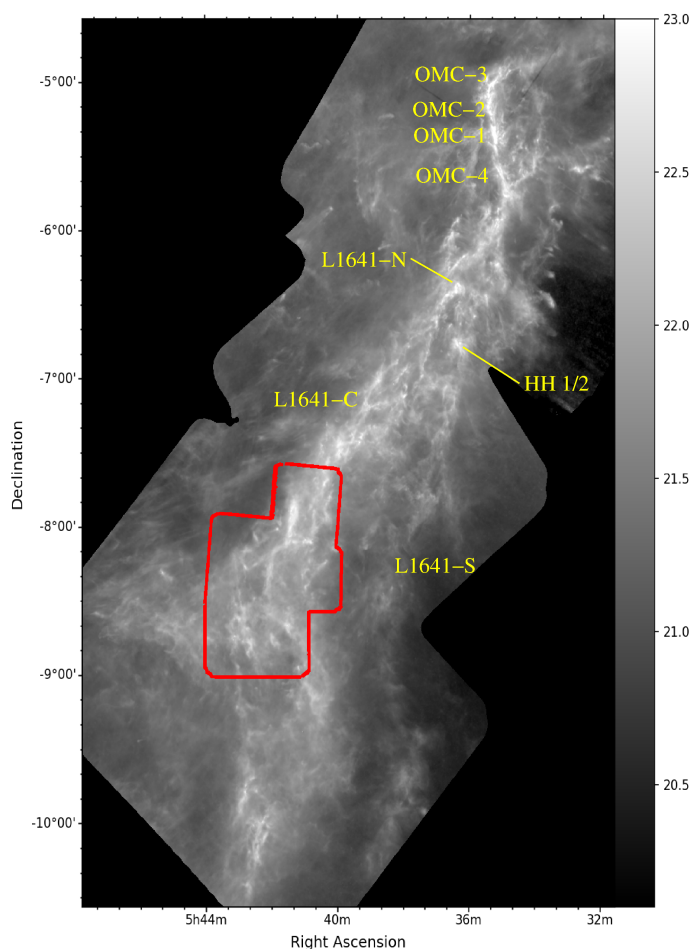
Fig. 2. As Fig. 1 for the Orion A GMC, but with the coverage of the ALCOHOLS survey in Orion A overplotted in red.

time of the observations. The receivers were tuned to the frequency of the ^{12}CO(3-2) transition at 345.7 GHz. The spectra were recorded with a 64×250 MHz Fast Fourier Transform spectrometer, giving 900 channels with a native channel width of ~0.278 MHz/0.24 km/s.

The maps were done in the 'On–The–Fly' (OTF) mode, where a rectangular (or square) area is scanned in a sequence of parallel rows. We chose a spacing between subsequent rows of 150″ (about half the size of the SuperCAM field of view

at APEX), and alternated the scanning direction in a 'zigzag' pattern. Along the rows, spectra were read every 0.5 seconds, spaced by 6″ (~1/3 of the main beam HPBW of 19″), corresponding to a scanning speed of 12″/second. Several coverages were done on each field, with the orientation of the scanning direction alternating between E–W and N–S. Hot/Sky-calibration observations were taken every 3 to 4 rows (depending on the geometry of the map).

Pointing was checked during the observations about once per hour, and the focus was checked at the beginning of each observing session. An observation of a standard Eccosorb (AN-72) blackbody load at the ambient temperature (~285 K) of the APEX C-cabin and a blank-sky observation were taken every few OTF rows to provide hot and sky measurements to compensate for atmospheric extinction by the standard 'chopper wheel' calibration method of Ulich & Haas (1976). These measurements were passed through the APEX online calibrator pipeline (Muders & Hafok 2019) to provide a facility measure of T_{cal} for a central 'fiducial' pixel and subsequently the system noise temperature T_{sys} through per-pixel sky/(hot-sky) 'gain' arrays.

The precipitable water vapour at the APEX telescope ranged from 0.5 mm to 2.2 mm during observations of these Orion maps, corresponding to an zenith atmospheric opacity at 345.6 GHz from 0.1 to 0.35. Receiver noise temperatures across the (44) selected pixels ranged from 75 K to 120 K DSB with a median of 90 K DSB. The heterodyne focal plane array is coupled to the APEX telescope via a compact refractive optical relay comprised of two lenses machined from high density polyethylene (HDPE), which allowed SuperCAM to be mounted into the APEX C-cabin with minimal disturbance to existing instruments. The warm losses of the two relay lenses used to couple the SuperCAM feed horns to the APEX telescope were, however, unfortunately significant: 1.5±0.1 dB. The impact of these losses raised the noise temperature of the combination of receiver plus coupling optics to a range of 200-250 K DSB. The resulting single-sideband T_{sys} varied with atmospheric water vapour content, from 700 K to about 1000 K.

Because T_{cal} was ultimately derived from a single central pixel, a per-pixel scaling factor was required to correct the antenna temperatures of each array pixel. This mean correction factor, derived from OTF maps of Jupiter and Saturn, was a factor of 1.3. This per-beam correction, relative to the T_{cal} that was calculated for the 'fiducial' pixel, results in a uniform T_a^* over the array.

2.1. Coverage

The survey fields were chosen to complement corresponding CO(3-2) observations done at the JCMT (as of the time when the proposals were written, i.e. in March 2014), in the course of the JCMT Goulds Belt survey (Ward-Thompson et al. 2007; Buckle et al. 2010, 2012), and by the HARP instrument team (unpublished). In Orion A (Fig. 2), we cover 1.1 square degrees in L 1641-S (Allen & Davis 2008) south of a declination of −7:30. In Orion B (Fig. 1), 1.6 square degrees were mapped, covering the major star forming clumps around NGC 2023 & NGC 2024 (e.g. Meyer et al. 2008), NGC 2068 & NGC 2071 (Gibb 2008), the Ori B9 region, and the L 1622 cloud (Reipurth et al. 2008).

3. Data reduction

For data reduction we used the GILDAS CLASS software[3] and, for the flatfielding, the ESO MIDAS software. As a first step, bad receiver pixels were identified, and, for each scan, pixels with an average rms higher than two times the median rms of all pixels during the scan were rejected. This typically left ∼44 (of the original 64) good pixels. Linear baselines were then subtracted from all spectra. The fitting range was restricted to 10–20 km/s beyond the maximum velocity extent of the CO emission in each survey field (and excluding the full velocity range where CO emission was detected). The full CO velocity range was identified from spectral cubes created from the raw data, and refined later–on, where necessary.

The spectral cubes initially showed clear striping patterns on regions of bright emission. These patterns were greatly reduced by applying a 'flat–field' correction for the individual receivers. We derived, for each receiver pixel, a rescaling factor, as the flux ratio of the cube using all pixels and a cube including only the respective pixel (using only spectral and spatial regions with emission above a certain brightness threshold). We then compared the total fluxes of the cubes (including all receivers) before and after the flatfielding, rescaling the flatfielded cubes to reproduce the original total flux, where necessary (typically for fields with only fairly faint emission). A separate set of pixel scaling values was derived for each survey field (as the signal–to–noise ratio was generally too low to do it on a per–scan basis). While the cube for any given survey field may generally include scans taken on different days, the scaling factors are seen to be consistent between the fields, implying that they are also stable with time.

The spectra frequently showed 'spikes' (unrealistically high or low values, in individual velocity channels). The spikes show up in individual spectra and frequently in larger groups of consecutive spectra. Often a set of 'typical' velocity channels consistently is affected for several receivers and in several scans. While the off–line calibration removed a significant fraction of the spikes, visual inspection of all spectra was necessary to identify the remaining, obvious groups of spikes, which were then corrected by interpolating between the adjacent, valid velocity channels (CLASS commands DRAW KILL and DRAW FILL). Visual inspection also showed a number of clearly bad spectra, which were removed. In addition, the preliminary spectral cubes showed a number of spectra which clearly were outside the intended map coverage. We identified the corresponding integration time stamps and removed all spectra belonging to these.

We then applied an iterative procedure to remove any remaining spikes (mostly individual spikes in individual spectra)

and to subtract higher order polynomial baselines from the spectra. At this stage, we subtracted from each spectrum a 'model spectrum' of the CO emission. The model spectrum was created using the resulting spectral cubes of the previous iteration, averaging spectra extracted from the cube over a small aperture (of a radius of 8–10 arcsec, smaller than or comparable to the beamsize of the observations) around the position of the respective spectrum. Adjacent and overlapping survey fields were processed together to maximize the quality of the 'model spectra' in the overlap regions (fields NGC 2023 and NGC2024, fields NGC 2068 and NGC 2071, fields L1641S-1 and L1641S-2 and L1641S-3 and L1641S-4). The model spectrum was added back to the spectra after de-spiking/de-baselining.

As spikes, we considered outliers beyond certain multiples of the rms of each (model–subtracted) spectrum, starting at large values (10-15 σ) and reducing to 4.8 σ in the final iterations. At this stage, spikes were replaced by the brightness value of the corresponding velocity channel of the 'model spectrum'.

Similarly, for baseline removal, we increased the baseline polynomial order, starting with linear baselines, up to polynomial orders of 3 in the final iterations. We also decreased the spectral window to be excluded from the baseline fits, from almost the full velocity extent of the emission in the beginning for the linear baselines, to using essentially the full spectrum for baseline fitting in the final iterations.
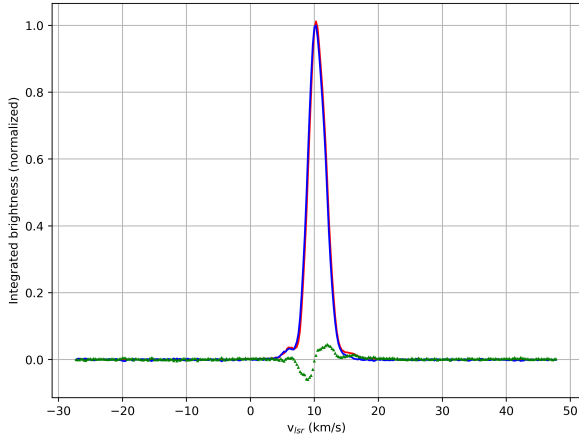
At the end of the automated de-spiking/de-baselining (after typically 4 iterations) the resulting spectra were again checked for pixels and integration ranges requiring even higher order baseline subtraction, resulting from receiver instability or unstable weather conditions. Higher order baselines were fitted and subtracted where necessary, again after subtracting a model spectrum. Here the highest order used was 18, but it has to be noted that very high order baselines only were used on a very minor fraction of the spectra (e.g. order 10 and higher were used for only ∼0.2% of the spectra). A final round of de-baselining with a baseline order of 3 was then done on all spectra (again removing a model spectrum before fitting the baselines).

Finally, we divided the resulting spectra by a mean main beam efficiency of 48% as derived from OTF maps of Jupiter and Saturn, assuming a intrinsic beam-convolved brightness temperature of 150 K for Jupiter (Butler-JPL-Horizons 2012 model, ALMA Memo 594[4]) and 124 K for Saturn given the ring inclination at the time of observation (Weiland et al. 2011). This somewhat low beam efficiency is due to a small but measurable amount of field distortion introduced by the aforementioned refractive relay that couples the SuperCAM focal plane to the APEX telescope. The principal impact is a measurable beam elongation that increases for pixels further from the central optical axis. This elongation reaches a maximum aspect ratio of 1.5:1 for pixels at the corners of the 8x8 square focal plane array. We note that these edge pixels were not used in the analysis.

The error beam of SuperCAM is thus dominated by a very narrow component, only a few arcseconds wider than the 18″ diffraction limited PSF core. The mean coupling efficiency rises to >0.7 in a slightly larger beam convolved to 22″ (corresponding well to main beam efficiencies measured in that frequency range with the APEX facility receivers before the upgrade of the telescope in 2018 (e.g. Güsten et al. 2006)). For further details on the derivation of the SuperCAM beam efficiencies (and their pixel-to-pixel variations) and the error beam see Kloosterman (2014). As will be demonstrated in Section 3.1, high imaging fidelity is achieved with SuperCAM in this configuration at APEX

---

[3] http://www.iram.fr/IRAMFR/GILDAS

[4] http://library.nrao.edu/public/memos/alma/main/memo594.pdf

Fig. 3. Comparison between the integrated (per channel) brightness of the FLASH+ CO(3-2) observations of NGC 2023 by Sandell et al. (2015) (red line) and the ALCOHOLS dataset (blue line). The green triangles show the difference between the two datasets. The data were normalized to give a peak integrated brightness of 1.0 for the ALCO-HOLS dataset.

with a small amount of spatial smoothing. Regardless, a general warning about the interpretation of both spectral line imaging and spectral line profiles at the diffraction limit must be made. It is important to emphasize that the results of this first survey paper do not depend upon data analysis at these very highest spatial frequencies.

We then created cubes at a velocity resolution of 0.25 km/s and with a pixel size of 6 arcseconds, over a velocity range wide enough to include the full CO emission and 10-20 km/s beyond on each side. As some residual baseline instabilities were still apparent in the cubes, we performed another round of baseline subtraction on the cube, where the spectral range to exclude from the fit was set to the full spectral extent of the CO emission; special care was given to areas with very high velocity emission, making sure that the exclusion range was set large enough (and the baseline order low enough) to avoid subtracting out or artificially introducing any high velocity line wing emission.

3.1. Comparison with previous APEX CO(3-2) map of NGC 2023

A subset of our survey region in NGC 2023 was previously mapped in the CO(3-2) line with the FLASH+ receiver (Klein et al. 2014) on APEX, that is, with the same telescope and on the same site (Sandell et al. 2015). We use this dataset to check the performance of SuperCAM and to verify the calibration and the robustness of the data reduction against artificially introducing or subtracting out high velocity line wing emission.

To do so, we created a subcube of the ALCOHOLS data at the same spatial and spectral gridding as the FLASH+ data cube (which also used a pixel size of 6″ and a velocity channel width of 0.25 kms/s). After correcting for a small pointing offset between the two datasets (3″ in declination), we used two approaches to compare the flux scaling. First, we summed up the brightness temperature values of all pixels within a velocity channel, and compared the resulting integrated spectra (Fig. 3). We find an excellent agreement of the peak values (as derived from Gaussian fits) of the two spectra, which differ only by 0.7% (where the FLASH+ map is slightly brighter). We note a small
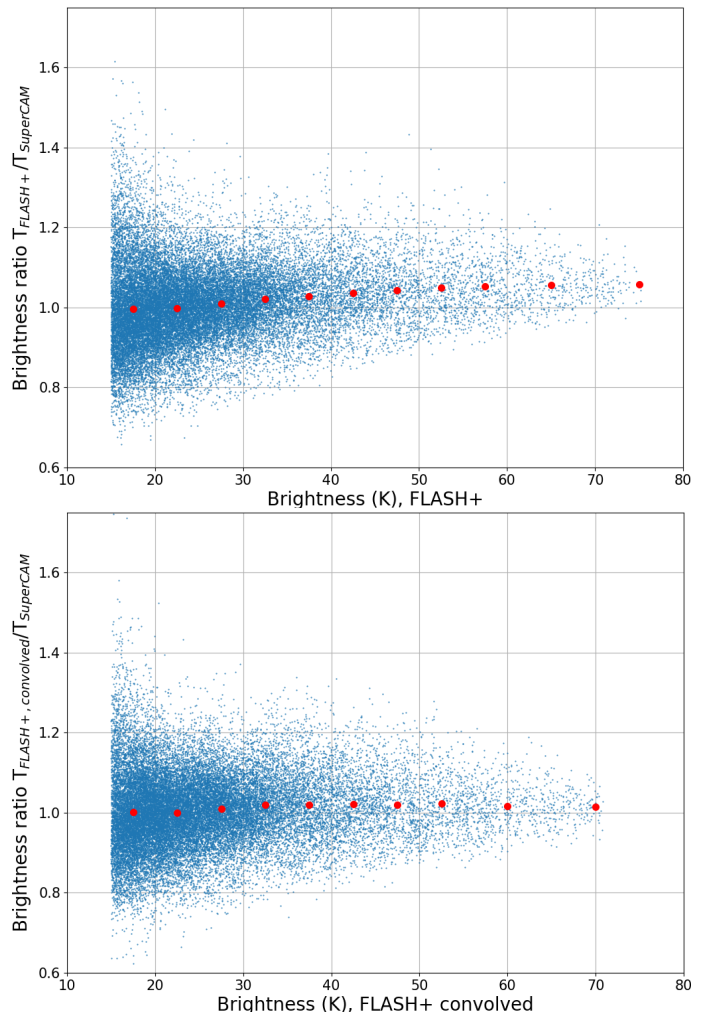
Fig. 4. Per pixel flux ratios (blue dots) of the Sandell et al. (2015) FLASH+ CO(3-2) NGC 2023 data to the ALCOHOLS SuperCAM data, as a function of the brightness of the FLASH+ data, for pixels with a FLASH+ brightness greater than 15 K. Red bullets represent flux ratios averaged over 5 K temperature bins (10 K bins for the two rightmost points). Top: direct ratio of the FLASH+ and SuperCAM data; bottom: ratio after convolving the FLASH+ data with a 9″ Gaussian.

velocity shift between the two datasets (~0.11 km/s) producing the negative and positive residual immediately to the blue and red side, respectively, of the line in the difference spectrum (green symbols in Fig. 3. The magnitude of this shift is very close to half the channelwidth and might be due to a different definition of the channel velocity between the two datasets. The ALCOHOLS data also reproduce the shape of the blue-shifted line wing emission very well. In the redshifted wing, at velocities between $\sim$ 14 km/s to $\sim$ 18 km/s the FLASH+ data show a mild excess (of the order of 1-1.5% ($\sim$0.3 K) of the flux at the line centre. The excess cannot be attributed to compact features as may be expected from outflows, but is apparently due to a diffuse, very low surface brightness component, which might not be real but due to, for example, slight differences in the spectral baseline fitting and subtraction procedure.

For each pixel of all channel maps that were brighter than a threshold of 15 K, we also derived the brightness ratio between the two datasets. The cutoff at 15 K was chosen as a compromise between having a significant number of flux values at good signal-to-noise in both datasets, as the value around which the flux ratios started to show increasingly significant scatter

greater than ~20%. Again, we find an overall excellent agreement, with a mean and median flux ratio of 1.011 and 1.008, respectively, with the FLASH+ map being slightly brighter. We have also plotted the pixel-to-pixel brightness ratios as a function of brightness (in the FLASH+ map, Fig. 4, top panel). Here, we notice a trend of increasing flux ratio with brightness by about 5% when going from 15 K to the maximum of ~75 K. We attribute this trend to a small difference between the main core of the point spread functions (psf) of the two observations. The brightest emission is in very compact knots, where the peak flux will be much more affected by blurring by a broader psf than more extended structures. To test this assumption, we convolved the FLASH+ data cube by Gaussians with FWHMs of 6″ and 9″and found that for a convolution with a 9″ Gaussian the flux ratios as a function of (convolved) FLASH+ brightness become essentially flat (Fig. 4, bottom panel). Convolving a 18″ or 19″ Gaussian beam with a 9″ Gaussian would result in a 20″.1 and 21″ FWHM beam, respectively, that is, would correspond to an only marginally broader psf. There remains some residual structure in the flux ratio vs. brightness plot, which might point to a more complicated, possibly non-axisymmetric difference between the psfs of the FLASH+ and SuperCAM observations, due to the substantial differences in the optics of the two systems.

3.2. Sensitivity and noise properties

The scanning pattern used during the observations was not designed to provide fully sampled maps for each individual receiver pixel (which would naturally result in near uniform coverage overall), but assumed that the differences in the sensitivity between receivers and lower effective coverage due to dead or poor pixels would average out, as still any position in the map was observed in a single scan by several pixels, and several coverages were taken for each field, with the array orientation changing from scan to scan due to the rotation of the target area on the sky. To check the validity of this approach we derived noise maps for each field by calculating the rms of the spectra at any spatial pixel in the cube (over the velocity range beyond the maximum velocity extent of CO emission in the respective cube).

We show histograms of the rms distribution for each survey field in Fig. 5, while maps of the rms are shown in Appendix A (which also shows full frequency distributions of the brightness values for all fields, including the full spectral range, in Fig. A.6). The histograms are characterized by a narrow peak centred around 0.7–0.8 K and a tail extending to higher rms values. As can be seen from the rms maps, the high–rms tails stem from the edges of the maps, where coverage is lower. The histogram for L1641-S shows a shoulder next to the main peak, which is due to the southernmost sub–field having lesser coverage and correspondingly higher rms (see Fig. A.5). While the maps show a clearly distinguishable striping pattern, indicating some degree of non–uniform rms and pixel–to–pixel variations, the rms values within the central parts of the survey fields are fairly uniform, as indicated by the narrow main peaks of the histograms. To quantify further the typical rms in the central parts of the survey fields we fitted the peak of the rms histograms with a Gaussian curve. The resulting mean values and standard deviations are indicated in the plots and listed in Table 2, indicating typical rms values of 0.7–0.8 K and pixel–to–pixel variations of the order of 10–20%. We take the mean of the Gaussian fits as the final sensitivity of the survey (at a pixel size of 6″ and a velocity resolution of 0.25 km/s). This level is comparable to the target sensitivity of the JCMT Gould Belt Legacy survey of 0.3 K per

pixel at a velocity resolution of 1 km/s (Ward-Thompson et al. 2007), but significantly poorer than achieved in the JCMT HARP maps in Orion B (0.1 K per pixel at 1 km/s Buckle et al. 2010).

4. Results

In this section, we provide a general description of the properties of the ^{12}CO(3–2) emission in the survey area. The main scientific goal of the survey, a characterization of the population of protostellar molecular outflows, is deferred to a companion paper. We here present the legacy data for community use. To illustrate the potential use, we show examples of outflow maps, to be compared with previous results.

In the following subsections, we discuss integrated intensity maps, position velocity cuts, and moment maps for each survey field separately, and a few remarkable sub-regions. In order to obtain a first impression on the properties of the CO emission, we show for each survey field spectra integrated over the entire area in Fig. 6, and Table 3 gives the line parameters as derived from Gaussian fits to those integrated spectra. For L 1622 (cf. Kun et al. 2008) we notice the presence of two well separated velocity components, which we refer to as the 1 km/s component and the 10 km/s component. In Ori B9 we also see two distinct spectral components, which we refer to as the 3 km/s and 10 km/s components. The NGC 2068/NGC 2071 and NGC 2023/NGC 2024 fields are dominated by a single, broad component, with a faint secondary component seen at lower (blue-shifted) velocities in the NGC 2023/NGC 2024 fields. The L 1641-S spectrum shows two closely spaced, narrow components, which we refer to as the 3 km/s component and the 6 km/s component.

4.1. L 1622

L 1622 has been described as a cometary cloud (e.g. Reipurth et al. 2008). Its overall shape is suggestive of being subject to radiation or wind from the south-west. We see two well separated velocity components in its integrated spectrum in Fig. 6. Consistent with previous observations, we see a clear cometary shaped cloud at velocities around ~1 km/s (Fig. 7, top), which corresponds to the actual L 1622 cloud. The emission around 10 km/s is much more diffuse (Fig. 7, bottom), and may trace the outskirts of the L 1617 complex of cometary clouds, located about 1 degree to the north-west (e.g. Reipurth et al. 2008). The velocity maps in Fig. B.1 indicate an overall rather smooth velocity field, with indications for a velocity gradient along the clouds minor axis. Together with the relatively small line width (less than 1.5 km/s over the bulk of the cloud, larger line widths can mostly be associated with outflows), the agent responsible for the cometary appearance is likely not an effective trigger of turbulence within the cloud.

Figure 9 shows position-velocity cuts through the cloud; the top panel shows a cut along the cloud's major axis. It confirms the overall fairly quiet nature of L 1622, as the emission is seen with very little variation in velocity from head to tail, except for offsets between 400″ and 850″. Between ~450 and 850″, the cut intersects two molecular outflows, driven by HOPS 1 and HOPS 354 (the latter outflow is seen at optical and infrared wavelengths as HH 962, Bally et al. 2009). At an offset around 400″, there is faint emission extending over 1-2 km/s beyond the ambient clouds velocity, which we attribute to a faint outflow originating from the HBC 515 multiple pre-main sequence system (Reipurth et al. 2010). We note an emission gap, with only
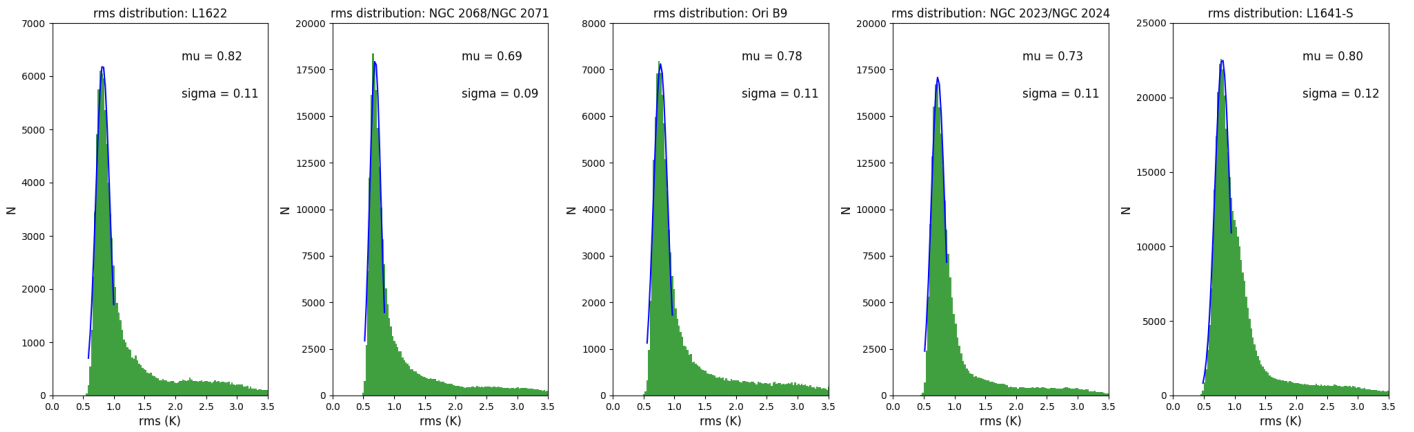
Fig. 5. Distribution of rms values measured for each spatial pixel (excluding the spectral range showing CO emission) for each survey field (histograms, restricted to rms<3.5). The blue curves indicate Gaussian fits to the peak of the histograms (with the resulting mean (μ) and standard deviation (σ) indicated).

Table 2. Noise properties (rms in K), by survey field.

Field	N_{pix}[a]	μ, σ[b]	rms min, max[c]	median[d]	mean[d]	stddev[d]
L1622	96355	0.82, 0.11	0.518, 6.831	0.91	1.21	0.69
N2068/N2071	239639	0.69, 0.09	0.456, 8.484	0.78	1.10	0.74
Ori B9	112406	0.78, 0.11	0.490, 5.134	0.87	1.19	0.74
N2023/N2024	221477	0.73, 0.11	0.442, 6.381	0.80	1.03	0.63
L1641-S	413827	0.80, 0.12	0.416, 9.889	0.91	1.14	0.69

Notes. [a] N_{pix}: total number of valid spatial pixels in the field. [b] μ, σ: mean value and standard deviation from Gaussian fit to the peak of the rms histogram, respectively. [c] rms min, max: minimum and maximum rms, respectively. [d] median, mean, stddev: median, mean and standard deviation including all rms values, respectively.
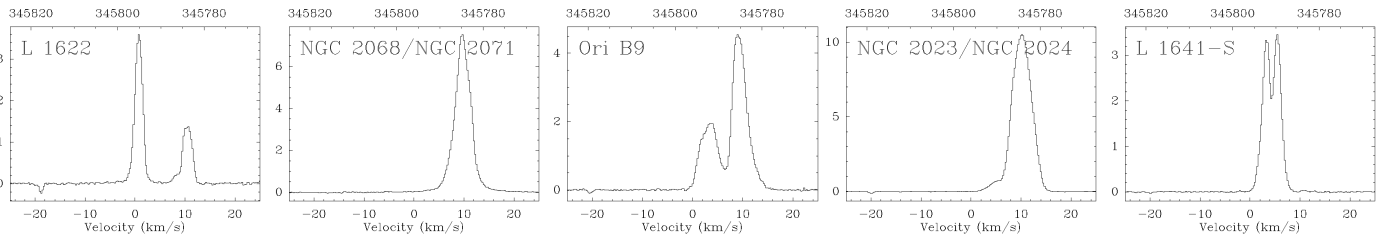
Fig. 6. CO spectra averaged over the full survey fields. L 1622 and Ori B9 each show two distinct velocity components, L1641-S also features a double peaked spectrum, while the NGC 2023, NGC 2024, NGC 2068, and NGC 2068 areas show single peaked spectra, though a hint of a secondary component is seen as a blue shoulder in the NGC 2023/NGC 2024 spectra.

Table 3. Velocities and line widths of the main CO components identified from Fig. 6 derived from Gaussian fits

| Field	v (km/s)	FWHM (km/s)
L1622 (1 km/s)	0.8	1.8
L1622 (10 km/s)	10.5	2.1
N2068/N2071	9.8	3.7
Ori B9 (3 km/s)	3.2	3.8
Ori B9 (10 km/s)	9.4	3.3
N2023/N2024	10.2	4.5
L1641-S (3 km/s)	3.2	1.9
L1641-S (6 km/s)	5.6	1.8

faint emission, between the position of HBC 515 and the onset of the bright, redshifted emission from the HOPS 1 outflow.

Figure 9 also shows four position-velocity cuts through L 1622 along the cloud's minor axis in its middle and bottom rows. The cuts in the middle row are in the head of the cloud, while the cuts in the bottom row are taken further west, in the tail. The cuts through the head indeed seem to show an overall velocity gradient, going from more blue-shifted velocities in the south-east to more red-shifted in the north-west. The cut in the middle-left panel intersects the position of HBC 515 (marked with the dashed line) and again shows faint emission extending beyond the ambient cloud velocity. The cut in the middle-right panel intersects the emission gap seen in the cut along the cloud's major axis, and shows up as small gap in this direction as well. Together, this gap suggests the presence of a small cavity to the north-east of HBC 515, possibly created by outflow from this system and corresponding to the cavity seen extending to the south-west of HBC 515 in optical images (e.g. Reipurth et al. 2008; Bally et al. 2009).

The cut in the bottom-left panel of Fig. 9 intersects a bright CO emission feature, which stands out in all three moment maps as bright (moment 0), blueshifted (moment 1) and broad (moment 2), and shows up as high-velocity emission in the position-velocity cut. It is located near the position of the bright, optical shock system of HH 122 (Reipurth & Madsen 1989; Bally et al.
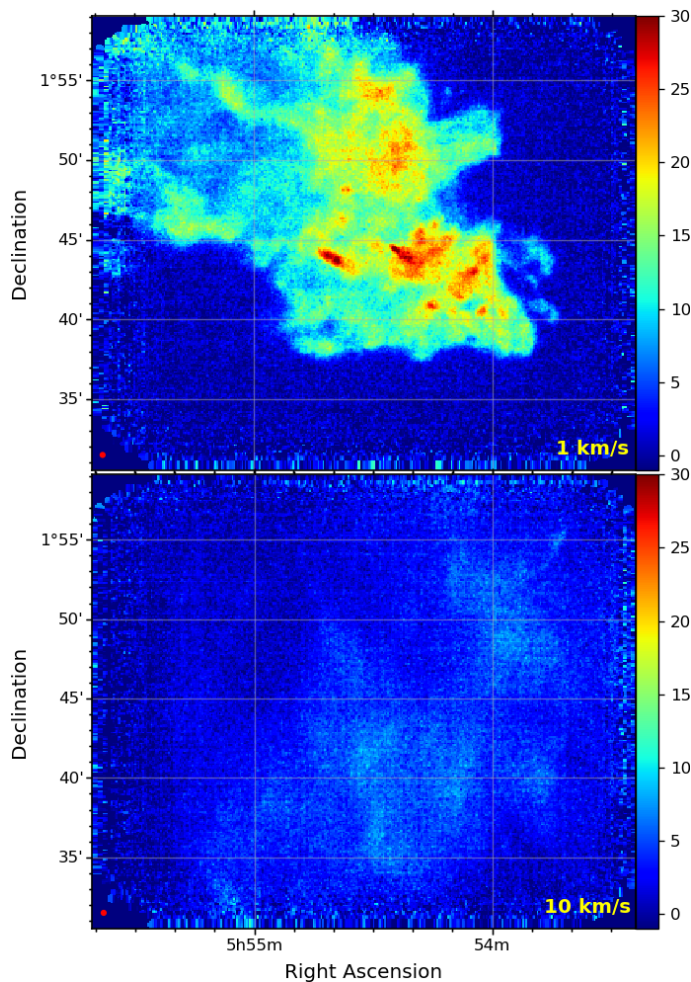
Fig. 7. CO emission in the L 1622 field, integrated from -1 km/s to 2.25 km/s (top, in K km/s) and from 9.25 km/s to 12 km/s (bottom). The red dots in the bottom left corners indicate the beam size.
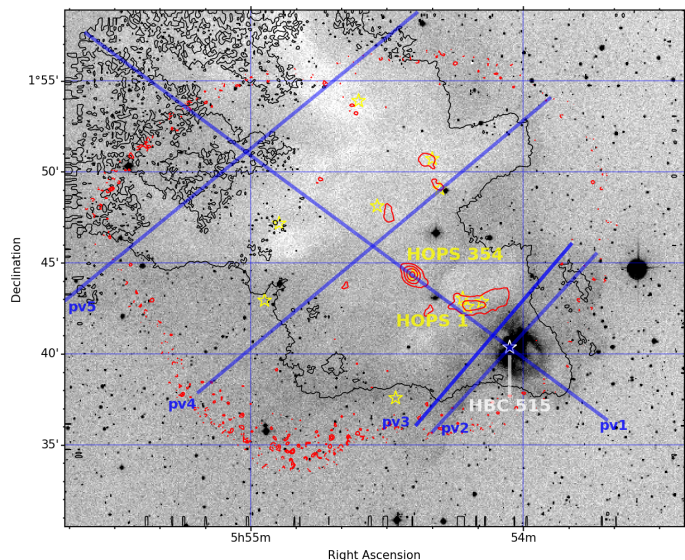
Fig. 8. Overview of the L 1622 field. The greyscale shows an optical (DSS2 blue) image. Black and red contour overlays mark the extent of the CO(3-2) emission of the 1 km/s component and APEX/Laboca 350 μm dust continuum emission, respectively. Yellow stars mark the location of HOPS protostars, while the white star marks the position of the HBC 515 pre-main-sequence multiple system. Blue lines mark the location of the position-velocity cuts shown in Fig. 9.
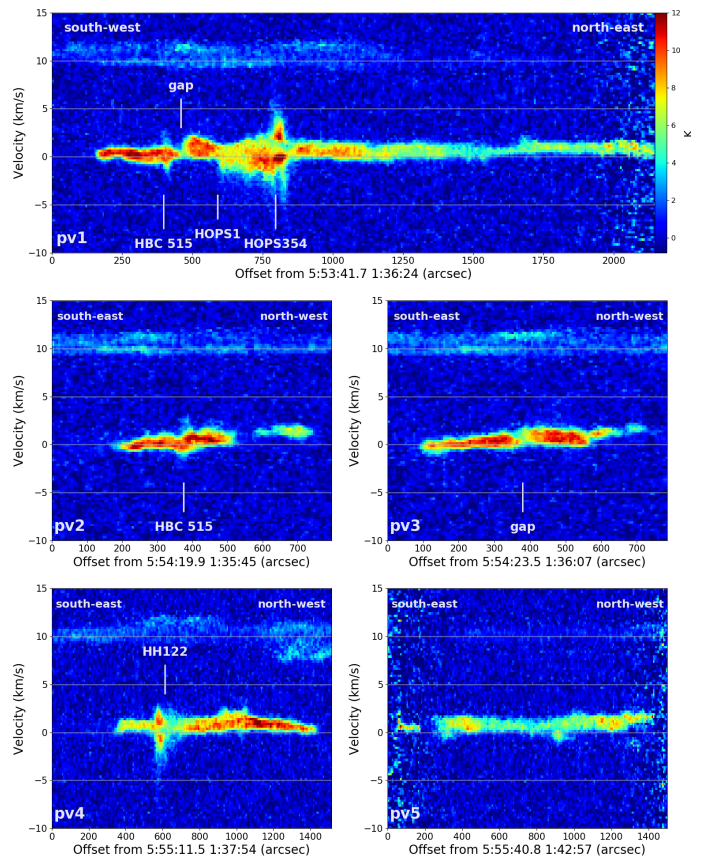
Fig. 9. Position-velocity cuts across L 1622, as marked in Fig. 8. Top: cut along the clouds major axis, starting from $5^h53^m41\!\!.\!\!^s7$, $1°36'24''$ to the south-west of the cloud, ending at $5^h55^m36\!\!.\!\!^s3$, $1°57'37''$ in the north-eastern corner of the mapped area. Middle row: cuts along the minor axis of the cloud; left panel (pv2): starting at $5^h54^m19\!\!.\!\!^s9$, $1°35'45''$ (south-west), ending at $5^h53^m44^s$, $1°45'29''$ (north-east); right panel (pv3): starting at $5^h54^m23\!\!.\!\!^s5$, $1°36'07''$ (south-west), ending at $5^h54^m23\!\!.\!\!^s5$, $1°36'07''$ (north-east). Bottom row, cuts along the minor axis of the cloud, further east in the tail of the cloud; left panel (pv4): starting at $5^h55^m11\!\!.\!\!^s5$, $1°37'54''$ (south-west), ending at $5^h53^m54\!\!.\!\!^s2$, $1°54'02''$ (north-east); right panel (pv5): starting at $5^h53^m54\!\!.\!\!^s2$ $1°54'02''$ (south-west), ending at $5^h53^m54\!\!.\!\!^s2$ $1°54'02''$ (north-east).

2009) and might indicate the terminating shock of the molecular outflow driven by HOPS 1. In contrast to the cuts through the head of the cloud, the cuts through the tail do not show a pronounced, systematic velocity gradient, possibly indicating that the agent creating the gradient is more efficient at the head of the cloud (e.g. uneven exposure to wind or radiation, between the south-eastern and north-western extents of the cloud).

4.2. The NGC 2068/NGC 2071 area

Figure 10 shows the CO emission in the NGC 2068/NGC 2071 fields integrated over the velocity interval from 7.5 km/s to 13 km/s, and Fig. 11 shows an overview of the region, comparing optical, CO, and dust emission. The brightest CO emission broadly corresponds to the NGC 2068 nebula, with the very brightest region being seen at the interface between the optical nebulosity and the dense filament seen in dust emission in the southern part of NGC 2068 (e.g. Motte et al. 2001; Kirk et al. 2016, see Fig. 11). Further bright emission is seen towards the NGC 2071-IR region (while the area of the brightest optical
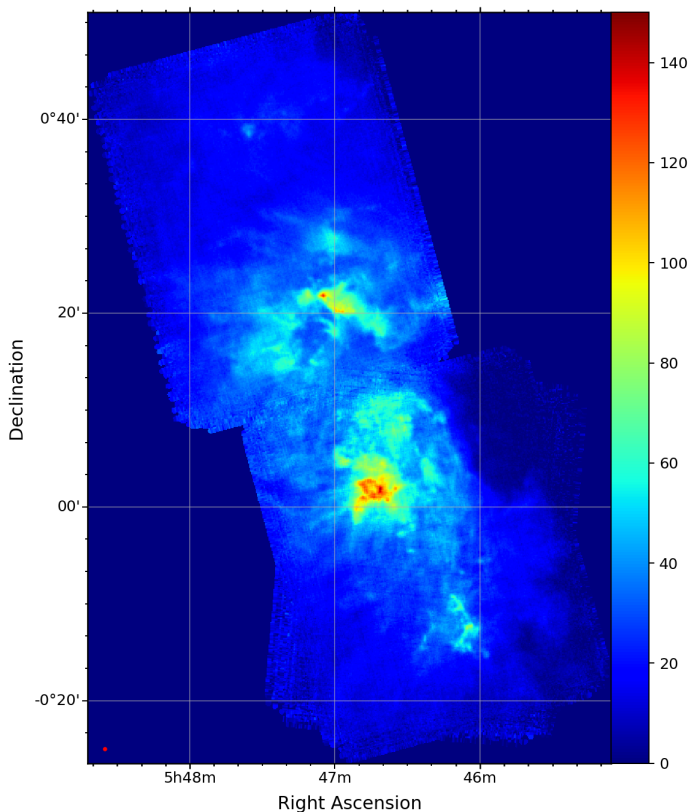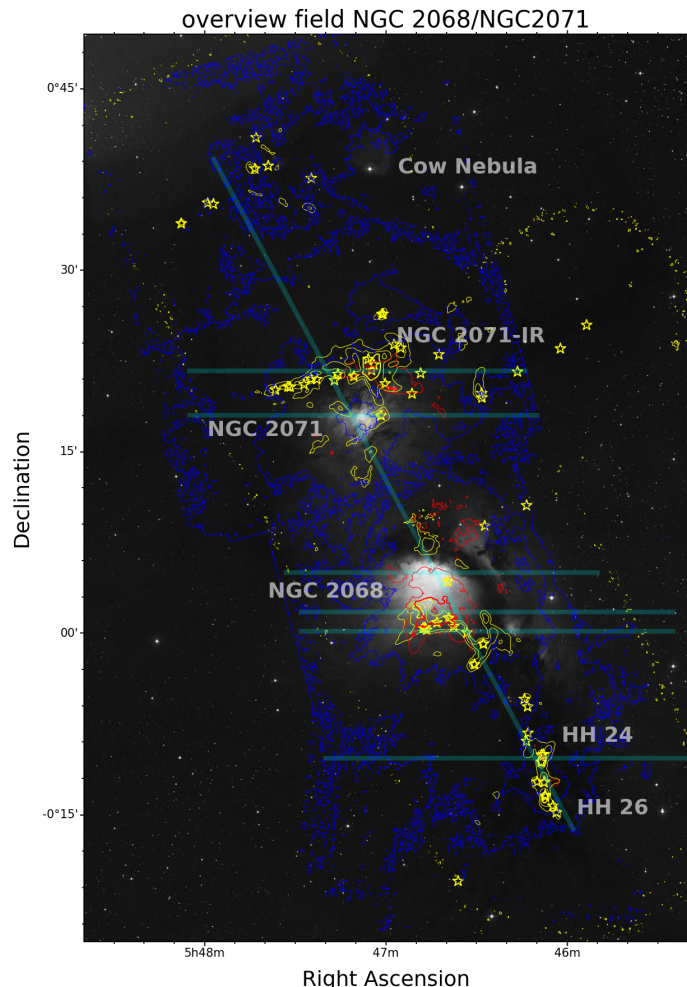
Fig. 10. CO emission in the NGC 2068 and NGC 2071 field, integrated from 7.5 km/s to 13 km/s (in K km/s). The red dot in the bottom left corner indicates the beam size.

Fig. 11. Overview of the NGC 2068/NGC 2071 region, showing a DSS2-blue optical image of the region, with the integrated CO emission from Fig. 10 overplotted as blue and red (for the brightest regions) contours, and APEX Laboca 870 μm dust continuum as yellow contours. Yellow stars mark the position of HOPS protostars, and cyan lines mark the location of the position-velocity cuts shown in Fig. 12.

emission in NGC 2071 corresponds to a local minimum in CO emission) and in the HH 24-HH 26 region.

In all three moment maps (Fig. B.2) the NGC 2071-IR outflow (see Sect. 4.2.1 below) is the most outstanding feature, but a few additional outflows in the HH 26 and NGC 2068 region are also readily visible. There is an overall north-south velocity gradient, with the northernmost parts of the area being more blueshifted. The area around the NGC 2071 nebula stands out as having consistently large (> 3 km/s) line widths, but also the HH 26 and NGC 2068 region features line widths greater than 2 km/s over wide areas.

Figure 12 shows position-velocity cuts through the NGC 2068/NGC2071 area. The top panel shows a cut going largely from south to north, while the remaining panels show east-west cuts (at fixed declination). The south-to-north cut shows the overall velocity gradient already noted in the moment 1 map. At offsets around 400″ and 1000″ the cut intersects the HH 24 to HH 26 region and the dense ridge of cores in the southern part of NGC 2068, respectively, which both display strong molecular outflow activity. The brightest CO emission is seen in NGC 2068 as a single velocity component. Starting at an offset of ~2200″ the CO emission splits into two components, roughly coinciding with the appearance of the NGC 2071 optical nebulosity. At around 2500″, the cut intersects a dust ridge extending east from the NGC 2071-IR core that is associated with several protostars, where again high-velocity CO due to protostellar outflow activity is present. Further north, at offsets greater than 3000″, only one velocity component is seen.

The east-west cuts in Fig. 12 are ordered from north to south. The panels in the second row show cuts going through NGC 2071-IR (left panel) and the brightest part (at optical wave-

lengths) of the NGC 2071 nebula. Both cuts show CO to be split into two components over a large fraction of the cut. The cut going through the brightest part of the optical nebula in particular shows a dominant, single component at both ends, splitting up when going further towards the middle of the cut. The northernmost cut through NGC 2071-IR shows very bright emission extending to high velocities due to the NGC 2071-IR molecular outflow (Sect. 4.2.1). The cuts in the third row and fourth row, left, go through the NGC 2068 optical nebulosity. The northernmost (third row, left) intersects the brightest optical emission, the second (third row, right) goes through the brightest CO emission (just north of the bright dust continuum ridge), while the third cuts through the bright dust ridge. In all three cuts the brightest emission is seen as a single component, while the fainter emission (particularly to the west) tends to show double-peaked lines, typically at offsets that correspond to the location of the dark (in the optical) ridge marking the northern and western boundary of the NGC 2068 nebula and the fainter optical emission nebulosities further west. While we can't exclude CO self-absorption as the cause of the double-peaked line profiles seen in several areas in NGC 2071 and NGC 2068, its association with optical nebulosities suggests that the double-peaked lines are due to ex-
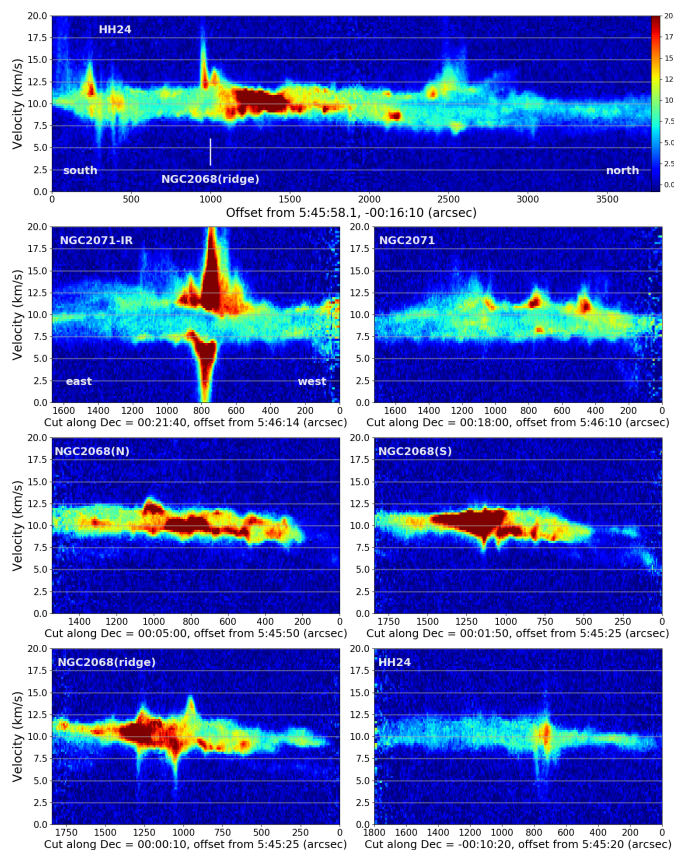
Fig. 12. Position velocity cuts across the NGC 2068/NGC 2071 survey field. Top: cut starting from 5:45:58.1, -0:16:10 (south-west), ending at $5^h47^m57\overset{s}{.}0$, $+00°39'10''$ (north-east).

panding bubbles in the molecular gas, driven by the early-type stars illuminating the NGC 2068 and NGC 2071 nebulae.

Finally, the southernmost cut (Fig. 12, bottom row, right panel) intersects the HH 24 region, known to be an active site of an outflow, and indeed shows clear high velocity emission in the middle of the cut. Perhaps more remarkable is the sharp transition from a narrow line profile to the west to a broad profile to the east of the HH 24/HH 26 dust ridge. Indeed, examining the moment 2 map (line width) more closely, the entire HH 24-HH 26 ridge is located in a transition zone between linewidths hardly exceeding 1 km/s to its south and west, and linewidths mostly greater than 2 km/s to its north and east. We speculate that this transition in velocity dispersion might be related to the peculiar overabundance of particularly young protostars (PBRs) in this area (Stutz et al. 2013).

4.2.1. The NGC 2071-IR outflow

The outflow driven by the intermediate-mass protostar NGC 2071-IR (Walther & Geballe 2019) was among the first to be detected in high-velocity CO emission (Bally 1981; Lichten 1982; Snell et al. 1984). Subsequent, deeper observations showed that the outflow extends to much higher velocities than originally seen (Margulis & Snell 1989; Choi et al. 1993), with a full velocity extent of over 100 km/s (−50 to +65). Chernin & Masson (1992) show that the extremely high velocity (EHV) component of the flow, particularly in the red lobe, clearly stands out as a separate bump in the spectrum and is in the form of compact blobs of emission. Chernin & Welch (1995)

interpreted the red EHV feature as originating from a jet interacting with a dense clump in its way.

Our ALCOHOLS survey data for this outflow are presented in Fig. 13. We show red- and blue-shifted CO emission at low outflow velocities, together with emission at rest velocities around 10 km/s, in the leftmost panel, reproducing the overall shape and extent of the outflow as seen before (Snell et al. 1984; Moriarty-Schieven et al. 1989; Chernin & Masson 1992), revealing additional outflowing CO gas at fainter intensity levels (see also Buckle et al. 2010). At higher velocities we recover the well collimated outflow shape seen also in Moriarty-Schieven et al. (1989) and Chernin & Masson (1992). Finally, at extreme velocities (Fig. 13, rightmost two panels) we see the emission only from small, compact regions relatively close to the protostar, with particularly the red EHV component also clearly standing out in the spectrum. Consistent with earlier observations (Chernin & Masson 1992), the red component is more compact, while the blue component extends over a larger range along the outflow axis. The velocity extent we see in our data, from about −50 kms in the blue lobe, to about +65 km/s in the red lobe, also agrees well with previous, targeted observations. Overall, this agreement confirms the quality of our data reduction procedure, particularly with respect to spectral baseline removal.

4.2.2. The Cow Nebula globule

Figure 14 shows the CO(3-2) emission of a remarkable cloud in the northern part of the NGC 2071 survey field (see Fig. 11) with an almost perfectly circular appearance. Its morphology is highly suggestive of a spherical cloud, and might serve well as an observational testbed for numerical and theoretical considerations. Due to its simplicity, we refer to it as the "Cow Nebula" globule.

The globule is well separated in velocity from the Orion B cloud, being centred at $v = -5.25$ km/s (while the bulk of the cloud in this area is centred at around +8 km/s. The top-left panel in Fig. 14 shows the CO(3-2) emission towards the Cow Nebula globule, integrated over its full velocity extent ($v = -6.25$ km/s to −4.5 km/s). The circle serves to illustrate the circular shape of the globule. It is centred at $5^h47^m04\overset{s}{.}3$, $+00°39'20''$, which we take as the position of the globule, and has a radius of 85″. Assuming that the globule is at the same distance as the Orion B clouds ($\sim$ 400 pc), this extent corresponds to a radius of 34 000 AU or 0.16 pc.

The top-right panel shows the CO integrated emission overlaid as contours on a DSS2-blue optical image. A small, cometary feature is clearly associated with the CO emission. At optical wavelengths, the 'head' of the feature points towards the south-west (towards the Orion Belt stars), and its rim aligns perfectly with the CO emission. Apart from being mentioned in the compilations of (reflection) nebulae by Dorschner & Gürtler (1963) (DG 82) and Bernes (1977) ([B77] 100) (see also Magakian 2003) this object has apparently not yet been studied in any detail. A diffuse tail extends towards the north-east, and is seen to extend further in the optical images than in CO. The star seen in projection against the clouds southern edge (HD 290857) seems to be an unrelated foreground object.

The panel to the bottom-left shows the CO map overlaid on a Spitzer IRAC 8 μm map (Megeath et al. 2012). Here, a sharp bright rim is seen outlining the western edge of the CO globule. Finally, the panel to the bottom-right shows the CO map overlaid on a JCMT 850 μm (dust continuum) map (Kirk et al. 2016). We see a faint, diffuse ridge of emission at the western edge of the globule, coinciding broadly with the area of the bright-
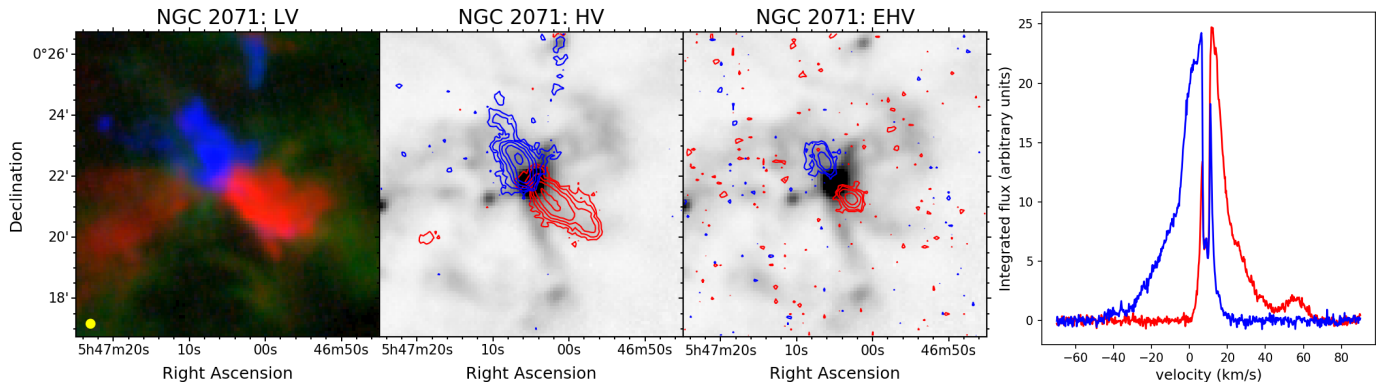
Fig. 13. Maps and spectra of the NGC 2071 molecular outflow. The leftmost panel shows the low velocity component of the outflow (red: $v = +13$ to $+20$ km/s, blue: $v = -5$ to $+5$ km/s) along with CO emission around the clouds rest velocity (green: $v = +6$ to $+12$ km/s). The yellow dot indicates the beam size. The two central panels show contour plots of the high-velocity (HV) emission (red: $v = +21$ to $+44$ km/s, blue: $v = -25$ to -6 km/s) and extremely high-velocity (EHV) emission (red: $v = +45$ to $+67$ km/s, blue: $v = -41$ to -26 km/s); the greyscale shows APEX Laboca 870 μm dust continuum emission. The panel to the right shows spectra extracted over a 12″ radius on the peak position of the EHV emission component, showing a well separated EHV feature particularly in the red lobe.
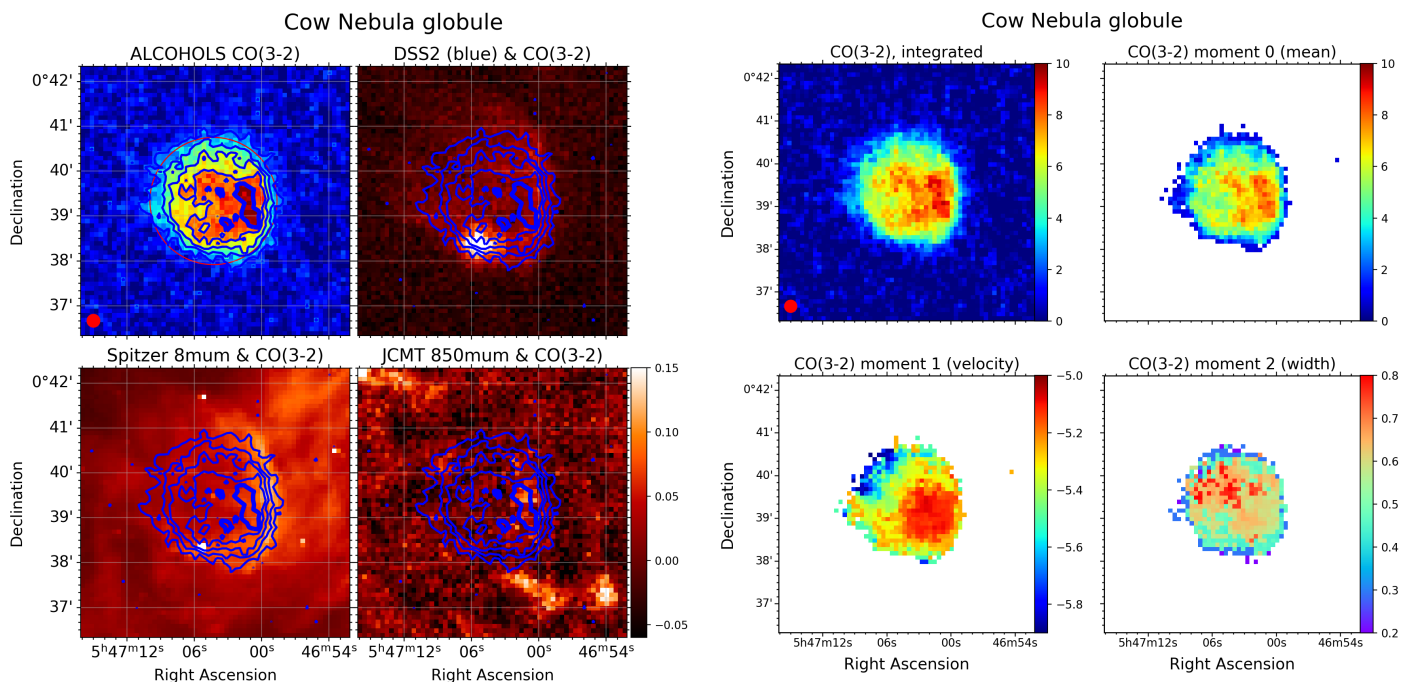
Fig. 14. CO emission from the Cow Nebula globule. Top left: emission integrated over the velocity interval $v = -6.25$ km/s to -4.5 km/s. The circle is centred at $5^h47^m04\overset{s}{.}3$, $+00°39'20''$ and serves to illustrate the circular morphology of the globule. Top right, bottom left, bottom right: integrated CO (top left panel) overlaid as contours over an optical image of the region (DSS2, blue), a Spitzer 8 μm image (Megeath et al. 2012), and a JCMT 850 μm map (Kirk et al. 2016), respectively.

Fig. 15. CO moment maps for the Cow Nebula globule. Top left: emission integrated over the velocity interval $v = -6.25$ km/s to -4.5 km/s. The red dot indicates the beam size. Top right, bottom left, bottom right: moment 0, moment 1 (velocity), and moment 2 (line-width), respectively.

est CO emission. We do not see any compact continuum source that could indicate the presence of an embedded protostar in the globule or even a dense, pre-stellar core. We also do not see any HOPS protostars within or close to the boundary of the CO emission.

In Fig. 15 we show moment maps for the Cow Nebula globule. The radial velocity is fairly constant, around -5.2 km/s, over the south-western part of the cloud, that is, the head. In the tail towards the north-east, we observe a shift to more blue-shifted velocities. We only see a marginal trend in the line widths, which are of the order of 0.6–0.65 km/s in the south-western half of

the globule, and slightly broader (0.7–0.75 km/s) in the northeastern half of the globule.

Taken together the data suggest that the Cow Nebula Globule, despite showing a cometary structure in the optical, is intrinsically a round (possibly spherical, in 3D) starless cloud. We interpret the steeper rise in CO emission and the enhanced brightness seen around the western edge of the globule as being due to heating from the west (as indicated by the bright rim seen in the Spitzer image outlining the western globule edge) rather than being due to larger column density in the western half of the globule. Clearly, subsequent multiline observations are needed to determine better the column density structure of the globule, and higher spectral resolution will be required to determine its dynamical state.
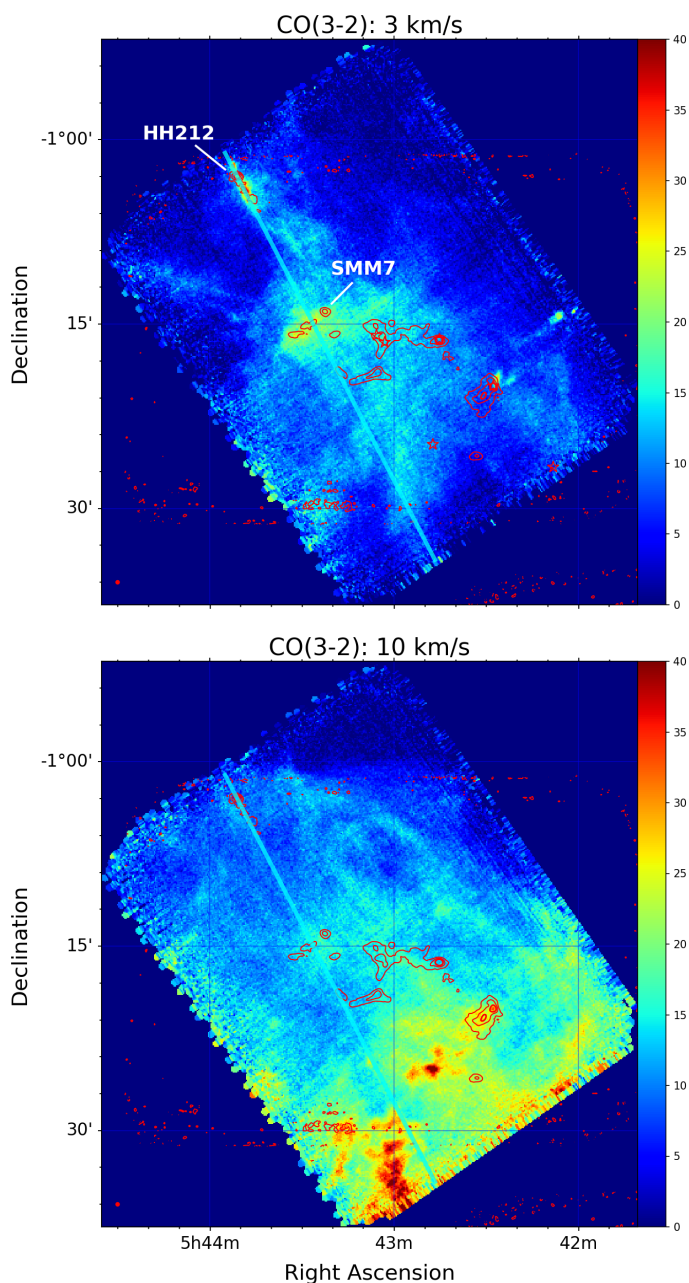
Fig. 16. CO emission in the Ori B9 field, integrated from 0.5 km/s to 5.5 km/s (top, in K km/s) and from 8 km/s to 12 km/s (bottom). Contours mark APEX/Laboca 870 μm dust continuum. The blue line marks the location of the position-velocity cut shown in Fig. 17. The red dots in the bottom left corners indicate the beam size (which is the same for the ALCOHOLS and Laboca data).

4.3. Ori B9

The Ori B9 region shows two distinct velocity components, centred at around 3 km/s and 10 km/s. We show integrated intensity maps for both components in Fig. 16, and also moment maps separately for the two components in Figs. B.3 and B.4. A largely south-to-north position-velocity cut for the field is shown in Fig. 17, with the velocity range covering both components.

The component at velocities around 3 km/s has a patchy, incoherent appearance in the moment 1 map (Fig. B.3), with an overall filamentary spatial structure. This behaviour is also reflected in the position-velocity cut in Fig. 17, where the 3 km/s component is visible between ~1 km/s and ~7 km/s, with some
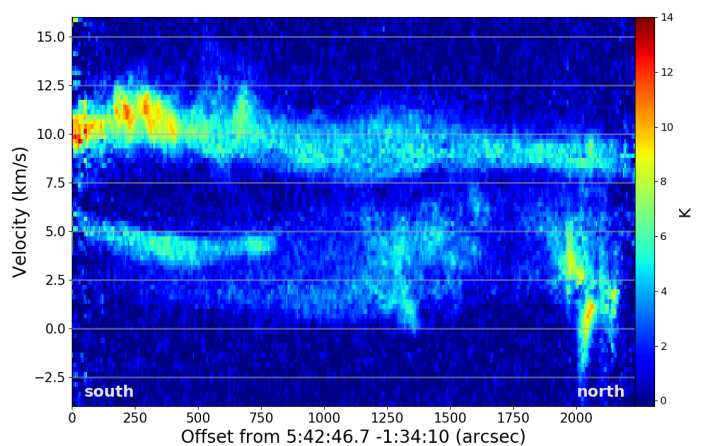
**Fig. 17.** Position-velocity cut through the Ori B9 field, starting at $5^h42^m46\overset{s}{.}7$, $-1°34'10''$ (south) and ending at $5^h43^m55\overset{s}{.}0$, $-1°01'05''$ (north).

regions of brighter, narrower emission embedded in a broad, faint, diffuse background. The presence of CO emission at velocities lower than (i.e. blue-shifted) the main cloud emission at around 10 km/s has been noted by Wilson et al. (2005), and Miettinen et al. (2009) noted the presence of N_2H^+ emission from this component as well. The cloud core harbouring the protostellar driving source of the HH 212 jet seems to be associated with the 3 km/s component (i.e. the NH_3 core associated with IRAS 05413-0104: Harju et al. (1993)), with mainly blue-shifted high-velocity CO due to this outflow seen at the northern end of the position-velocity cut. We also note some patches of faint emission at around 5 km/s in the position-velocity cuts in the NGC 2023/NGC 2024 region (Fig. 20) to the south-west of Ori B9. Together with the presence of the blue shoulder in the integrated spectrum of the NGC 2023/NGC 2024 field, this emission indicates that the 3 km/s component extends further the south-west, into the NGC 2023/NGC 2024 region.

The CO component at velocities around 10 km/s is seen at similar velocities as the bulk CO emission in the NGC 2023/NGC 2024 region located to the south-west of Ori B9. It seems to trace the north-eastern outskirts of that region, albeit it appears separated in ^{13}CO from the NGC 2024 cloud, see Caselli & Myers (1995). We see a north-south velocity gradient, with more blue-shifted CO found towards the north. Along with the shift in radial velocity we see a trend for decreasing linewidth further north.

The population of dust continuum cores in the Ori B9 region has been studied by Miettinen et al. (2009), implicitly assuming that all dust sources are associated with the main cloud component at velocities around 10 km/s. While no detection of CS emission is reported in the survey by Lada et al. (1991), the presence of dense, cold gas in the 3 km/s cloud is indicated by the detection of N_2H^+ at these velocities (Miettinen et al. 2009). Fig. 16 shows 870 μm dust continuum emission as observed with APEX (merging our own observations with those presented by Miettinen et al. 2009) overlaid as contours on the integrated CO intensity maps. We note that the compact source SMM 7 of Miettinen et al. (2009) and the ridge of fainter cores extending to its south-east correspond well to the region of brightest integrated CO emission seen in the 3 km/s cloud component. We suggest that these cores actually reside within the 3 km/s cloud, providing the second evidence of ongoing (or imminent) star formation in that cloud in addition to the HH 212 system.
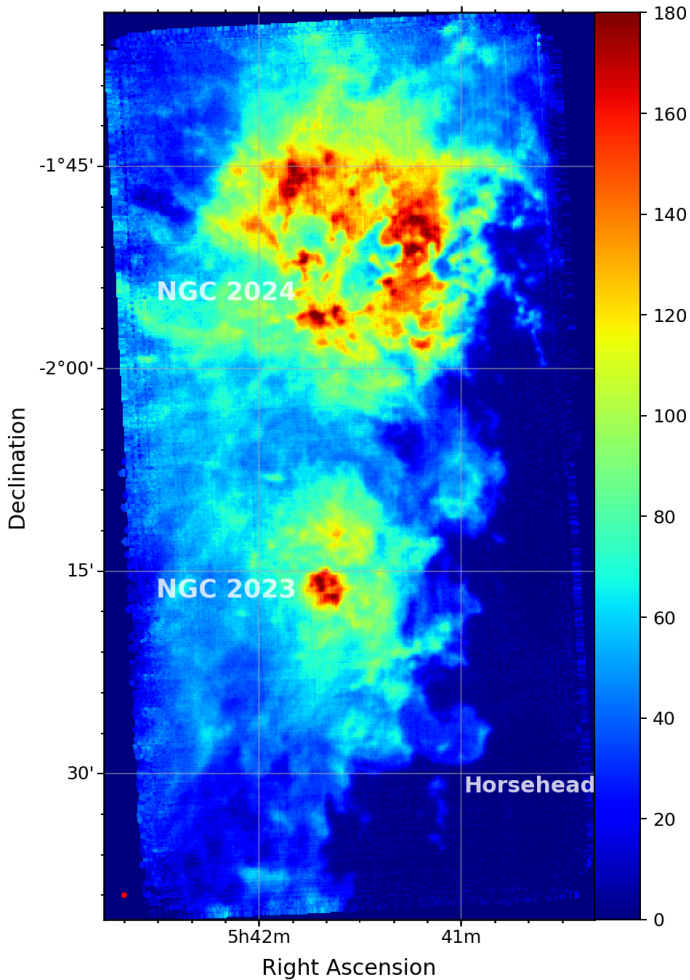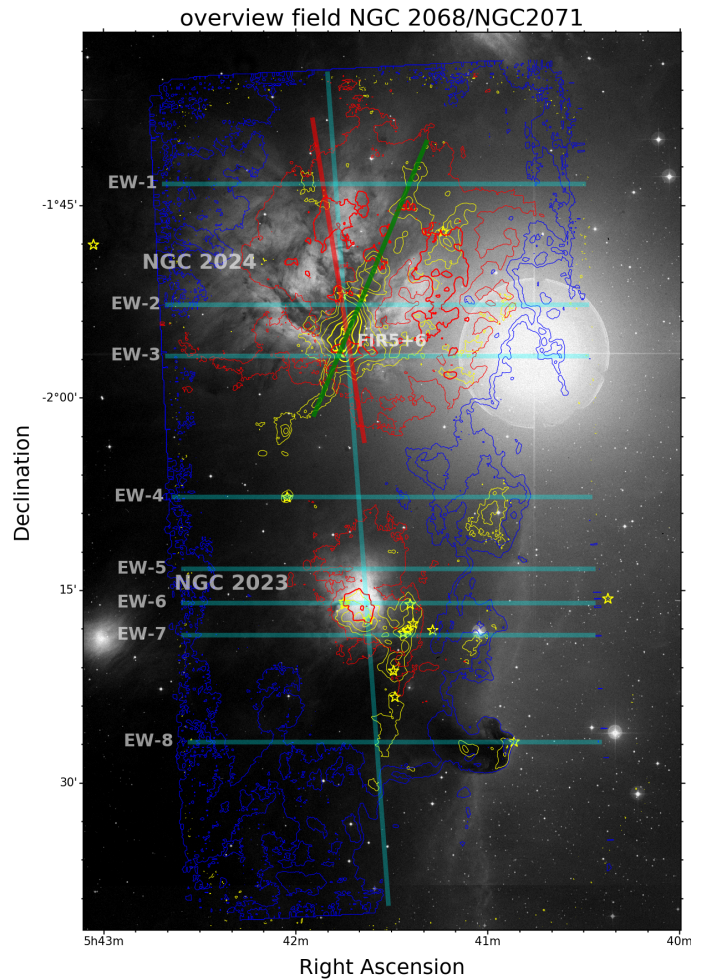
Fig. 18. CO emission in the NGC 2023 and NGC 2024 field, integrated from 6.5 km/s to 14 km/s (in K km/s) The red dot in the bottom left corner indicates the beam size.
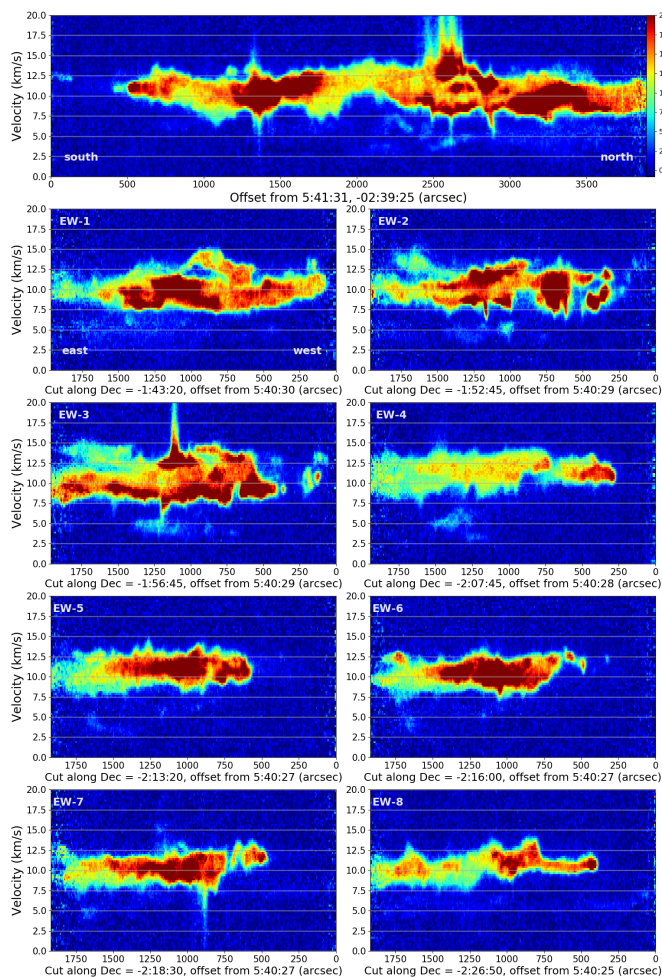

Fig. 19. Overview of the NGC 2023/NGC 2024 region, showing a DSS2-blue optical image of the region, with the integrated CO emission from Fig. 18 overplotted as blue and red (for the brightest regions) contours, and APEX Laboca 870 μm dust continuum as yellow contours. Yellow stars mark the position of HOPS protostars, and cyan lines mark the location of the position-velocity cuts shown in Fig. 20. The red line marks the cut along the NGC 2024 monopolar outflow axis (shown in Fig. 29), the green line marks the cut along the dark lane (shown in Fig. 25).

4.4. NGC 2023, NGC 2024, and Horsehead Nebula

Figure 18 shows the CO emission in the NGC 2023/NGC 2024 fields integrated over the velocity interval from 6.5 km/s to 14 km/s, and Fig, 19 shows an overview of the region, comparing optical, CO, and dust emission. Our map reproduces the main features seen in the CO(3-2) map of Kramer et al. (1996), albeit at better angular resolution. The area around the NGC 2024 H II region is seen prominently in CO emission. The CO emission in the northern and north-western part of the nebula is suggestive of being shaped by the early-type stars in the NGC 2024 cluster, showing cometary features with their heads pointing towards the centre of the nebula. Overall, the nebula also stands out in the moment 2 map (Fig. B.5) as a region of large line widths. NGC 2023 shows bright CO over the same extent as the bright optical reflection nebula, but is much smaller than NGC 2024, and hardly stands out in the moment 1 and 2 maps.

As for the overall velocity field, the moment 1 maps show a prevalence for more blue-shifted lines in and around the two optical nebulae, with more red-shifted emission between them. We also notice a trend for red-shifted emission to prevail at the western edge of the cloud, where it is exposed to the intense radiation from σ Ori.

Figure 20 shows position-velocity cuts through the NGC 2023/NGC 2024 region. The top panel shows a cut going largely from south to north, intersecting the brightest part of

the NGC 2023 nebula, NGC 2024 FIR5, and the NGC 2024 H II region. The remaining panels all show cuts going east-to-west through the cloud.

The south-to-north cut shows the large scale pattern noticed also from the moment 1 map, that is, more blue-shifted emission in the NGC 2023/NGC 2024 region, with more red-shifted emission in the very south of the region and between the two nebulae. Only one bright emission component is seen towards NGC 2023, while two or even three velocity components are seen towards NGC 2024.
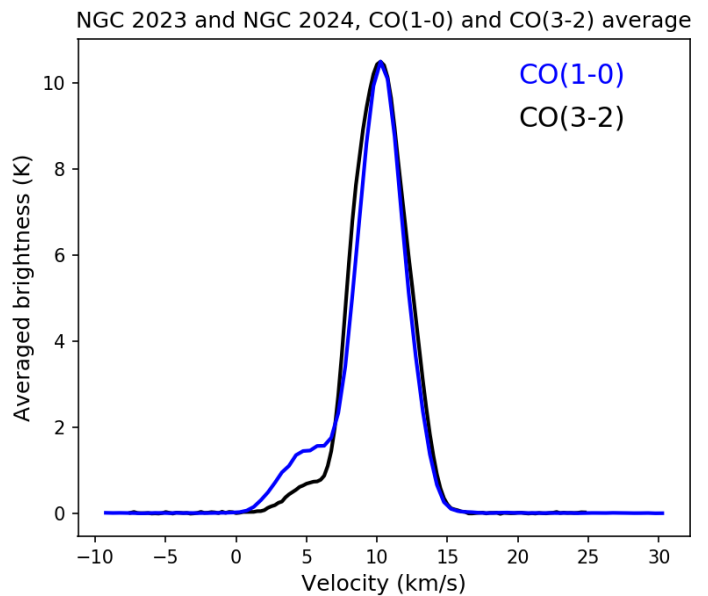
The eight east-west cuts shown in Fig. 20, EW-1 through EW-8, are ordered from north to south. The first three, EW-1 to EW-3, go through the NGC 2024 H II region. They all show a very wide overall velocity extent, with two components (locally even three) seen over much of the second and third cut. The southernmost cut of the three intersects NGC 2024 FIR5, showing strong high-velocity emission. In all three cuts, the emission at the western edge appears systematically shifted towards lower (red-shifted) velocities.

Fig. 20. Position velocity cuts across the NGC 2023/NGC 2024 survey field. Top: cut starting from $5^h41^m31^s$, $-2°39'25''$ (south), ending at $5^h41^m50^s$, $-01°34'45''$ (north). The remaining cuts go from east to west.

Fig. 21. CO(1-0) spectrum (blue), averaged over the survey field covered by Pety et al. (2017) (see their Fig. 4), and CO(3-2) spectrum, averaged over our NGC 2023/NGC 2024 survey field (black), with the CO(1-0) spectrum renormalized to the maximum of the CO(3-2) spectrum.

line profiles indicative of an expanding bubble, nor does it significantly enhance the velocity dispersion in its environment. The western edge of the cloud is systematically more red-shifted compared to the bulk of the cloud, presumably due to the influence of σ Ori to its west, which creates the IC 434 ionization front at the western surface of the cloud.
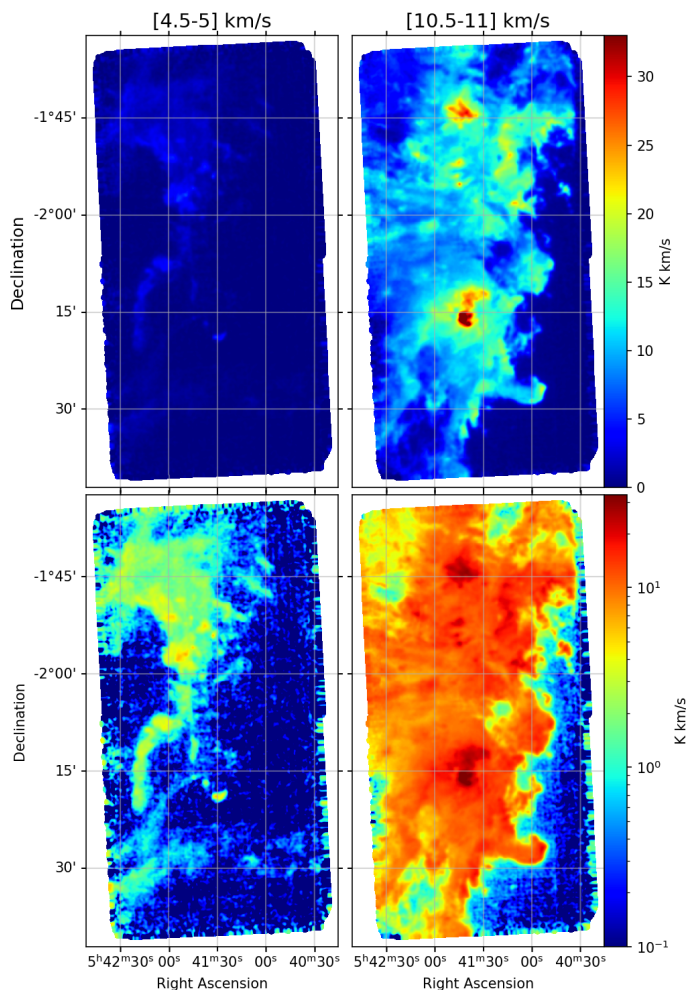
4.5. CO(1-0) versus CO(3-2) in NGC 2023/NGC 2024

The fields covered by our CO(3-2) survey overlap significantly with the area covered by the IRAM 30m 100 GHz spectral mapping survey. We provide here a comparison between our data and its CO(1-0) data as presented in Pety et al. (2017).

Figure 21 compares the CO(1-0) and CO(3-2) spectra averaged over the respective survey areas[5]. With the caveat that the areas over which the spectra have been obtained are not the same (in particular, the area covered by Pety et al. (2017) extends further to the east, that is, away from the western, UV illuminated cloud edge), the shapes of the main component of the lines compare fairly well, with some excess emission seen on the blue-shifted side of the CO(3-2) line. This secondary component at velocities around 4 km/s is comparatively much fainter than the main component in the CO(3-2) transition, by about a factor of two. We attempted to fit a double Gaussian to the CO(3-2) profile for a more direct comparison with the ratio between the two components in the CO(1-0) line derived in Pety et al. (2017), but the fit did not converge due to the more non-Gaussian shape of the main component, and the secondary component being significantly fainter than the main component.

Figure 22 shows CO(3-2) maps integrated over the same velocity ranges and convolved to the same 31″ beam as in Fig. 5 of Pety et al. (2017), to allow for a direct comparison of the CO(3-2) and CO(1-0) distributions. The map at 4.5-5 km/s, represen-

The fourth east-west cut, EW-4, is located between the NGC 2024 and NGC 2023 nebulae and shows fainter emission mostly in a single line component. The final three cuts intersect the NGC 2023 reflection nebula. All three show bright CO emission in the area of the optical nebula, but only in one velocity component. The southernmost cut shows high velocity emission associated with the outflow from NGC 2023 MM1 (Sandell et al. 1999). The emission closest to the western cloud edge in EW-6 and EW-7 again is seen to be slightly more red-shifted than the CO further east. This trend is also seen in EW-8, going through the Horsehead Nebula (B33), showing the entire 'head' and 'neck' to be redshifted compared to the emission in the western part of the cloud (for a more detailed discussion of the CO and [C I] kinematics of the Horsehead region see Bally et al. (2018)).

Taken together, the ALCOHOLS data show NGC 2023/NGC 2024 to be the most dynamic region studied in the survey. The dynamic nature of the emission can also clearly be seen when scrolling through channel maps of the line data cube. We clearly see the strong impact of the NGC 2024 H II region shaping the morphology of the surrounding gas and boosting the line width in the area. The prevalent double peaked line there suggests the presence of an expanding cavity (see Sect. 4.5.1 below). NGC 2023 has a much smaller impact on the cloud. While still creating bright line emission (presumably by heating the gas) it is neither associated with double-peaked

---

[5] Only the spectrum integrated over the full field of view covered by Pety et al. (2017) is publicly available (https://www.iram.fr/ pety/ORION-B/data.html)

Fig. 22. CO(3-2) maps over the NGC 2023/NGC 2024 survey field, integrated over the same velocity ranges (covering 0.5 km/s around the peaks of the two separate velocity components) and convolved to the same 31″ beam as in Fig. 5 of Pety et al. (2017), in linear (top) and logarithmic (bottom) intensity scaling.

Table 4. RADEX model inputs and resulting parameter ranges for the three diverse CO emission regimes in the NGC 2023/NGC 2024 region

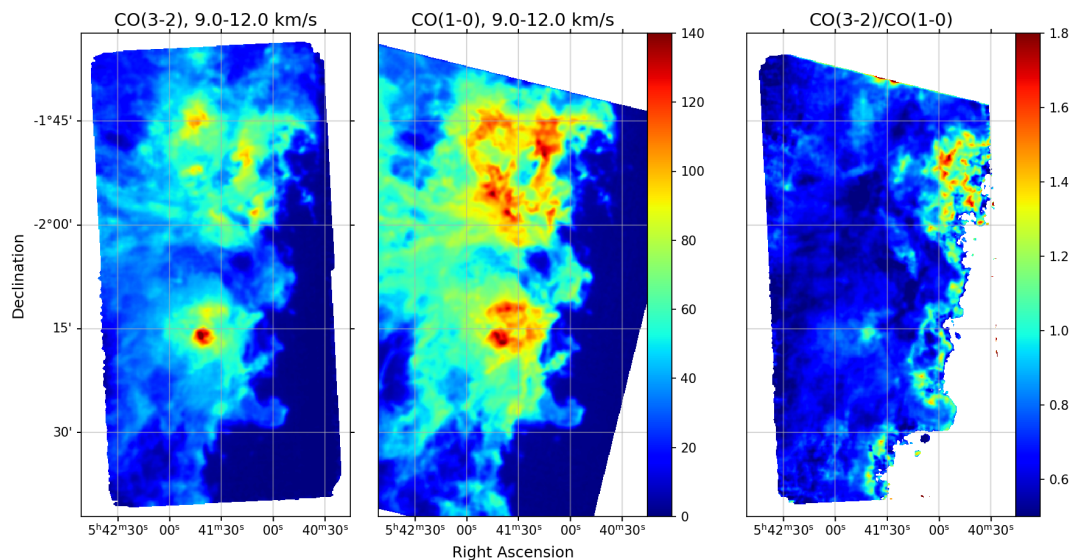|	typical	4 km/s	high excitation
CO(3-2)/(1-0)	0.5-0.75	0.25-0.4	0.9-1.8
$T_{mb}(3\text{-}2)$ (K)	8-16	< 10	2-13
$T_{mb}(1\text{-}0)$ (K)	15-23		< 10
N_{CO} (cm^{-2})	10^{17}-10^{19}	$2\cdot10^{16}$-$5\cdot10^{18}$	$5\cdot10^{15}$-$5\cdot10^{16}$
T (K)	10-60	10-50	30-200
n (cm^{-3})	10^3-10^6	10^2-10^6	$2\cdot10^2$-10^6

the main purpose of the survey, that is an unbiased search for molecular outflows.

In Fig. 23 we present a detailed comparison of the main line component, integrated over a velocity interval of 9-12 km/s, between our CO(3-2) data and the CO(1-0) data of Pety et al. (2017), where the CO(3-2) data are convolved to the same 31″ beam as used in Pety et al. (2017). The panel to the right shows the ratio of the two lines. While the absolute value of the ratio may be skewed by how exactly the integrated line maps were created, some spatial trends in the distribution of the line ratio can be seen. Over most of the area covered by both surveys, the ratio is fairly similar, at values between ~0.5 and 0.7. Interestingly, this includes the NGC 2024 H II region, which features dominantly in the line brightness maps. Assuming that generally the CO emission is optically thick, this near-constant ratio would imply relatively small variations of the gas temperature over the field, even in the gas associated with the NGC 2024 H II region. As can be seen in the following Section 4.5.1, however, the brightest emission in the NGC 2024 H II region actually falls just outside the velocity range used for the integrated intensity, particularly on the blue-shifted side, so velocity-resolved line-ratio maps would probably show a different picture.

Higher line ratios are found in the NGC 2023 nebula, over a fairly small area, and all along the western edge of the cloud. In NGC 2023, the area of high line-ratio coincides with bright line emission, consistent with the presence of warm, optically thick molecular gas. In contrast, the areas of high line-ratio along the western cloud edge predominantly arise in comparatively faint CO emitting regions. This behaviour is further illustrated in Fig. 24, plotting the distribution of line ratios against brightness in the CO(1-0) and CO(3-2) lines. Fig. 24 also shows that the line ratios over most of the cloud are at fairly uniform values, with high line ratios found associated mainly with fainter line emission. Apparently the regions with high line ratios trace the warm molecular gas, presumably with low optical depth, associated with the PDR at the western edge of the Orion B cloud. NGC 2023 and the western cloud edge are in fact also seen as regions of elevated dust temperature (e.g. Lombardi et al. 2014), whereas the high dust temperatures in NGC 2024 are not reflected in correspondingly higher line ratios (in the velocity interval used for the line integration used in Pety et al. (2017) and here).

In Appendix C we present exploratory RADEX (van der Tak et al. 2007) radiative transfer modelling of the CO emission in the CO(3-2) and CO(1-0) lines, in order to constrain the differences in physical properties of three characteristic emission regimes: the multi-colour scale in Fig. C.1 represents models reproducing the 'typical' emission, which according to Fig. 24 is characterized by CO(3-2)/CO(1-0) line ratios around 0.6, a CO(1-0) brightness temperature around 20 K (i.e. 60 K km/s if integrated over 3 km/s), and a CO(3-2) brightness temperature around ~12 K (~35 K km/s if integrated over 3 km/s). The

tative of the secondary line component, shows that our CO(3-2) survey covers the majority of the secondary component as seen in the CO(1-0) map, thus the low ratio with respect to the primary component (as compared to the ratio in the CO(1-0) line) is unlikely due to the CO(3-2) survey missing a significant part of the secondary component. Similarly, no significant part of emission in the main line component is missed by the CO(1-0) map, thus the difference in the ratios between main and secondary components between the (3-2) and (1-0) lines is most likely real. This difference may indicate that the secondary component traces a layer of molecular gas that is colder and more optically thin than the main component.

Overall the CO(3-2) map of the secondary component corresponds well to the CO(1-0) maps in terms of the structures detected. The streak of emission running east-west around the declination of the Horsehead Nebula seems comparably fainter in the CO(3-2) maps, which in part may be due to the fact that the bulk of this feature is at slightly lower velocities (as can be seen from the southern-most E-W oriented position-velocity cut at the bottom right of Fig. 20). Perhaps the most noteable difference is the much more prominent appearance of the blue-shifted lobe of the outflow driven by NGC 2023 MM1 (Sandell et al. 1999) in the CO(3-2) map, confirming that CO(3-2) is well suited for
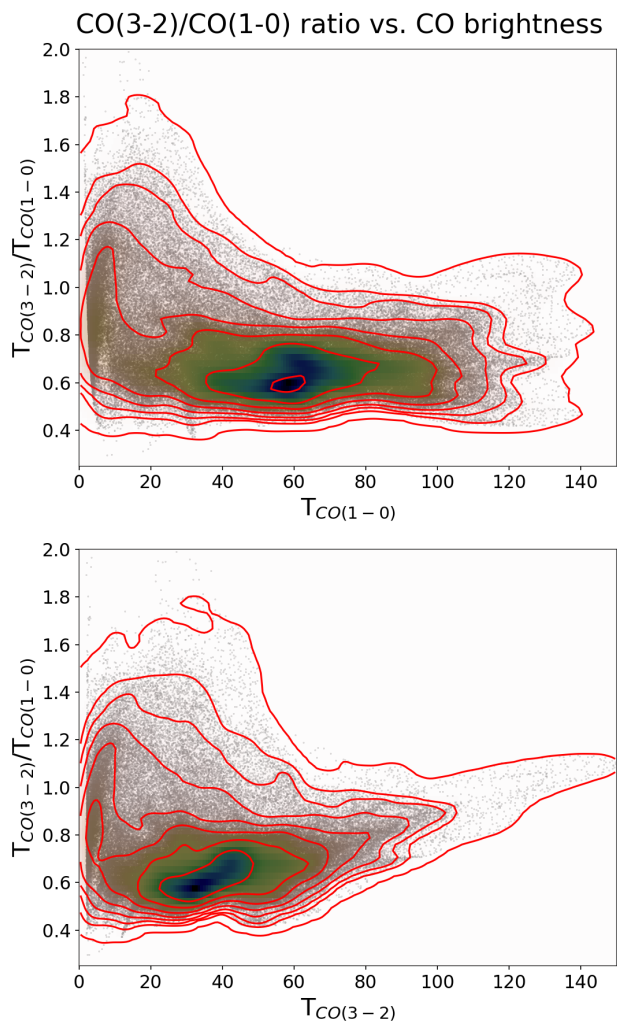
Fig. 23. CO(3-2) map over the NGC 2023/NGC 2024 survey field, integrated over the same velocity range (9-12 km/s) and convolved to the same 31″ beam as in Fig. 2 of Pety et al. (2017), along with their CO(1-0) velocity integrated map, and the ratio of the CO(3-2)/CO(1-0) maps (where the ratio was computed for all pixels with a CO(3-2) line brightness temperature greater than 2 K, i.e. excluding pixels with noisy ratios due to low signal-to-noise ratios).

red colour scale in Fig. C.1 corresponds to models resembling the 'low excitation' emission, corresponding to the ~ 2 times lower CO(3-2)/CO(1-0) line ratio inferred for the velocity component around 4-5 km/s, which we assume to be characterized by CO(3-2)/CO(1-0) line ratios around 0.3 and a CO(3-2) brightness temperature less than 10 K (the maximum brightness seen in our line cubes for this velocity component). The blue colour scale in Fig. C.1 shows the parameter range reproducing the 'high excitation' emission reflecting the conditions at the western cloud edge, with CO(3-2)/CO(1-0) line ratios greater than 0.9 and brightness temperatures less than 13 K and 10 K for the CO(3-2) and CO(1-0) lines, respectively.

Table 4 summarizes the restrictions in terms of line ratios and line brightnesses imposed on the RADEX models representing the three distinct emission regimes, as well as the ranges of CO column densities, temperatures, and densities that yield models reproducing the respective observed line properties. For all three regimes we find that, in principle, wide ranges in CO column densities, temperatures, and H_2 densities may yield CO emission consistent with the respective input restrictions. Nevertheless, we can identify some trends. Regardless of the emission regime and column density considered, there is a general degeneracy between density and temperature, and valid models reproducing a certain set of constraints at a given column density typically fall into a narrow stripe in the density-temperature plane, with lower temperatures requiring overall higher densities. Varying the column density typically leads to a shift of that stripe, with lower column densities usually requiring a combination of higher temperatures and densities, that is, shifting the stripe in the density-temperature plane upwards and to the right. Additional observations would be needed to further limit the physical conditions of the gas, in particular, rarer CO isotopologues (^{13}CO) should help to constrain the CO column density, while additional transitions should help to further constrain the gas temperature. As an additional caveat, it has to be kept in mind that the CO(3-2) and (1-0) lines may have a different beam filling factor, for example warmer gas emitting stronger in the (3-2) transition might be limited to smaller volumes.

Despite the wide range in parameters allowed for each of the three emission regimes considered, we can identify some physical differences between them. In terms of column density, the 'typical' emission requires the highest CO column densities (no models meet the restrictions imposed for column densities $N < 10^{17} \mathrm{cm}^{-2}$), the 'high excitation' component requires the lowest CO column densities ($< 10^{17} \mathrm{cm}^{-2}$), while the 'low excitation' component of the 4-5 km/s cloud requires CO column densities around $10^{17} \mathrm{cm}^{-2}$, intermediate between the 'typical' and the 'high excitation' component. This indicates that the 'typical' component indeed traces the high column density bulk molecular gas of the GMC, while the 4-5 km/s 'low-excitation' emission traces a significantly more tenuous cloud. In terms of temperature and density the 4-5 km/s 'low-excitation' might not be too different from the bulk cloud, with temperatures less than $\sim$50 K. In particular if the lowest densities considered are excluded, as they would imply unrealistically large cloud extents along the line of sight, temperatures for both components should be well below 40 K.

In contrast, we find that the 'high excitation' component most probably requires significantly higher temperatures >40 K (with temperatures as low as $\sim$30 K possible only for very high densities). This is similar to the findings of Zhang et al. (2019) in a study of ^{12}CO(3-2)/(2-1)/(1-0) line ratios in the N131 dust bubble, who see high line ratios outlining the inner rim of the bubble. They attribute the high line ratios to the high temperatures and pressure generated by the impact of the massive hot stars creating the bubble. While our RADEX models do not provide unambiguous evidence for higher pressure in the high excitation component, it seems clear that the temperature is significantly higher than in the bulk of the molecular cloud. We conclude that the 'high excitation' component seen along the western cloud edge indeed corresponds to warm gas heated and possibly compressed by the incident UV radiation field. The 4-5 km/s 'low-excitation' emission instead indicates a fairly cool cloud not exposed to significant irradiation and might trace a tenuous cloud in the fore- or background of the Orion complex, at a significantly larger physical distance from the OB stars creating the
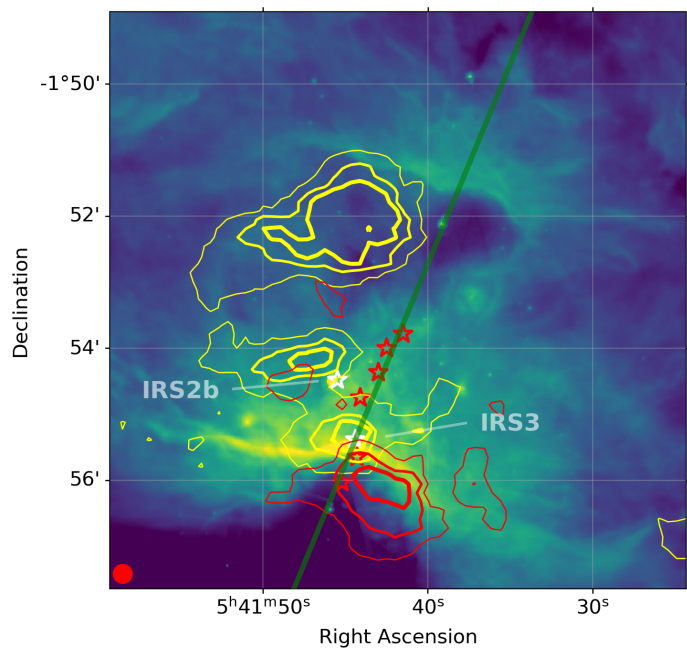
CO(3-2)/CO(1-0) ratio vs. CO brightness

Fig. 24. CO(3-2)/CO(1-0) line ratios in the NGC 2023/NGC 2024 survey field as a function of CO line brightness.
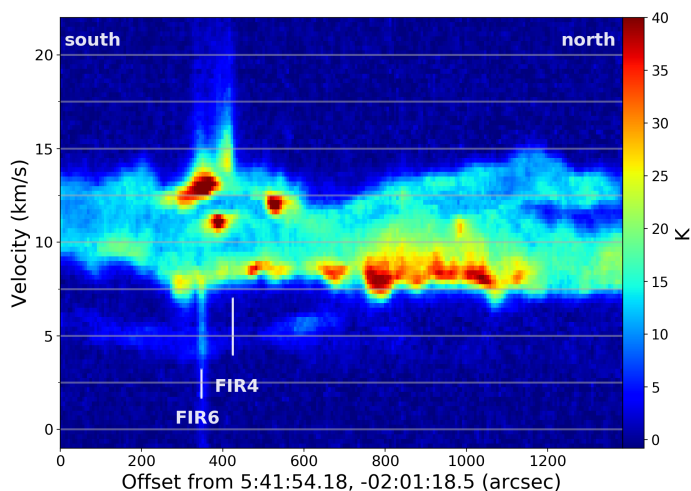
Fig. 25. Position-velocity cut along the NGC 2024 dark lane along the green line shown in Figs. 19, 26, and 27.

IC 434 ionization front at the western edge of the bulk cloud in the NGC 2023/NGC 2024 region.

Fig. 26. Spitzer IRAC4 (8.0 μm) image of the central NGC 2024 region (logarithmic colour scale) overlayed with contours of CO(3-2) emission at 10.75 to 11.25 km/s (yellow) and 12.75 to 13.25 km/s (red); red stars mark the positions of FIR1 to 6 from Mezger et al. (1988), the green line marks the location of the position-velocity cut shown in Fig. 25. The red circle in the lower left marks the beam size of the CO(3-2) maps.

4.5.1. The NGC 2024 H II region

The basic picture of the structure of the NGC 2024 H II region is summarized, for example, in Fig. 6 of Matthews et al. (2002). It is a blister-type H II region opening towards the north, east, and west, but bounded to the south (Barnes et al. 1989). A dense ridge of molecular cores (Mezger et al. 1988, 1992) is located in the background cloud at the southern end of the H II region. A layer of foreground material protruding from the main cloud at the southern end of the H II region causes the prominent dark optical lane running through the middle of the nebula, while the bulk of the cloud is thought to be located behind the H II region. A cluster of young stars is found in infrared images of the region (e.g. Barnes et al. 1989; Bik et al. 2003), with the source IRS2b, having a late O-type spectrum, identified as the most likely exciting source of the H II region (Bik et al. 2003).

The structure of the gas towards the dense ridge has been the subject of previous investigations that attempted to explain the profiles of CO lines in the direction of FIR5 with a wide range of upper energy levels and including various isotopologues (e.g. Graf et al. 1993; Emprechtinger et al. 2009). The resulting structure along the line of sight corresponds to the picture sketched above, with the bulk of the molecular gas behind the H II region at velocities of ~11 km/s and a thinner foreground layer with a velocity of ~9.3 km/s. Both of these layers are separated from the H II region by thin layers of warm molecular gas representing the interfacing PDRs. An additional cold foreground layer is postulated to explain the depression of the CO low-J main isotopologue lines at 12 km/s, where the location and extent of that foreground layer remains unclear.

Figure 25 shows a position-velocity cut through the NGC 2024 H II region along the optical dark lane, as indicated by the green line in Figs. 19, 26, and 27. Our data reproduce the complex CO(3-2) line shapes seen there before. For example, a

double peaked line noted by Graf et al. (1993) is seen immediately south of FIR6, while three peaks noted by Emprechtinger et al. (2009) are seen between FIR6 and FIR4. We also see substantial variations in the line properties. For example, the number of emission and absorption components and their respective velocities and brightnesses can change dramatically even on sub-arcminute spatial scales.

The absorption dip at ~12 km/s drifts by a few velocity channels (i.e. by more than 0.5 km/s) over just 60″ around the position of FIR5, while only 2′ further north bright emission is seen at the same velocity. The bright emission component at intermediate velocities (around ~11.0 km/s) is seen as a small, but clearly resolved patch in the channel maps (green contours in Fig. 26). It coincides with the brightest portion of the rim seen at infrared wavelengths marking the PDR at the southernmost boundary of the H ɪɪ region (e.g. Gaume et al. 1992; Watanabe & Mitchell 2008; Ren & Li 2016). This location marks both the smallest separation between the infrared rim and the main ionizing source IRS2b, and the location of IRS3, which was once proposed as a possible ionizing source and which is actually a small group of stars (Bik et al. 2003). Either IRS2b or IRS3 seem to heat the molecular gas around this location. The bright emission at ~13 km/s (red contours in Fig. 26) is seen south of the bright infrared rim, with the rim precisely curving around its northern edge. The shape of the infrared rim suggests that the H ɪɪ region at the southern end is bounded by a dense clump, around which the PDR is wrapping, and to which the most red-shifted CO emission at 13 km/s is associated. FIR5 and FIR6 are seen (in projection) towards this clump, but might still be located further in the background. The radial velocities of the gas in the FIR1-6 dense ridge itself ranges between <10 km/s to 11 km/s (e.g. Gaume et al. 1992; Watanabe & Mitchell 2008; Ren & Li 2016), that is, slightly less redshifted than the rear cloud wall bounding the H ɪɪ region, indicating that only the surface layer of the cloud has been accelerated by the pressure from the H ɪɪ region and is moving into the densest portion of the cloud.

The basic picture of a more red-shifted background molecular component and a more blue-shifted foreground component provides a plausible explanation of many features seen in previous multi-line, multi-isotopologue CO line studies. In particular, it explains the double-peaked profiles of low-J, low opacity isotopologue lines. The true three dimensional structure of the CO emitting gas at the southern end of the H ɪɪ region, however, is clearly more complex. For example, Emprechtinger et al. (2009) assume layers with constant velocities and no spatial substructure over the 80″ beam used in their study towards the position of FIR5. A fuller understanding will require multiline observations at substantially better spatial resolution and adequate spatial sampling of the region.

Going further north along the dark lane, we observe a gradual increase in the maximum red-shifted extent of the line, from ~12 km/s at an offset of ~650″ up to ~15 km/s at an offset of ~1200″. The blue-shifted maximum velocity remains roughly constant (apart from some wiggles) at ~7-7.5 km/s. The brightest emission is consistently seen at the most blue-shifted edge of the line in the position-velocity diagram. In Fig. 27 we compare the spatial distribution of the blue-shifted CO(3-2) emission (using a single channel of the CO(3-2) cube at a velocity of 8 km/s) with an optical image (Digitized Sky Survey: DSS2-blue), which shows the distribution of obscuring dust in the foreground of the H ɪɪ region. A number of structures correspond well between the two maps. In particular, the western rim of the optical dark lane coincides with a sharp drop in CO intensity. This drop in CO emission is also clearly seen in maps of velocity-integrated ^{13}CO

emission (e.g. Subrahmanyan et al. 1997; Buckle et al. 2010). It is not clearly apparent, however, in the velocity integrated ^{13}CO maps shown in Pety et al. (2017) as their velocity interval (9-12 km/s) excludes the majority of the blue-shifted component. The ^{13}CO channel maps shown in Enokiya et al. (2021) also suggest that in the northern part of the cloud this blue-shifted component dominates the total emission. Overall, this indicates that the blue-shifted component contributes very significantly to the total CO column density at least towards the northern part of the H ɪɪ region. The good correspondance between the blue-shifted CO distribution and the optical obscuration clearly places the blue-shifted molecular gas in the foreground of the H ɪɪ region.

Taken together, our data suggest a revised model for the NGC 2024 H ɪɪ region, particularly for its northern. The more blue-shifted CO(3-2) emission clearly traces a layer in the foreground of the H ɪɪ region. As it is significantly brighter in our ^{12}CO data, and as it also seems to dominate ^{13}CO maps, we argue that the foreground, more blue-shifted CO actually traces the bulk of the cloud column density in the area. We see the brightest line emission at the most blue-shifted velocities, tracing a warm layer interfacing the molecular foreground cloud and the H ɪɪ region, and being pushed towards us (to slightly higher velocities than the bulk foreground cloud) by the H ɪɪ region. Overall the bulk velocity of the blue-shifted component does not change systematically with increasing distance from the central cluster, indicating that the gas there is too massive to be accelerated as a whole by the impact of the H ɪɪ region. The red-shifted CO then traces the molecular gas behind the H ɪɪ region. The increasing red-shift with distance from the ionizing cluster could indicate that we see the (southern) edge of an inflating bubble, or that the amount of gas decreases with distance from the cluster and is thus more easily accelerated to larger velocities. This situation would be comparable to that found in the Orion Nebula (albeit seen here 'from behind'), where blue-shifted [C ɪɪ] emission traces a thin foreground layer that is accelerated by the expanding H ɪɪ region, while the background layer remains at a roughly constant velocity of the bulk background cloud (Pabst et al. 2020). Finally, observations of hydrogen radio recombination lines show increasingly blue-shifted velocities towards the north (Krügel et al. 1982; Subrahmanyan et al. 1997), which could be explained as an accelerating flow directed north and inclined towards the observer. Consequently, the foreground molecular layer must also be inclined towards the observer.

4.5.2. The NGC 2024 collimated outflow

The presence of high velocity CO emission in the NGC 2024 area was first noticed by Bally & Lada (1983). First mapping observations by Sanders & Willner (1985) indicated a bipolar outflow with its highly collimated red-shifted lobe extending south, and blue-shifted emission to the north. Subsequent observations (Richer et al. 1989, 1992) did not confirm the northern, blueshifted lobe, making the NGC 2024 outflow a rare example of a monopolar protostellar outflow. The proposed driving source of the outflow is the sub-millimetre condensation NGC 2024 FIR5, the brightest condensation in a chain of 7 running along a north-south high column density ridge (Mezger et al. 1988, 1992). The reason for the absence of the blue lobe is not entirely clear, but has been attributed to NGC 2024 FIR5 being located immediately south of a PDR interfacing the dense core and the NGC 2024 H ɪɪ region.

Figure 28 shows the distribution of high velocity CO emission in the central NGC 2024 region, and Fig. 29 shows a position-velocity cut along the outflow axis, marked by the red
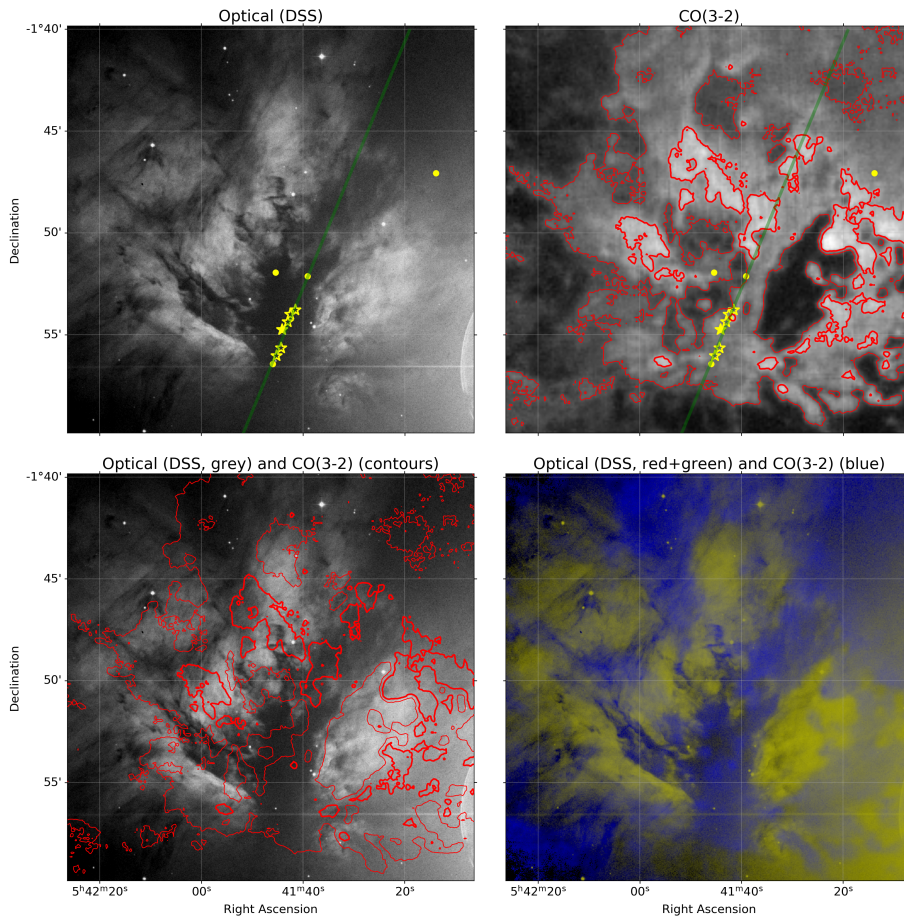
Fig. 27. Comparison of the NGC 2024 H II region at optical wavelengths and CO(3-2) emission at 8 km/s. The panel to the top left shows a DSS2-blue image; yellow stars mark the location of the sub-millimetre cores FIR1 to FIR6 (counting from north to south; Mezger et al. 1988), yellow dots mark HOPS protostars in the field, the green line marks the location of the position-velocity cut shown in Fig. 25. The panel to the top right shows the CO(3-2) emission in a single velocity channel at 8 km/s (greyscale and contours). The bottom left panel shows an overlay of the CO(3-2) 8 km/s velocity channel (using the same contour levels as in the upper right panel) on the DSS2-blue image, the bottom right panel shows a colour-composite image, where the optical DSS2-blue image is shown in the red and green channels, and CO at 8 km/s in the blue channel.

line in Fig. 28 and Fig. 19. We clearly detect red-shifted high-velocity emission with a spatial distribution and kinematic structure very similar to previous observations (see e.g. Fig. 4 of Richer et al. (1989) for a comparison in position-velocity space, and Buckle et al. (2010) for a CO(3-2) high velocity emission map).

The redshifted lobe extends north-south, starting from the position of FIR4, passing just west of the position of FIR5. In position-velocity, space the upper envelope in velocity shows the maximum velocity in the lobe increasing steadily from north to south in a 'Hubble-type' flow. This increase in maximum velocity starts at FIR4 and continues towards the southern end of the lobe without any noticable change or feature visible at the position of FIR5. We hence propose that FIR4 is the actual driving source of the outflow. In fact, this identification is consistent with a number of observations reported in the literature. Richer et al. (1992) note the existence of red-shifted emission north of FIR5, but discard a driving source further north. The CO(3-2) map of Buckle et al. (2010) also show the red-shifted lobe to extend up to FIR4. Meanwhile, Chandler & Carlstrom (1996) detect red-shifted outflow emission to the south of FIR4. They see the brightest emission extending towards the south-east from FIR4, but faint and more diffuse emission is also seen to its south and south-west, possibly indicating a conical base of a south-oriented outflow. Certainly these early interferometric

observations are compromised by poor sensitivity and uv coverage. Perhaps even more interestingly, the CS(2-1) maps in the same paper show two filaments first extending to the south-east and south-west of FIR4, respectively, then both turning towards a more southerly orientation. These filaments could indicate the walls of an outflow cavity extending south of FIR4. Alves et al. (2011) present SMA interferometric CO(3-2) observations of the FIR5/6 region and find two nearly parallel, north-south oriented filaments of red-shifted emission at intermediate velocities (with an additional north-south oriented filament at higher velocities located between the lower-velocity filaments). They suggest that the eastern filament is driven by FIR5, and the western filament is either driven by a separate, fainter continuum peak along the filament or is part of a precessing outflow from FIR5, along with the high-velocity filament. We instead propose that the two filaments at intermediate velocity trace the eastern and western edge of a single outflow lobe originating further north. The lack of CO detection at similar velocities between the filaments may either indicate a hollow outflow structure, or (more likely) is due to filtering of extended emission by absent short spacings in their observations. Chernin (1996) argue that FIR5 may not be the driving source, but propose that its origin is in a still undiscovered low-mass young stellar object rather than any of the FIR sources of Mezger et al. (1988) and Mezger et al. (1992).
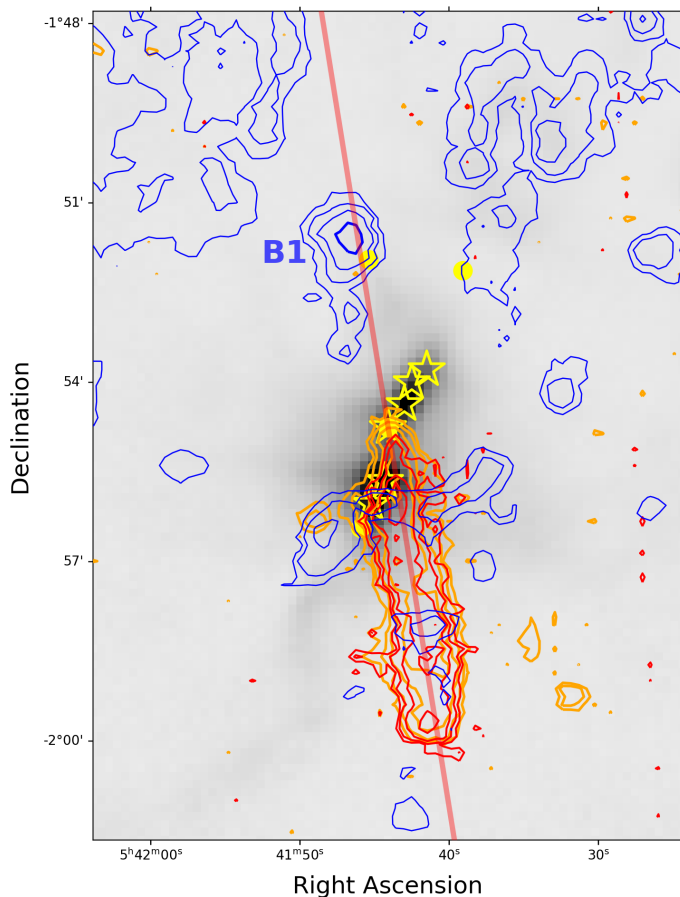
Fig. 28. Maps of high-velocity CO emission in the central NGC 2024 region. Greyscale: Laboca 850 μm continuum emission. Orange contours: CO emission integrated from 16.0 km/s to 19.75 km/s. Red contours: CO integrated from 20.0 km/s to 36.0 km/s. Blue contours: CO integrated from 5.5 km/s to 7.0 km/s. Yellow stars mark the positions of the 1.3 mm dust continuum cores FIR1 to FIR6 (counting from north to south, from Mezger et al. (1988)), while yellow dots mark HOPS protostars (where FIR4 coincides with HOPS 384). The red line marks the position of the velocity cut shown in Fig. 29.

Choi et al. (2015) describe a radio continuum jet and water maser features which line up in a north-north-west to south-south-east orientation (position angle $-25°$, broadly consistent with the orientation of the brightest part of the red-shifted CO outflow found by Chandler & Carlstrom (1996). This might either indicate a second flow, or a variation of outflow direction with time. In fact, at large scales the red lobe shows evidence for some wiggling, as seen in the maps of Sanders & Willner (1985), Richer et al. (1992), Buckle et al. (2010), and in the present data. Finally, we note that recent ALMA observations taken with the 7m ACA array also show a redshifted, conical outflow lobe opening towards the south of FIR4 (Megeath, pers. comm.), broadly consistent with Chandler & Carlstrom (1996), and perfectly coinciding with the northern end of the large-scale red-shifted lobe.

FIR5 (the brightest of the sub-millimetre cores identified by Mezger et al. (1988) and Mezger et al. (1992)) was originally proposed as driving source, as the large mass/momentum/energy of the flow requires at least an intermediate-mass object as driving source. The newly proposed driving source FIR4 corresponds to HOPS 384, a Class 0 protostar with a bolometric luminosity $L_{bol} = 1478 L_{\odot}$, that is, also an intermediate-mass object, and thus consistent with the original postulation.
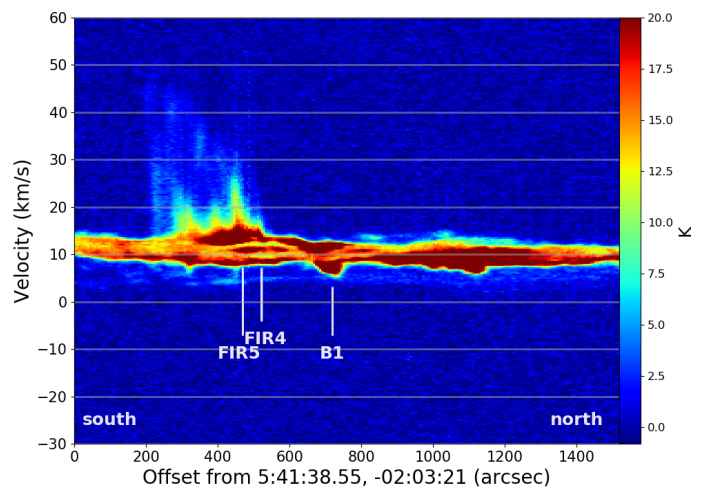
Fig. 29. Position velocity cut along the NGC 2024 outflow axis, starting from $5^h41^m38\overset{s}{.}55$, $-2°03'21''$ (south), ending at $5^h41^m54\overset{s}{.}65$, $-01°38'20''$ (north; marked with a red line in Fig. 19 and Fig. 30).
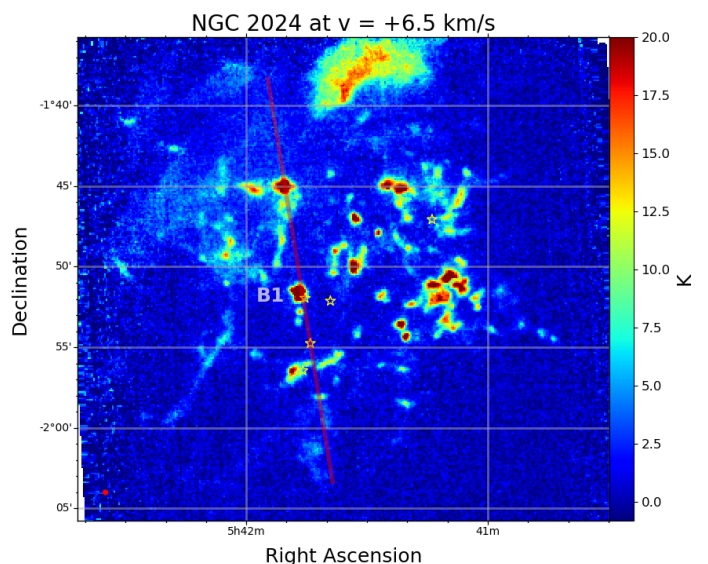
Fig. 30. Map of the CO emission in the NGC 2024 region in a single velocity channel at $+6.5$ km/s, showing the highly fragmented distribution of emission features at this moderately blue-shifted velocity. The red line shows the location of the position-velocity cut along the NGC 2024 outflow axis shown in Fig. 29. The red dot in the bottom left corner indicates the beam size.

We also note that the emission from the red-shifted lobe seems to curve around the continuum emission of FIR5, as seen more clearly in the slightly higher angular resolution JCMT map of Buckle et al. (2010)). We propose that the outflow lobe is located behind the FIR5 core and that the dust in the centre of that core is optically thick enough to absorb the CO emission in its background. This scenario is in line with the notion that FIR5 and FIR6 are seen immediately south of the ionization front at the southern boundary of the NGC 2024 H II region, and FIR1-4 are located just behind the southernmost part of the H II region.

The blue-shifted counterlobe remains elusive. While we detect the east-west oriented, mostly blue-shifted flow attributed to FIR6 (see Fig. 28), we do not detect any emission at blue-shifted velocities north of FIR4 that could obviously form a counterlobe to the prominent red-shifted outflow lobe south of FIR4. Figure 28 shows a roundish patch of blue-shifted emis-

sion about 3.′3 north of FIR4, which corresponds to a triangular feature in the position-velocity diagram of Fig. 29 extending towards velocities lower than the region's systemic velocity. We refer to this feature as B1 in the following. It is accompanied by two smaller blobs to its south, which also show clear blue outflow line wings in their spectra. Further north (outside the field shown in Fig. 28) the position-velocity diagram in Fig. 29 shows another slow increase towards blue-shifted velocities, which is however much less clearly separated from the region's systemic velocity in the north. Both features are also visible in the channel map in Fig. 30, which shows a map of the CO emission in a single, 0.25 km/s wide spectral channel, along with a population of compact, bright, slightly blue-shifted blobs seen scattered over the entire area of the NGC 2024 H ɪɪ region.

It remains to be seen whether this population of blue-shifted blobs are due to outflows driven by the embedded young stellar object population in the area, or whether it is just a signpost of the complex kinematics of the molecular gas in front of the NGC 2024 H ɪɪ region. The location of the blue-shifted feature B1 on the axis defined by the red-shifted outflow lobe, and its size, which is comparable to the east-west diameter of the red-shifted lobe at similar separations from FIR4, however, leads us to speculate that it marks the location where the blue counter-lobe of the FIR4 flow punches through the layer of foreground molecular gas. In this picture, FIR4 is embedded in a dense ridge behind the H ɪɪ region (but very close to the surface of the molecular material). The northern flow immediately enters the H ɪɪ region, and first remains invisible in molecular lines, as there is no molecular gas to entrain, and any molecules in the flow very quickly are dissociated. It then enters the foreground molecular layer, where it can entrain molecular gas over some distance and accelerate it to modest velocities. Then, it leaves the molecular layer after a short distance, where molecules are dissociated again as they are exposed to the ambient UV field.

4.6. L 1641-S

The spectrum integrated over the entire L 1641-S survey field shows two velocity components (Fig. 6). Figure 31 shows maps of the CO emission integrated over the velocity ranges corresponding to each component. We see the cloud component with velocities around 6 km/s mainly in the north-western part of the mapped field, getting fainter towards the south. The 3 km/s component is brightest around the location of the L 1641-S cluster and its associated reflection nebula (Strom et al. 1993; Carpenter 2000; Allen & Davis 2008; Megeath et al. 2016; Pillitteri et al. 2013) and extends mostly to its south.
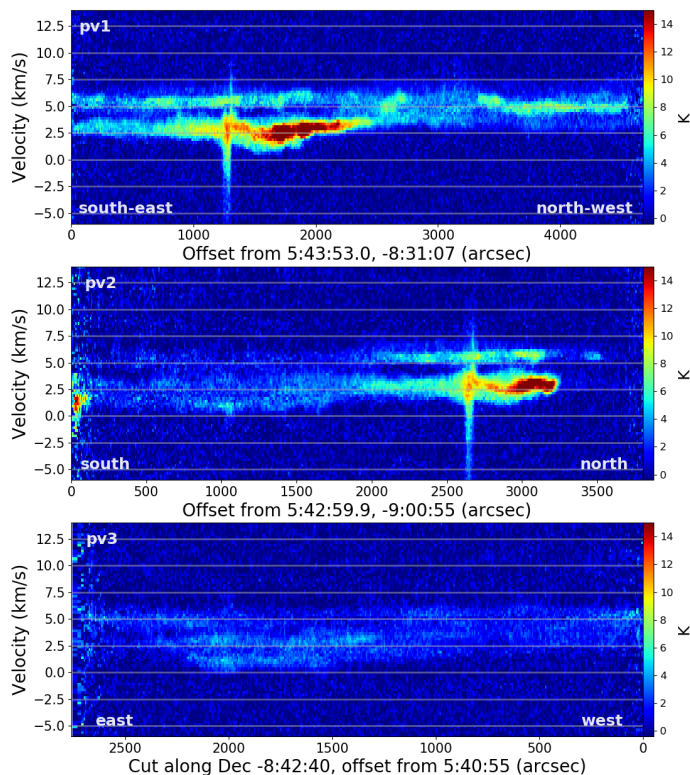
Figure 32 shows position-velocity cuts through the L 1641-S field. The top panel shows a cut going south-east to north-west through the northern part of the survey field, intersecting the L 1641-S cluster area (bright emission in the 3 km/s component around offsets of 2000″). Further to the north-west, the two components become entangled, and in the north-westernmost part, the 6 km/s component becomes the brightest (with a velocity centred around 5 km/s). The panel in the middle shows a south-to-north cut through the eastern part of the survey field, again intersecting the L 1641-S cluster area at its northern end. The 3 km/s CO emission has a sharp edge in the north. Overall its shape, particularly in individual channel maps at velocities around 2 km/s, is that of a large cometary cloud, with its head pointing north and the tail opening to the south. In the southern part of the position-velocity cut the 3 km/s component seems to split up again, showing an additional velocity component at
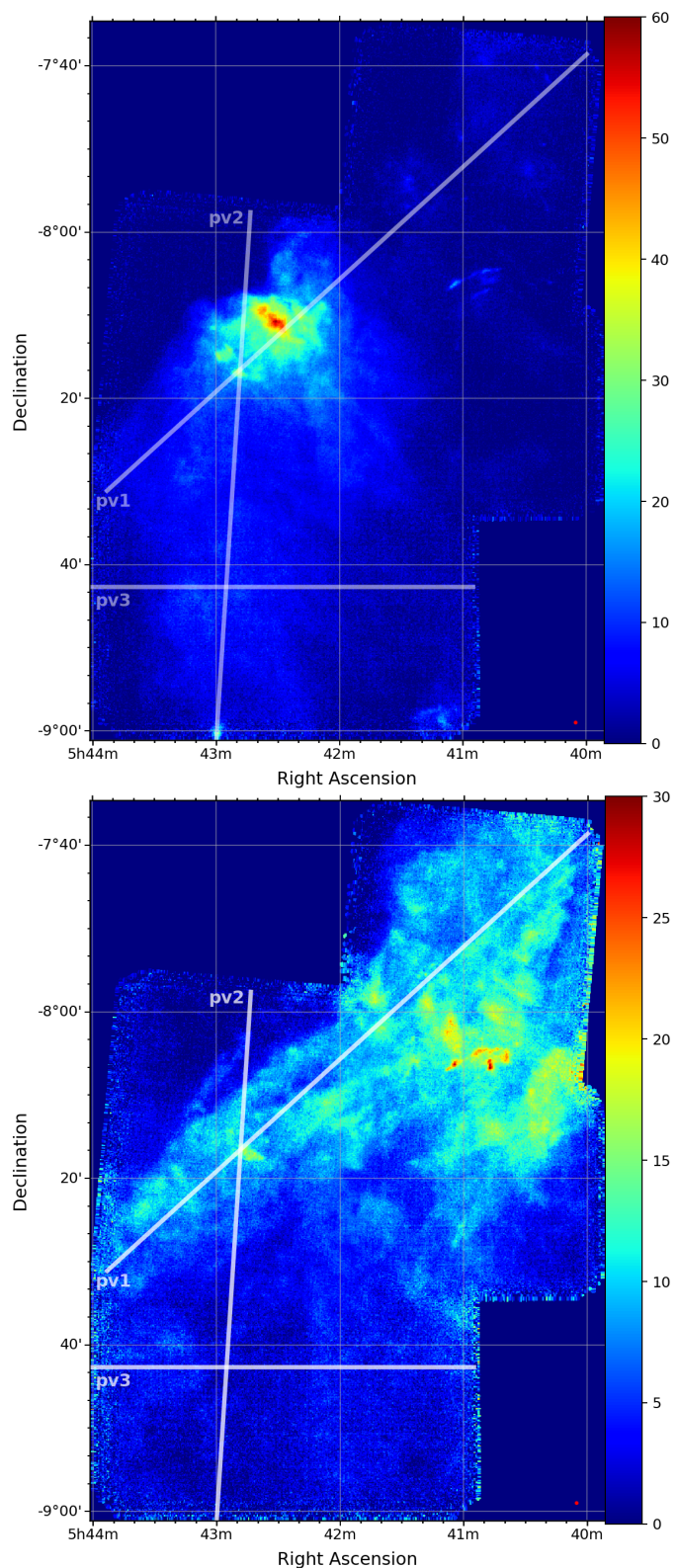
Fig. 31. CO emission in the L 1641-S field, integrated from 0.5 km/s to 3.5 km/s (top, in K km/s) and from 4.5 km/s to 7.25 km/s (bottom) The red dot in the bottom right corner indicates the beam size.

around 1 km/s. This third component is seen more clearly in the east-west position-velocity cut shown in the bottom panel.

A large-scale north-to-south velocity gradient over the Orion A cloud has long been known (e.g. Bally et al. 1987; Wilson et al. 2005), with the gas exhibiting increasingly more

Fig. 32. Position-velocity cuts through the L 1641-S field. See Fig. 31 for definition.

blue-shifted velocities further south. Hacar et al. (2016) showed that the stars associated with the cloud follow the same trend in their radial velocities. There is also mounting evidence that the L 1641 cloud has a significant extent perpendicular to the plane of the sky, with the northernmost part being at around 400 pc, and the southernmost areas at up to 500 pc, as determined from Gaia distance measurements of young stellar objects in the cloud (Großschedl et al. 2018). This inclination suggests that overall the radial velocities of the cloud and stars are correlated with their distance. We suggest that the presence of multiple, separated CO velocity components over much of the L 1641-S survey field is due to the cloud actually being composed of a chain of sub-clouds extending north-west to south-east and through the plane of the sky, rather than being one long, contiguous filamentary cloud.

5. Summary and future work

We present extensive mapping observations in the ^{12}CO(3-2) line of the Orion A and B GMCs. The survey covers a total area of ~2.7 square degrees, with an angular resolution of ~19″ (~7500 AU, ~0.04 pc), and a sensitivity of 0.7–0.8 K (at a velocity resolution of 0.25 km/s). The survey covers the major star formation sites in the Orion B GMC (L 1622, NGC 2068 and NGC 2071, the Ori B9 area, and NGC 2023 and NGC 2024, including the Horsehead Nebula) and a ~1.1 square degree area in the southern part of the L 1641 cloud in Orion A, complementing existing (at the time of proposal writing) JCMT HARP observations.

In the present paper, we give an overview of the survey regions and discuss the overall velocity fields of the CO emission (using moment maps of the line emission and position-velocity cuts). We find that the velocity fields in L 1622, Ori B9, and L 1641-S are characterized by narrow lines (of the order of

2–3 km/s; 'quiet' regions), while the more 'active' regions in NGC 2023, NGC 2024, NGC 2068, and NGC 2071 (which are all associated with optical reflection nebulae, H ɪɪ regions, and large embedded clusters) show larger line-widths (~4 km/s). In several regions, we see multiple velocity components (L 1622, Ori B9, NGC 2024) indicating the presence of more than one cloud or cloud component along the line of sight. In L 1641-S, in particular, we see up to three distinct velocity components. Together with previous measurements showing that there is a gradient in the distance to the cloud (more distant when going further south-east, Großschedl et al. 2018) along with a gradient in the radial velocities of the associated stars (Hacar et al. 2016), we interpret this finding as an indication that the southern L 1641-S cloud consists of a sequence of clouds along the line of sight rather than a contiguous filament.

In the more 'active' regions, we see several instances of lines splitting up into two components, coinciding with regions of optical nebulosities (most prominently in the NGC 2024 H ɪɪ region). We interpret this behaviour as being due to expanding bubbles driven by early-type stars into the molecular clouds. In particular, we rediscuss the structure of the molecular gas surrounding the NGC 2024 H ɪɪ region, concluding that, contrary to previous work, the bulk of that cloud's material (particularly in the northern part of the H ɪɪ region) lies in the foreground.

We identify a trend for CO emission to be slightly more redshifted and have narrower lines in regions that are directly exposed to incident irradiation, for example in the PDRs at the west-facing edges of NGC 2023 and NGC 2024 (including the Horsehead Nebula) and in the NGC 2068 area. In NGC 2068, around the dense dust ridge harbouring (among others) the protostars driving the HH 24 system of outflows and the HH 26 outflow, we see a transition from narrow (west) to broad (east) lines right at the location of the dense ridge, which stands out as having particularly strong ongoing star formation activity given the presence of an exceptionally high number of very red (hence young) protostars. Further evidence for the impact of the PDR along the western edge of the cloud in the NGC 2023/NGC2024 region is indicated by elevated brightness ratios between our CO(3-2) data and the CO(1-0) maps of Pety et al. (2017), indicative of high (> 40 K) molecular gas temperatures as constrained through exploratory RADEX radiative transfer modelling. In contrast, a fainter cloud component seen at velocities offset by a few km/s (around 4-5 km/s) from the main cloud is found to be cooler and more tenuous, indicating that it is not subject to significant UV irradiation and might be located somewhere in the fore- or background of the Orion region.

We also report the discovery of a small, round CO cloud north of NGC 2071, which is seen as a cometary cloud in optical images. The cloud apparently is not associated with any protostar or dense cloud core. It is illuminated and heated from the west, as indicated by a bright, west-facing rim seen in Spitzer images. While further observations will be needed to determine the true column density structure of the cloud, its circular appearance in CO suggests an underlying near spherical geometry in three dimensional space. The simple geometry makes it a prime target for comparisons with theoretical work on cloud structure and dynamics, particularly that under the influence of external irradiation. Due to its simple, apparently spherical geometry, we name this cloud the "Cow Nebula" globule.

One of the main scientific drivers for this project is to obtain an unbiased account of protostellar CO outflows over a significant part of a GMC, covering the full extent of the outflows to measure their entire energy and momentum content. While we defer a detailed identification and analysis of the outflow pop-

ulation to a subsequent paper, we here presented a comparison of the CO(3-2) line emission for the two most prominent proto-stellar outflows in the Orion B GMC (the NGC 2071-IR outflow and the monopolar outflow in NGC 2024). In both cases we find good agreement with previous, targeted observations. In particular we reproduce the wide velocity extent of the NGC 2071-IR outflow, including the pronounced 'bump' seen in the redshifted lobe at extremely high velocities, confirming the validity of our data reduction approach. We confirm the monopolar nature of the outflow in NGC 2024 in our wide-field maps, but revise its driving source to be the source FIR4 of Mezger et al. (1988) rather than FIR5 as thought previously. No conclusive evidence for a blue-shifted counterlobe to the well-collimated, jet-like red-shifted outflow lobe is seen, particularly in the immediate vicinity of the driving source, but we speculate that a patch of blue-shifted emission (B1) further north along the outflow axis marks the point where the blue-shifted outflow lobe punches through the foreground cloud bounding the H ɪɪ region.

The line moment maps (moment 1 and moment 2, i.e. mean CO velocity and CO line-widths) and numerous high-velocity spikes in the position-velocity cuts indicate the presence of a multitude of additional outflows in the survey fields. We will provide a full account of these outflows in a follow-up publication, including an identification of their driving sources (making use of the catalogue of protostars identified in the course of the Herschel Orion Protostar Survey HOPS), a characterization of the outflows in terms of mass, momentum, and energy and their respective flow rates. With our discussions of the structure of the NGC 2024 H ɪɪ region, the elevated CO(3-2)/CO(1-0) line ratios at the western edge of the cloud in the NGC 2023/NGC 2024 region, the multi-component structure of the cloud in the L 1641-S region, and the comparison of the ALCOHOLS CO(3-2) maps with the SOFIA [C ɪɪ] maps of the Horsehead Nebula and the IC 434 ionization front by Bally et al. (2018) (see also Pabst et al. 2017) we only scratch the surface of the potential applications of our wide-field CO(3-2) survey and future, even larger, wide-band molecular line surveys.

References

Allen, L. E. & Davis, C. J. 2008, Low Mass Star Formation in the Lynds 1641 Molecular Cloud, ed. B. Reipurth, Vol. 4, 621
Alves, F. O., Girart, J. M., Lai, S.-P., Rao, R., & Zhang, Q. 2011, ApJ, 726, 63
Aoyama, H., Mizuno, N., Yamamoto, H., et al. 2001, PASJ, 53, 1053
Astropy Collaboration, Price-Whelan, A. M., Sipőcz, B. M., et al. 2018, AJ, 156, 123
Astropy Collaboration, Robitaille, T. P., Tollerud, E. J., et al. 2013, A&A, 558, A33
Bally, J. 1981, in BAAS, Vol. 13, 540
Bally, J. 2008, Overview of the Orion Complex, ed. B. Reipurth, Vol. 4, 459
Bally, J., Chambers, E., Guzman, V., et al. 2018, AJ, 155, 80
Bally, J. & Lada, C. J. 1983, ApJ, 265, 824

Bally, J., Langer, W. D., Stark, A. A., & Wilson, R. W. 1987, ApJ, 312, L45
Bally, J., Walawender, J., Reipurth, B., & Megeath, S. T. 2009, AJ, 137, 3843
Barnes, P. J., Crutcher, R. M., Bieging, J. H., Storey, J. W. V., & Willner, S. P. 1989, ApJ, 342, 883
Belloche, A., Schuller, F., Parise, B., et al. 2011, A&A, 527, A145
Berné, O., Marcelino, N., & Cernicharo, J. 2014, ApJ, 795, 13
Bernes, C. 1977, A&AS, 29, 65
Bik, A., Lenorzer, A., Kaper, L., et al. 2003, A&A, 404, 249
Buckle, J. V., Curtis, E. I., Roberts, J. F., et al. 2010, MNRAS, 401, 204
Buckle, J. V., Davis, C. J., di Francesco, J., et al. 2012, MNRAS, 422, 521
Carpenter, J. M. 2000, AJ, 120, 3139
Caselli, P. & Myers, P. C. 1995, ApJ, 446, 665
Castets, A., Duvert, G., Dutrey, A., et al. 1990, A&A, 234, 469
Chandler, C. J. & Carlstrom, J. E. 1996, ApJ, 466, 338
Chernin, L. M. 1996, ApJ, 460, 711
Chernin, L. M. & Masson, C. R. 1992, ApJ, 396, L35
Chernin, L. M. & Welch, W. J. 1995, ApJ, 440, L21
Choi, M., Evans, Neal J., I., & Jaffe, D. T. 1993, ApJ, 417, 624
Choi, M., Kang, M., & Lee, J.-E. 2015, AJ, 150, 29
Curtis, E. I., Richer, J. S., & Buckle, J. V. 2010, MNRAS, 401, 455
Davis, C. J., Chrysostomou, A., Hatchell, J., et al. 2010, MNRAS, 405, 759
Dorschner, J. & Gürtler, J. 1963, Astronomische Nachrichten, 287, 257
Emprechtinger, M., Wiedner, M. C., Simon, R., et al. 2009, A&A, 496, 731
Enokiya, R., Ohama, A., Yamada, R., et al. 2021, PASJ, 73, S256
Furlan, E., Fischer, W. J., Ali, B., et al. 2016, ApJS, 224, 5
Gaume, R. A., Johnston, K. J., & Wilson, T. L. 1992, ApJ, 388, 489
Genzel, R. & Stutzki, J. 1989, ARA&A, 27, 41
Gibb, A. G. 2008, Star Formation in NGC 2068, NGC 2071, and Northern L1630, ed. B. Reipurth, Vol. 4, 693
Graf, U. U., Eckart, A., Genzel, R., et al. 1993, ApJ, 405, 249
Graves, S. F., Richer, J. S., Buckle, J. V., et al. 2010, MNRAS, 409, 1412
Großschedl, J. E., Alves, J., Meingast, S., et al. 2018, A&A, 619, A106
Güsten, R., Nyman, L. Å., Schilke, P., et al. 2006, A&A, 454, L13
Hacar, A., Alves, J., Forbrich, J., et al. 2016, A&A, 589, A80
Harju, J., Walmsley, C. M., & Wouterloot, J. G. A. 1993, A&AS, 98, 51
Ishii, S., Nakamura, F., Shimajiri, Y., et al. 2019, PASJ, 87
Ishii, S., Seta, M., Nagai, M., et al. 2016, PASJ, 68, 10
Kirk, H., Di Francesco, J., Johnstone, D., et al. 2016, ApJ, 817, 167
Klein, T., Ciechanowicz, M., Leinz, C., et al. 2014, IEEE Transactions on Tera-hertz Science and Technology, 4, 588
Kloosterman, J., Cottam, T., Swift, B., et al. 2012, in Society of Photo-Optical Instrumentation Engineers (SPIE) Conference Series, Vol. 8452, Proc. SPIE, 845204
Kloosterman, J. L. 2014, PhD thesis, The University of Arizona
Kong, S., Arce, H. G., Feddersen, J. R., et al. 2018, ApJS, 236, 25
Kounkel, M., Hartmann, L., Loinard, L., et al. 2017, ApJ, 834, 142
Kramer, C., Stutzki, J., & Winnewisser, G. 1996, A&A, 307, 915
Krügel, E., Thum, C., Pankonin, V., & Martin-Pintado, J. 1982, A&AS, 48, 345
Kun, M., Balog, Z., Mizuno, N., et al. 2008, MNRAS, 391, 84
Kutner, M. L., Tucker, K. D., Chin, G., & Thaddeus, P. 1977, ApJ, 215, 521
Lada, E. A., Bally, J., & Stark, A. A. 1991, ApJ, 368, 432
Lichten, S. M. 1982, ApJ, 253, 593
Lombardi, M., Bouy, H., Alves, J., & Lada, C. J. 2014, A&A, 566, A45
Maddalena, R. J., Morris, M., Moscowitz, J., & Thaddeus, P. 1986, ApJ, 303, 375
Magakian, T. Y. 2003, A&A, 399, 141
Margulis, M. & Snell, R. L. 1989, ApJ, 343, 779
Matthews, B. C., Fiege, J. D., & Moriarty-Schieven, G. 2002, ApJ, 569, 304
Megeath, S. T., Gutermuth, R., Muzerolle, J., et al. 2012, AJ, 144, 192
Megeath, S. T., Gutermuth, R., Muzerolle, J., et al. 2016, AJ, 151, 5
Menten, K. M., Reid, M. J., Forbrich, J., & Brunthaler, A. 2007, A&A, 474, 515
Meyer, M. R., Flaherty, K., Levine, J. L., et al. 2008, Star Formation in NGC 2023, NGC 2024, and Southern L1630, ed. B. Reipurth, Vol. 4, 662
Mezger, P. G., Chini, R., Kreysa, E., Wink, J. E., & Salter, C. J. 1988, A&A, 191, 44
Mezger, P. G., Sievers, A. W., Haslam, C. G. T., et al. 1992, A&A, 256, 631
Miettinen, O., Harju, J., Haikala, L. K., Kainulainen, J., & Johansson, L. E. B. 2009, A&A, 500, 845
Moriarty-Schieven, G. H., Snell, R. L., & Hughes, V. A. 1989, ApJ, 347, 358
Motte, F., André, P., Ward-Thompson, D., & Bontemps, S. 2001, A&A, 372, L41
Muders, D. & Hafok, H. 2019, APEX Calibration and Data Reduction Manual
Nagahama, T., Mizuno, A., Ogawa, H., & Fukui, Y. 1998, AJ, 116, 336
Nakamura, F., Ishii, S., Dobashi, K., et al. 2019, PASJ, 71, S3
Nakamura, F., Miura, T., Kitamura, Y., et al. 2012, ApJ, 746, 25
Nishimura, A., Tokuda, K., Kimura, K., et al. 2015, ApJS, 216, 18
Pabst, C. H. M., Goicoechea, J. R., Teyssier, D., et al. 2020, A&A, 639, A2
Pabst, C. H. M., Goicoechea, J. R., Teyssier, D., et al. 2017, A&A, 606, A29
Pety, J., Guzmán, V. V., Orkisz, J. H., et al. 2017, A&A, 599, A98
Pillitteri, I., Wolk, S. J., Megeath, S. T., et al. 2013, ApJ, 768, 99
Reipurth, B., Herbig, G., & Aspin, C. 2010, AJ, 139, 1668

Reipurth, B. & Madsen, C. 1989, The Messenger, 55, 32

Reipurth, B., Megeath, S. T., Bally, J., & Walawender, J. 2008, The L1617 and L1622 Cometary Clouds in Orion, ed. B. Reipurth, Vol. 4, 782

Ren, Z. & Li, D. 2016, ApJ, 824, 52

Richer, J. S., Hills, R. E., & Padman, R. 1992, MNRAS, 254, 525

Richer, J. S., Hills, R. E., Padman, R., & Russell, A. P. G. 1989, MNRAS, 241, 231

Ripple, F., Heyer, M. H., Gutermuth, R., Snell, R. L., & Brunt, C. M. 2013, MNRAS, 431, 1296

Sakamoto, S., Hasegawa, T., Hayashi, M., Morino, J.-I., & Sato, K. 1997, ApJ, 481, 302

Sakamoto, S., Hayashi, M., Hasegawa, T., Handa, T., & Oka, T. 1994, ApJ, 425, 641

Sandell, G., Avery, L. W., Baas, F., et al. 1999, ApJ, 519, 236

Sandell, G., Mookerjea, B., Güsten, R., et al. 2015, A&A, 578, A41

Sanders, D. B. & Willner, S. P. 1985, ApJ, 293, L39

Shimajiri, Y., Kawabe, R., Takakuwa, S., et al. 2011, PASJ, 63, 105

Siringo, G., Kreysa, E., Kovács, A., et al. 2009, A&A, 497, 945

Snell, R. L., Scoville, N. Z., Sanders, D. B., & Erickson, N. R. 1984, ApJ, 284, 176

Strom, K. M., Strom, S. E., & Merrill, K. M. 1993, ApJ, 412, 233

Stutz, A. M. 2018, MNRAS, 473, 4890

Stutz, A. M. & Gould, A. 2016, A&A, 590, A2

Stutz, A. M. & Kainulainen, J. 2015, A&A, 577, L6

Stutz, A. M., Tobin, J. J., Stanke, T., et al. 2013, ApJ, 767, 36

Subrahmanyan, R., Goss, W. M., Megeath, S. T., & Barnes, P. J. 1997, MNRAS, 290, 431

Takahashi, S., Saito, M., Ohashi, N., et al. 2008, ApJ, 688, 344

Ulich, B. L. & Haas, R. W. 1976, ApJS, 30, 247

van der Tak, F. F. S., Black, J. H., Schöier, F. L., Jansen, D. J., & van Dishoeck, E. F. 2007, A&A, 468, 627

Walther, D. M. & Geballe, T. R. 2019, ApJ, 875, 153

Ward-Thompson, D., Di Francesco, J., Hatchell, J., et al. 2007, PASP, 119, 855

Watanabe, T. & Mitchell, G. F. 2008, AJ, 136, 1947

Weiland, J. L., Odegard, N., Hill, R. S., et al. 2011, ApJS, 192, 19

White, G. J., Drabek-Maunder, E., Rosolowsky, E., et al. 2015, MNRAS, 447, 1996

Wilson, B. A., Dame, T. M., Masheder, M. R. W., & Thaddeus, P. 2005, A&A, 430, 523

Wilson, R. W., Jefferts, K. B., & Penzias, A. A. 1970, ApJ, 161, L43

Zhang, C.-P., Li, G.-X., Zhou, C., Yuan, L., & Zhu, M. 2019, A&A, 631, A110

Zucker, C., Speagle, J. S., Schlafly, E. F., et al. 2019, ApJ, 879, 125

[1] ESO, Karl-Schwarzschild-Straße 2, 85748 Garching bei München
e-mail: tstanke049@gmail.com

[2] Department of Astronomy, Yale University, P.O. Box 208101, New Haven, CT 06520-8101, USA

[3] CASA, University of Colorado, Boulder, CO, USA

[4] Dept of Space, Earth and Environment, Chalmers Univ. of Technology, Onsala Space Observatory, 43992 Onsala, Sweden

[5] Joint ALMA Observatory, Avenida Alonso de Córdova 3107, Vitacura, Santiago, Chile

[6] National Science Foundation, 2415 Eisenhower Avenue, Alexandria, VA 22314, USA

[7] NRC Herzberg Astronomy and Astrophysics, 5071 West Saanich Road, Victoria, BC, V9E 2E7, Canada

[8] Thüringer Landessternwarte, Sternwarte 5, D-07778 Tautenburg, Germany

[9] School of Physical Sciences, University of Kent, Canterbury CT2 7NH, UK

[10] Department of Astronomy, University of Florida, PO Box 112055, USA

[11] Department of Astronomy, University of Massachusetts, Amherst, MA, 01003, USA
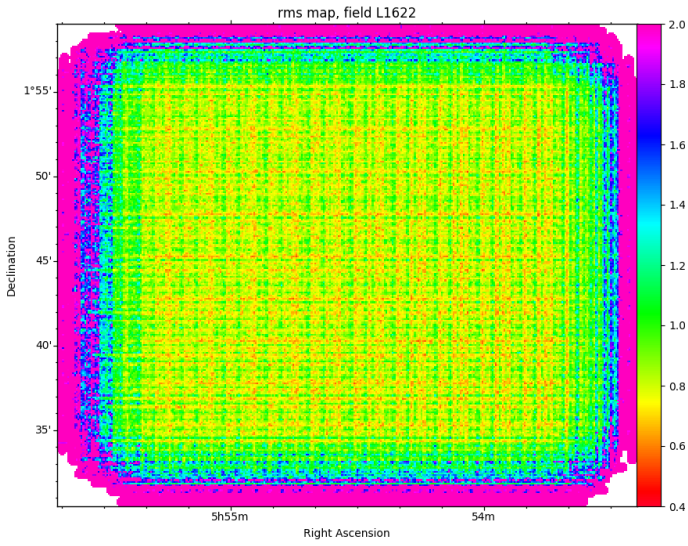
[12] Department of Physics and Astronomy, University of Victoria, Victoria, BC, V8P 5C2, Canada

[13] Departamento de Astronomía, Universidad de Chile, Casilla 36-D, Santiago, Chile
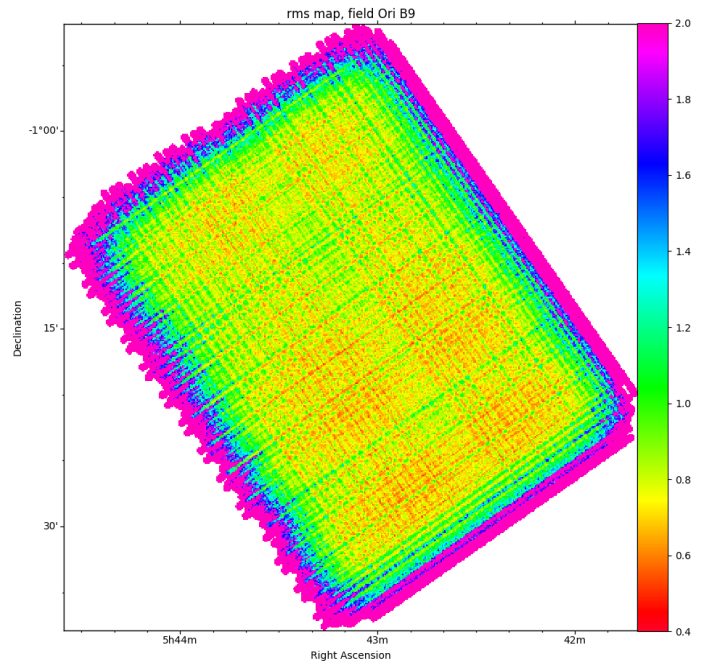
[14] European Space Agency, ESTEC, Postbus 299, 2200 AG Noordwijk, The Netherlands

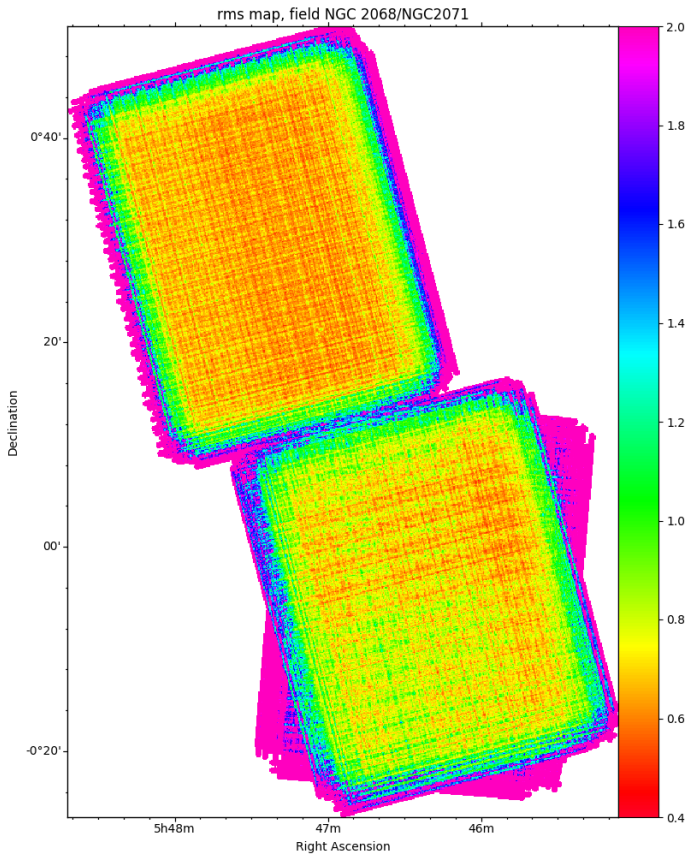[15] Department of Physics and Astronomy, University of Toledo, Toledo, OH 43606, USA

[16] National Astronomical Observatory, 2-21-1 Osawa, Mitaka, Tokyo 181-8588, Japan

[17] Centre for Astrophysics and Planetary Science, School of Physical Sciences, University of Kent, Canterbury CT2 7NH, UK

[18] Departmento de Astronomía, Facultad de Ciencias Físicas y Matemáticas, Universidad de Concepción, Concepción, Chile

[19] Nobeyama Radio Observatory, National Astronomical Observatory of Japan, National Institutes of Natural Sciences, 462-2 Nobeyama, Minamimaki, Minamisaku, Nagano 384-1305, Japan
e-mail: k.tatematsu@nao.ac.jp

[20] Steward Observatory, University of Arizona, 933 N. Cherry Avenue, Tucson AZ 85721

[21] Institute for Astronomy, University of Hawaii at Manoa, Honolulu, HI 96822, USA
e-mail: jw@hawaii.edu

[22] Universidad Autonoma de Chile, Pedro de Valdivia 425, Santiago de Chile

[23] University of Southern Indiana, Evansville, IN, USA

[24] Jet Propulsion Laboratory, California Institute of Technology, 4800 Oak Grove Drive, Pasadena, CA 91109-8099, USA

[25] European Southern Observatory, Alonso de Córdova 3107, Vitacura, Casilla, 19001, Santiago de Chile, Chile

Fig. A.1. Noise map for the L1622 field.

Fig. A.2. Noise map for the NGC 2068 and NGC 2071 field.


Fig. A.3. Noise map for the Ori B9 field.
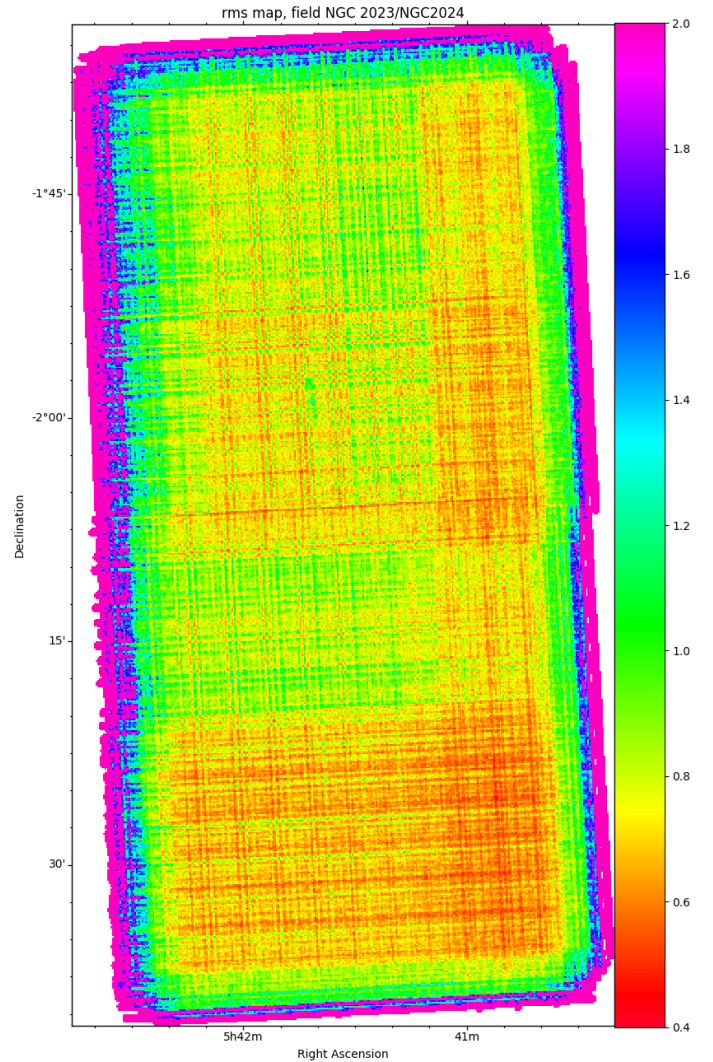
Fig. A.4. Noise map for the NGC 2023 and NGC 2024 field.

Appendix A: Noise maps and additional rms statistics

We here present noise maps for the five survey fields (Figs. A.3 to A.5). The rms for each spatial pixel is measured directly in the cube, deriving statistics for the spectrum over the velocity range beyond the maximum velocity extent of CO emission. The colour mapping is the same for all fields to allow for a comparison between them and an easy assessment of the (non)uniformity of the rms within each.
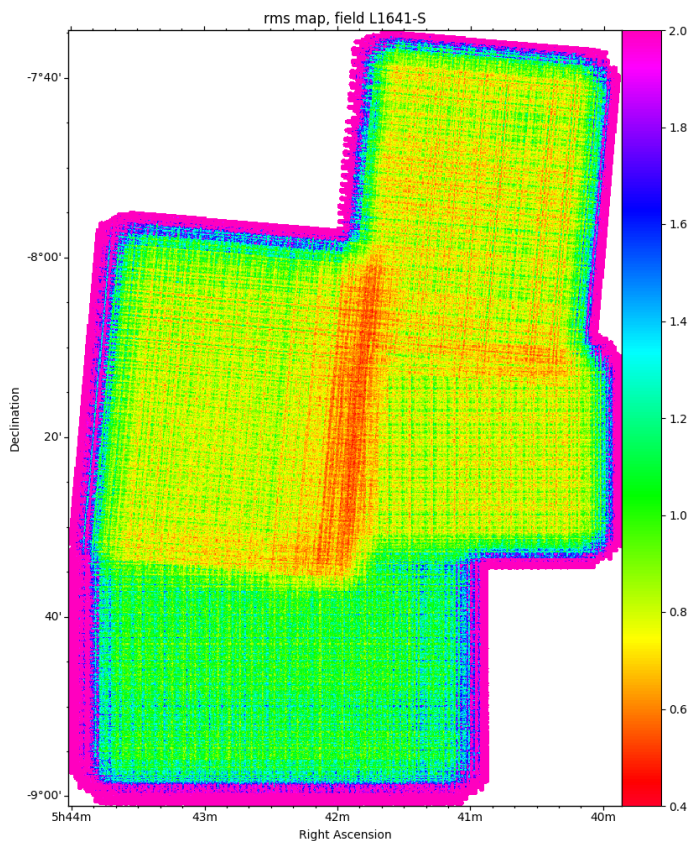
Fig. A.5. Noise map for the L1641-S field.

We also show the full frequency distribution of brightness values in the cubes in Fig. A.6. To characterize the noise in the cubes further, we have approximated the frequency distributions by Gaussians, varying the fitting ranges to check at which extent the non-Gaussian wings of the distributions (stemming from noisier sections at the cube edges, where the exposure time per spatial pixel is lower, and from source emission) influences the noise estimate. We provide the derived rms values for various fitting ranges around the maximum of the distribution (± 1 K: green; ± 2 K: yellow; ± 4 K: red; full intensity range: black) in Fig. A.6, along with the fits plotted over the histograms. We also plot the normalized residuals after subtraction of the Gaussian fits.

As expected, increasing the fitting range results in broader Gaussian fits, as the contribution of the noisy spatial pixels at the map edges and astronomical signal contribute increasingly to the wider range of brightness values. The residuals indicate that overall a Gaussian is not a very good representation of the brightness distribution, which can be understood as the overall distribution is the sum over the distributions of the individual spatial pixels, each of which should be a Gaussian (in the emission-free parts of the spectrum) with its own standard deviation. Adding Gaussians with differing standard deviations will result in an overall distribution that is more triangular than a Gaussian. In particular, a Gaussian fit will underestimate the values in the very centre of the distribution. Using a narrow fitting range reduces the residual in the centre, but implies larger residuals in the wings of the distributions. Larger fitting ranges somewhat reduce the residuals in the wings, but also produce larger residuals on the central peak.

The derived standard deviations are systematically larger than the typical rms values derived in Sect. 3.2. This can be at-

tributed to the significant contribution of the noisy spatial pixels at the map edges (and the inclusion of the full spectral range, while in Sect. 3.2 we excluded the spectral range with bright line emission. To illustrate this further, Fig. A.7 shows the frequency distributions of brightness values in the LDN 1622 survey field over the full cube (left) and of the central part excluding the noisy spatial pixels at the map edges (right). Excluding the map edges results in a more Gaussian shape of the distribution (the residuals are significantly reduced, the width of the fitting range has a much smaller impact on the resulting standard deviations of the fits). Moreover, the derived rms of 0.82 K agrees well with the typical rms derived in Sect. 3.2 of 0.81 K, indicating that our approach for deriving typical rms values for the well-observed central parts of the maps gives sensible values.

Appendix B: Line velocities

We here give an overview of the CO line properties within the survey fields. For each field, we show a RGB coded map of the red-shifted/central/blue-shifted velocity range of the main part of the line (i.e. excluding high velocity line-wings). We furthermore show maps of the first three line moments, computed using the GILDAS MOMENTS task: moment 0: integrated intensity, moment 1: mean velocity, and moment 2: line width, where we limit the calculation to emission brighter than 3.5 K (while the integrated maps presented in Figs. 7, 10, 16, 18, and 31 add up individual velocity channels regardless of line detection and brightness) and to a certain velocity range, which varies from field to field. For the L 1622 field we only include the main cloud component around 1 km/s. For the Ori B9, field we show RGB and moment maps for both velocity components (around 3 km/s and around 10 km/s).

Appendix C: CO(3-2)/CO(1-0) RADEX models

Here, we explore the use of the CO(3-2) and CO(1-0) line intensities and intensity ratios to constrain the physical conditions in the emitting gas, using the RADEX line radiative transfer code (van der Tak et al. 2007). We calculated grids of line main beam brightnesses and their ratios, covering a temperature range from 10 K to 200 K and H_2 densities ranging from $n = 10^2$ cm^{-3} to 10^6 cm^{-3}, and for CO column densities ranging from $N = 10^{15}$ cm^{-2} to 10^{19} cm^{-2}. In Fig. C.1 we plot RADEX CO(3-2)/CO(1-0) line ratios, restricted to models reproducing three diverse emission regimes, as follows:

The multi-colour scale in Fig. C.1 corresponds to models resulting in 'typical' line brightnesses and line ratios as judged from Fig. 24. As 'typical' we take CO(1-0) brightness values between 15 K and 23 K (corresponding to 45 K km/s to 70 K km/s integrated over 3 km/s), CO(3-2) between 8 K and 16 K (24 K km/s to 48 K km/s integrated over 3 km/s), and ratios between 0.5 and 0.75. We find that there are valid models for column densities ranging from 10^{17} cm^{-2} to 10^{19} cm^{-2} (the multi-colour scale models in Fig. C.1 are for an intermediate column density of $N = 10^{18}$ cm^{-2}). Depending on the CO column density a large range of parameters can reproduce the observed emission. Low column densities require moderately high temperatures (20 K-40 K) to reach the measured brightness values, along with high densities. At higher column densities, temperatures of a 10 K to ~25 K are sufficient along with lower densities (few $\times 10^3$ cm^{-3}).

The red colour scale in Fig. C.1 marks conditions that might yield the line ratios that characterize the faint
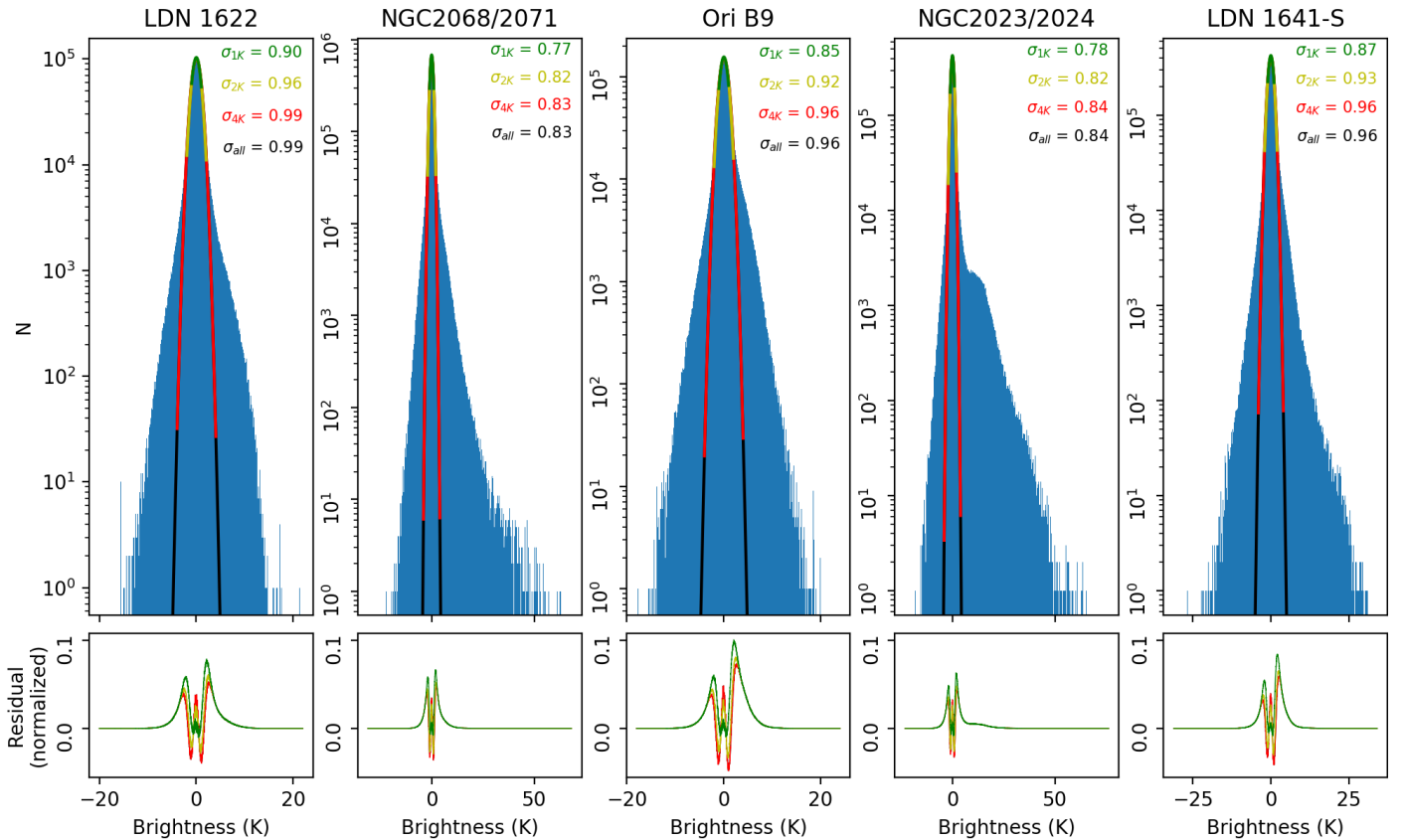
Fig. A.6. Histograms of the brightness values for the five survey fields, along with the results of Gaussian fits to the central peak of the distribution (green: fitting range 0 ± 1 K; yellow: fitting range 0 ± 2 K; red: fitting range 0 ± 4 K; black: fitting range entire brightness range). The top row shows the histograms, while the bottom row show the residuals of the Gaussian fits (normalized to the maximum pixel count).

cloud component seen at velocities around 4-5 km/s towards NGC 2023/NGC 2024. While we do not have a map of the CO(1-0) emission for this component available, the comparison of the integrated spectra (Fig. 21) indicates that the CO(3-2)/CO(1-0) ratio is ~ 2 times smaller than for the 'typical' cloud emission, we thus plot only models that result in line ratios between 0.25 and 0.4; further we only show models with CO(3-2) brightness less than 10 K (the maximum we see in our cubes for that velocity component). Again a wide range of parameters can reproduce the observed emission, with column densities being lower by a factor of a few than for the 'typical' molecular gas. Valid models are obtained for column densities ranging from 2×10^{16} cm^{-2} to 5×10^{18} cm^{-2} (where the red colour scale indicates models with an intermediate column density of $N = 2 \times 10^{17}$ cm^{-2}). Lower column densities generally result in a shift to higher temperatures, while there is a degeneracy between temperature and density (higher temperatures need lower densities to keep the CO(3-2)/(1-0) line ratio low through subthermal excitation at low densities).

Finally, the blue colour scale in Fig. C.1 shows models reproducing the high line ratios and comparably low intensities found along the western edge of the clouds interfacing molecular gas and the IC 434 ionization front. We only show models that result in CO(3-2) brightness between 2 K and 13 K (6 K km/s to ~ 40 K km/s integrated over 3 km/s), CO(1-0) brightness between 0 K and 10 K (0 K km/s to ~ 30 K km/s integrated over 3 km/s), and line ratios between 0.9 and 1.8. Valid models are found for column densities between 5×10^{15} cm^{-2} and 5×10^{16} cm^{-2} (where the blue scale in Fig. C.1 shows models with an intermediate column density of $N = 10^{16}$ cm^{-2}). Compared to the 'typical'

molecular gas discussed above, significantly lower CO column densities along with a higher temperatures gas temperature are required to reproduce the line emission in this high-excitation component, as could be expected from gas being exposed to and heated by intense UV irradiation.

Appendix D: APEX/Laboca 870 μm dust continuum maps

We here include 870 μm dust continuum maps, taken with the Laboca bolometer array (Siringo et al. 2009) on APEX. The main purpose of the observations was to provide sub-millimetre photometry of the protostars observed in the course of the Herschel Orion Protostar Survey (HOPS) and so determine the amount of circumstellar material left for further accretion in the envelope and disk (Stutz et al. 2013; Furlan et al. 2016). The maps are used at several instances in the present paper to demonstrate the relation between dense gas and the bulk cloud emission as traced by the CO emission.

The observing strategy was optimized to cover efficiently the sample of Spitzer identified protostars observed with Herschel in the HOPS project. This goal was achieved by implementing a number of well placed spiral raster maps (each covering a roughly circular patch with a diameter of the order of 15′). To these maps, we added linear On-The-Fly scans to achieve more complete areal coverage and better sensitivity to larger scale emission. We emphasize that the noise is not uniform over the maps as a consequence of this observing strategy. In the Ori B9 field, we also extracted the data obtained by Miettinen et al.
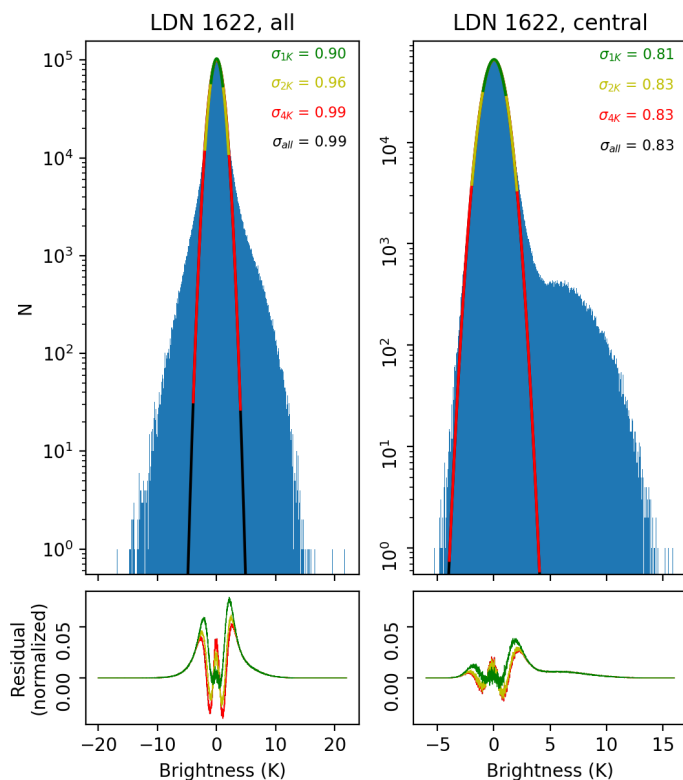
Fig. A.7. Histograms of the brightness values for the LDN 1622 survey field, along with the results of Gaussian fits to the central peak of the distribution (green: fitting range 0 ± 1 K; yellow: fitting range 0 ± 2 K; red: fitting range 0 ± 4 K; black: fitting range entire brightness range). The top row shows the histograms, while the bottom row show the residuals of the Gaussian fits (normalized to the maximum pixel count). Left: distribution for the full field. Right: distribution for the central part of the field, excluding the noisy map edges.

iterations result in increasingly better recovery of extended emission, while the later iterations give increasingly better noise removal, while preserving the extended emission components. In the end we use 35 iterations for our final maps (as compared to 21 iterations in Belloche et al. 2011).

(2009) from the archive and included them in the reduction and analysis.

Data calibration and reduction followed standard methods as outlined in Siringo et al. (2009), with an iterative procedure designed to filter out rapid atmospheric brightness variations (sky-noise) while retaining as much as possible of the extended astronomical emission, similar to the method outlined by Belloche et al. (2011). The iterative procedure uses the resulting map of the previous iteration as input for a sky-brightness model. This model emission is subtracted from the bolometer time-stream data before the sky-noise filtering, allowing for more stringent sky-noise filtering in later iterations, as the sky-brightness model gets increasingly better. The sky-brightness model uses the resulting map of the previous iteration and assumes that negative emission is an artefact due to filtering of extended emission components. This behaviour is accounted for by replacing negative values in the map, below a certain threshold, by 'zero' values. For our reduction we used a slightly different approach than Belloche et al. (2011) to construct the sky emission model for each iteration, smoothing the map from the previous iteration to a larger beam before replacing negative values (below a certain threshold) by 'zero' values (and excluding areas with higher rms, mostly at map edges, from replacing negative values, to avoid injecting too much 'artificial' flux in these areas). The amount of smoothing was gradually reduced in later iterations, while at the same time the radius over which correlated emission variations (sky-noise) is determined was reduced (allowing for an increasingly more efficient removal of sky-noise). Overall, the earlier
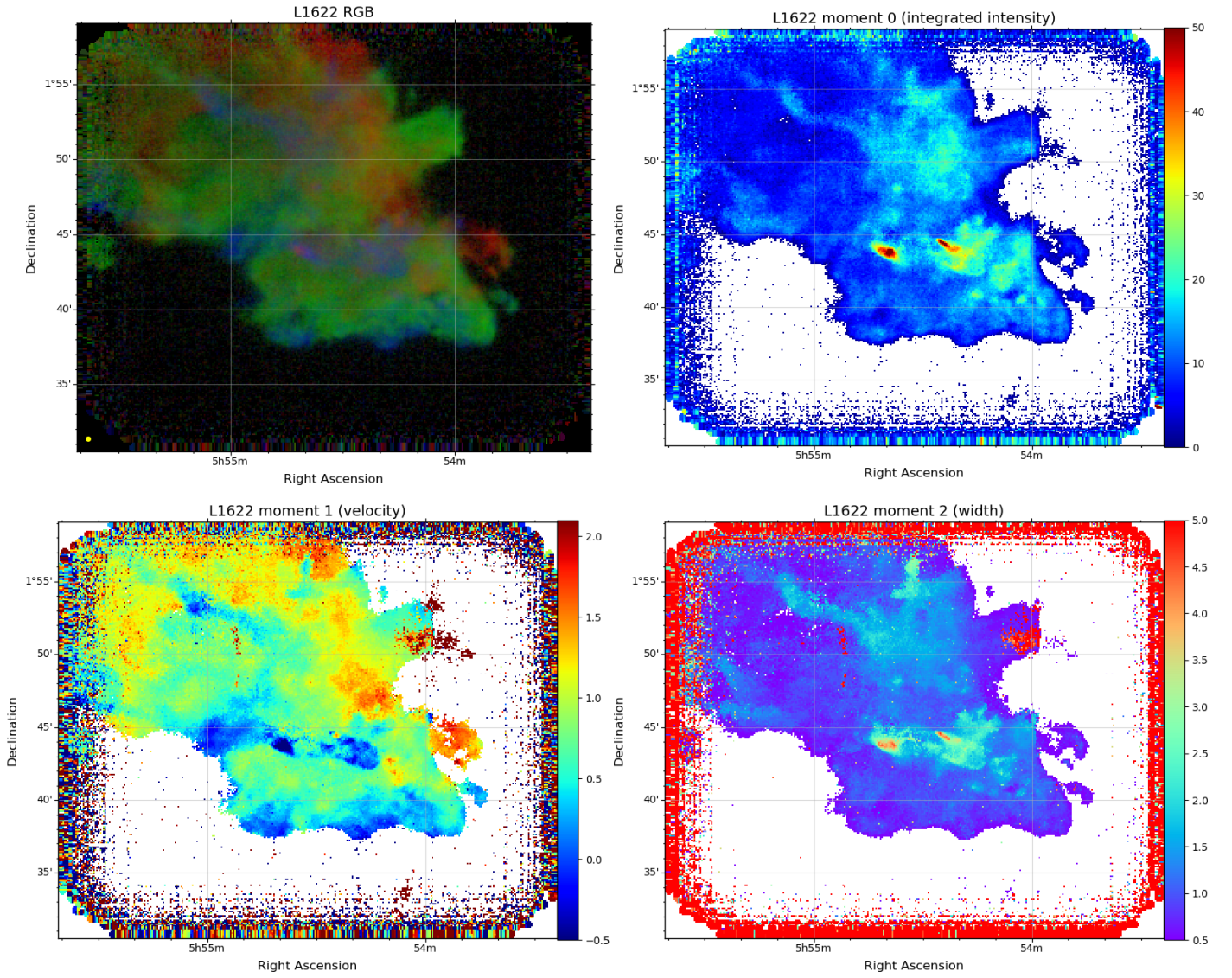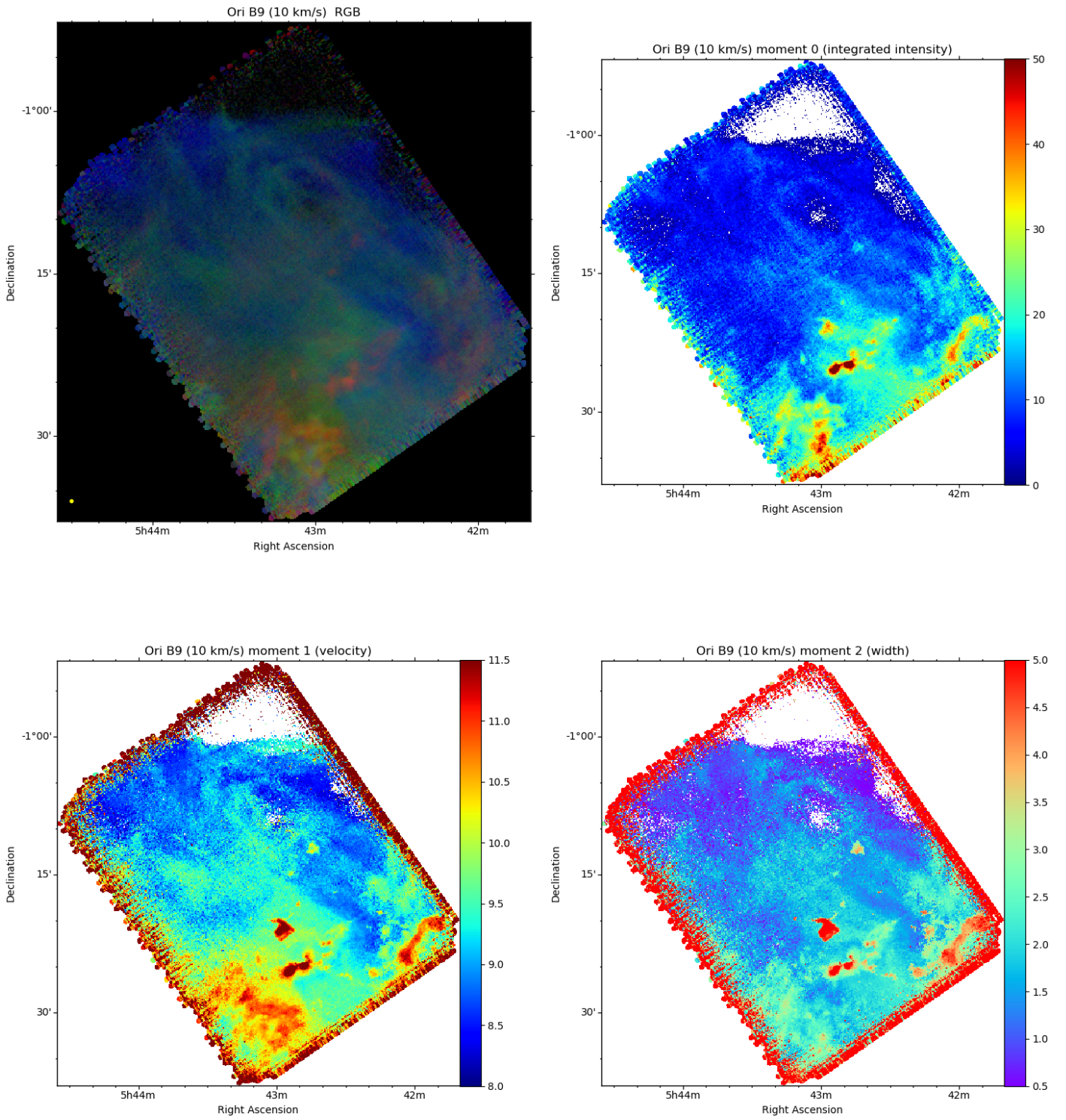
Fig. B.1. Properties of the velocity field in the L 1622 area. Top, left panel: red/green/blue representation of the velocity field around the clouds ambient velocity; red: $v = +1.25$ km/s to $+2.25$ km/s; green: $v = +0.25$ km/s to $+1.0$ km/s; blue: $v = -1.0$ km/s to 0.0 km/s. The yellow dot in the lower left corner indicates the beam size. The remaining three panels show maps of the first three moments of the line emission, computed over the velocity range from -6 km/s to $+8$ km/s, and limited to emission brighter than 3.5 K.
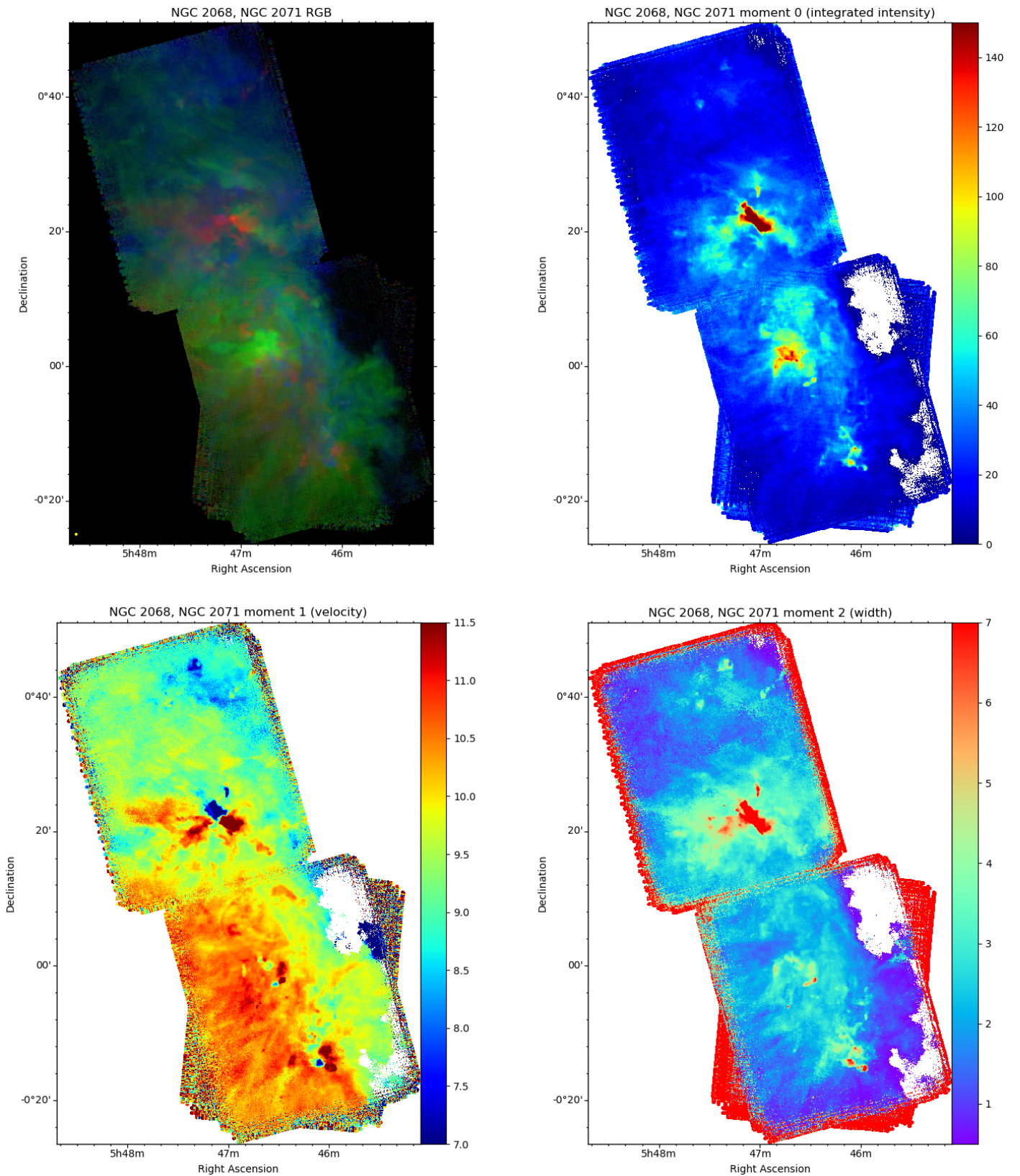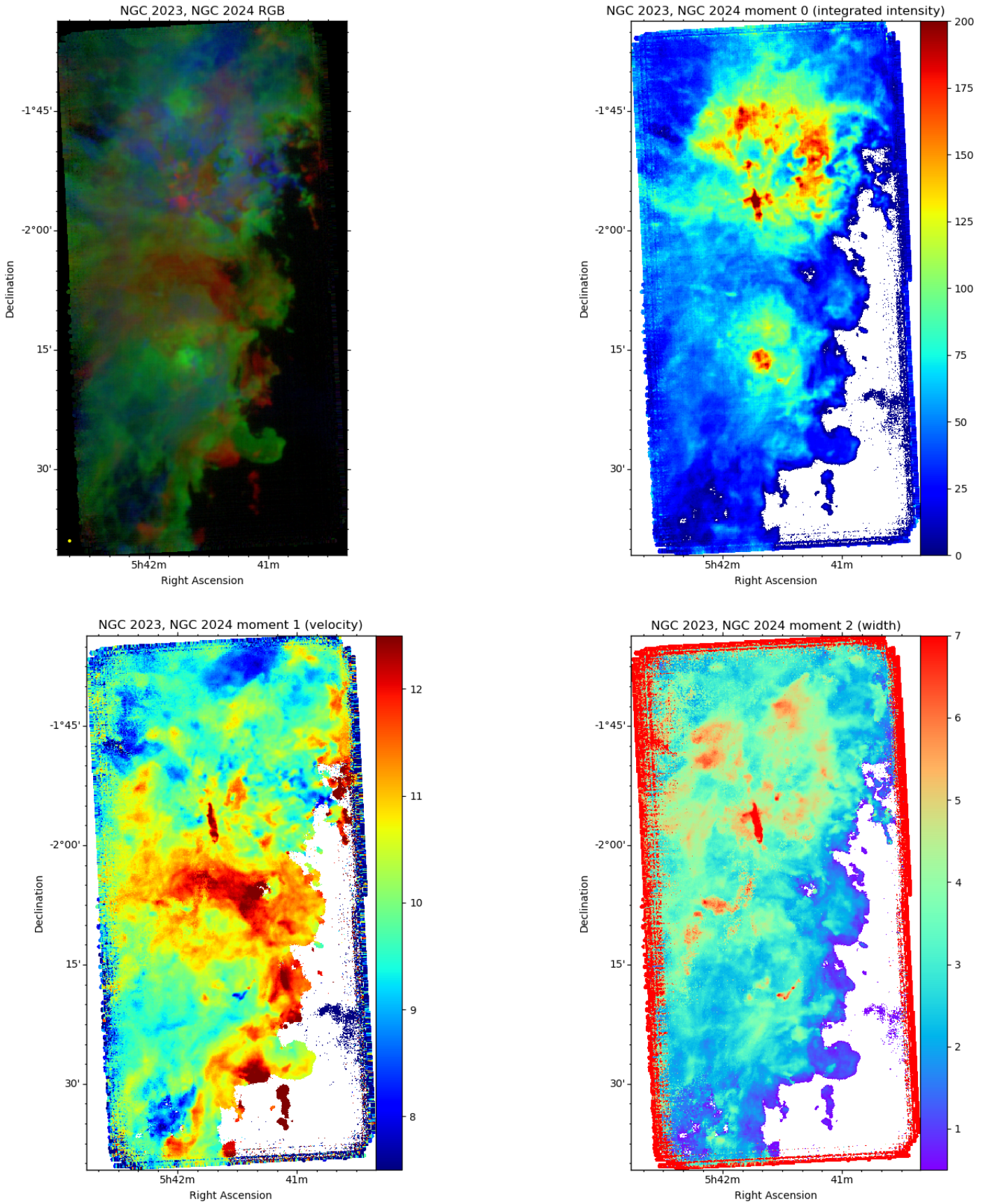
Fig. B.2. Properties of the velocity field in the NGC 2068 and NGC 2071 area. Top, left panel: red/green/blue representation of the velocity field around the clouds ambient velocity; red: $v = +11.25$ km/s to $+13.0$ km/s; green: $v = +9.5$ km/s to $+11.0$ km/s; blue: $v = +7.5$ km/s to $+9.25$ km/s. The yellow dot in the lower left corner indicates the beam size. The remaining three panels show maps of the first three moments of the line emission, computed over the velocity range from 0 km/s to $+20$ km/s, and limited to emission brighter than 3.5 K.
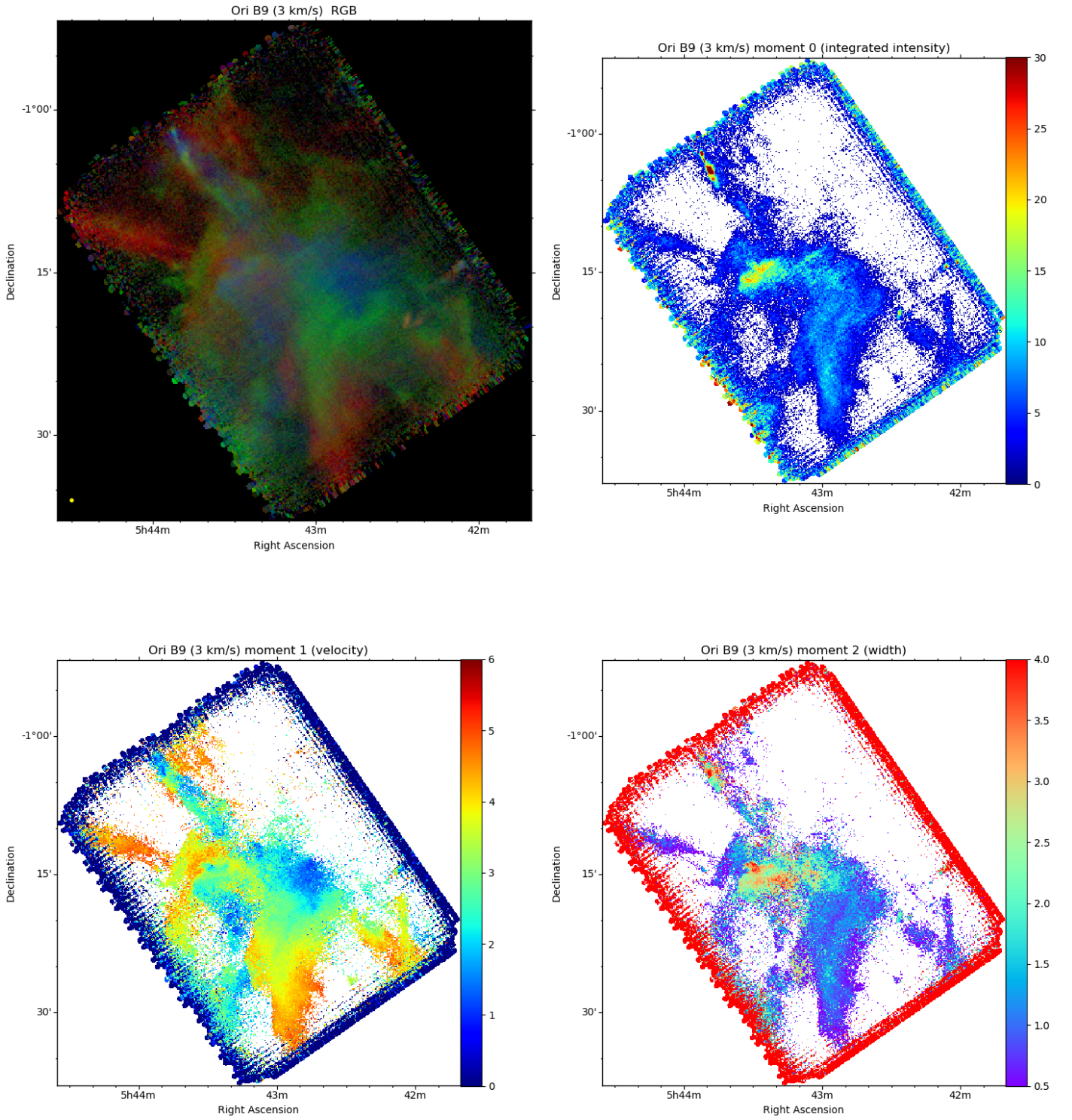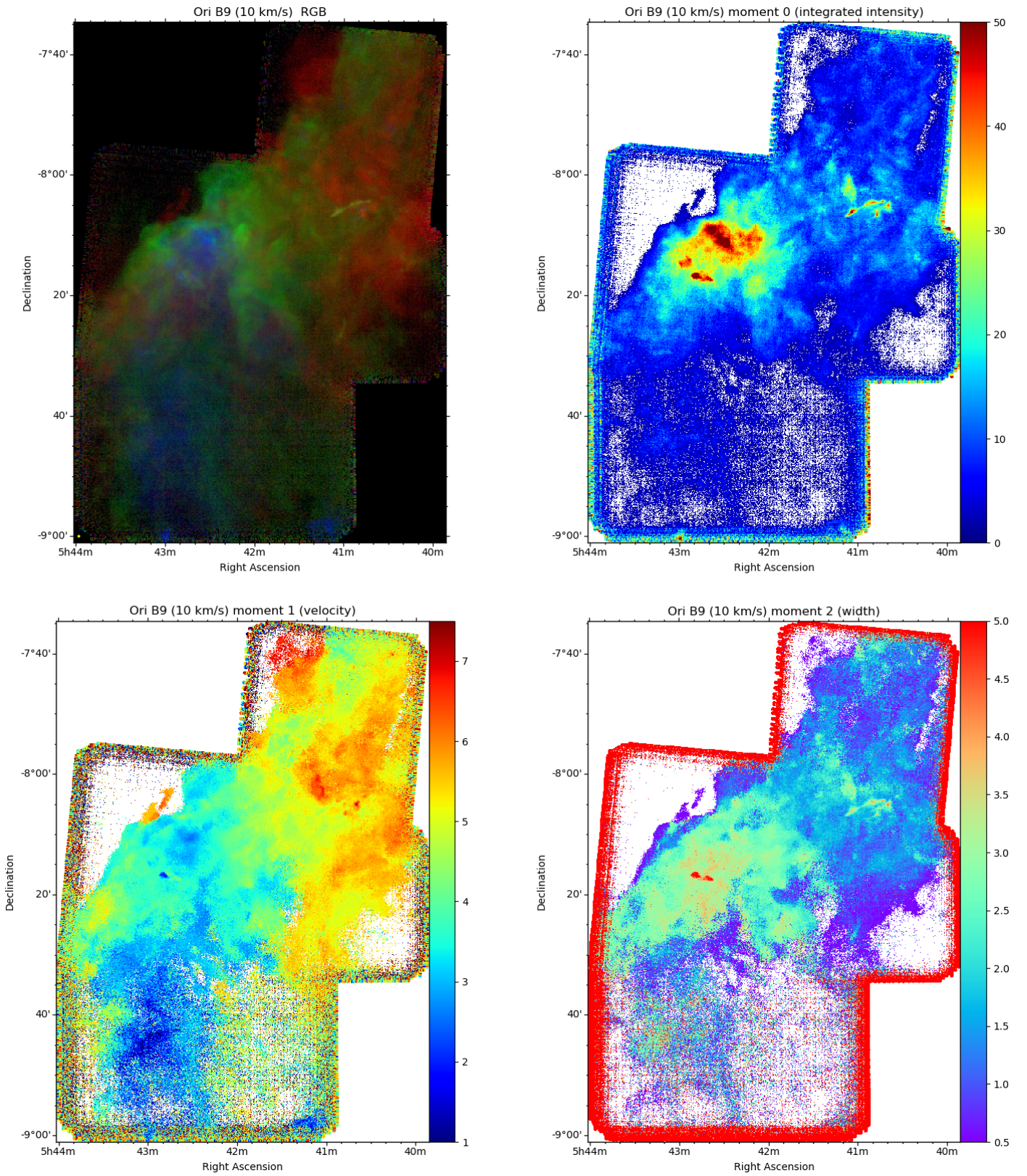
Fig. B.3. Properties of the velocity field in the Ori B9 area, for velocities around +3 km/s. Top, left panel: red/green/blue representation of the velocity field around the central velocity of +3 km/s; red: v = +4.0 km/s to +5.5 km/s; green: v = +2.25 km/s to +3.75 km/s; blue: v = +0.5 km/s to +2.0 km/s. The yellow dot in the lower left corner indicates the beam size. The remaining three panels show maps of the first three moments of the line emission, computed over the velocity range from −6 km/s to +8 km/s, and limited to emission brighter than 3.5 K.
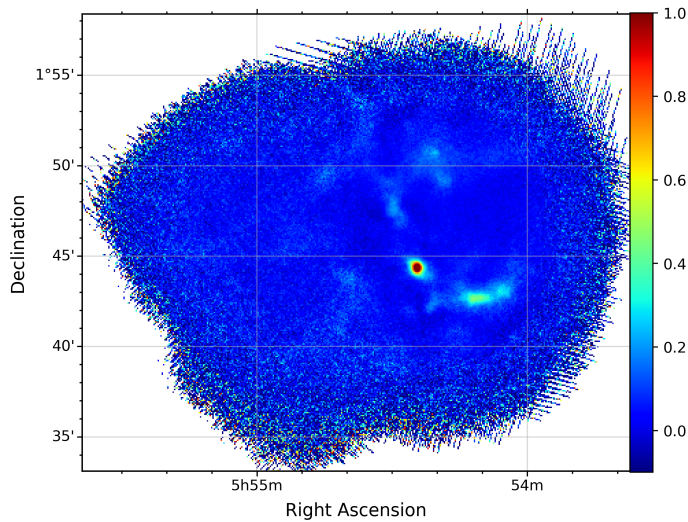
Fig. B.4. Properties of the velocity field in the Ori B9 area, for velocities around +10 km/s. Top, left panel: red/green/blue representation of the velocity field around the central velocity of +10 km/s; red: $v = +10.75$ km/s to $+12.0$ km/s; green: $v = +9.5$ km/s to $+10.5$ km/s; blue: $v = +8.0$ km/s to $+9.25$ km/s. The yellow dot in the lower left corner indicates the beam size. The remaining three panels show maps of the first three moments of the line emission, computed over the velocity range from +8 km/s to +20 km/s, and limited to emission brighter than 3.5 K.

Fig. B.5. Properties of the velocity field in the NGC 2023 and NGC 2024 area. Top, left panel: red/green/blue representation of the velocity field around the clouds ambient velocity; red: $v = +11.5$ km/s to $+14.0$ km/s; green: $v = +9.25$ km/s to $+11.25$ km/s; blue: $v = +6.5$ km/s to $+9.0$ km/s. The yellow dot in the lower left corner indicates the beam size. The remaining three panels show maps of the first three moments of the line emission, computed over the velocity range from -5 km/s to $+20$ km/s, and limited to emission brighter than 3.5 K.
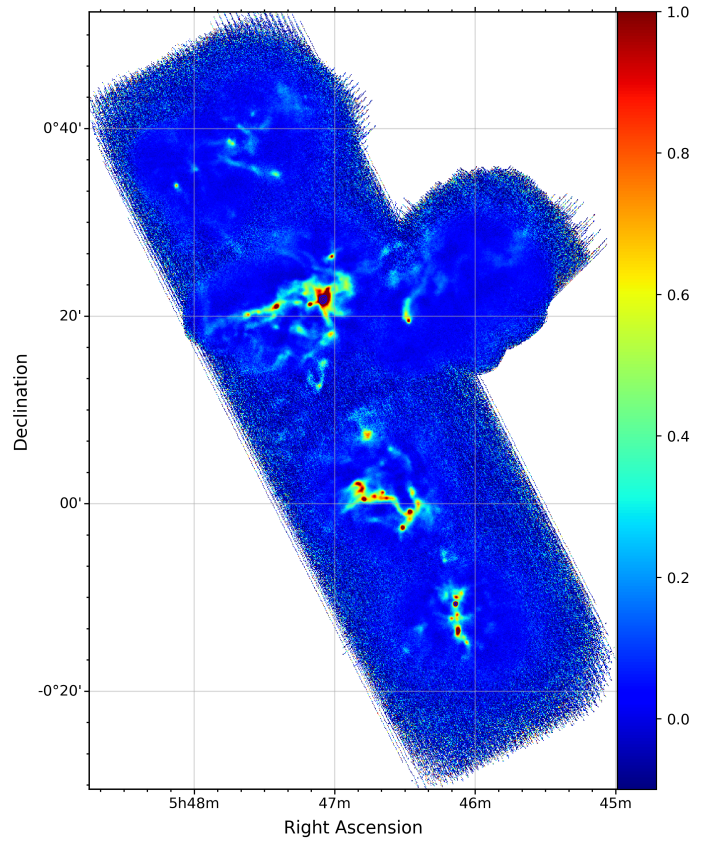
Fig. B.6. Properties of the velocity field in the L 1641-S area. Top, left panel: red/green/blue representation of the velocity field around the clouds ambient velocity; red: v = +5.0 km/s to +7.25 km/s; green: v = +3.0 km/s to +4.75 km/s; blue: v = +0.5 km/s to +2.75 km/s. The yellow dot in the lower left corner indicates the beam size. The remaining three panels show maps of the first three moments of the line emission, computed over the velocity range from −5 km/s to +15 km/s, and limited to emission brighter than 3.5 K.
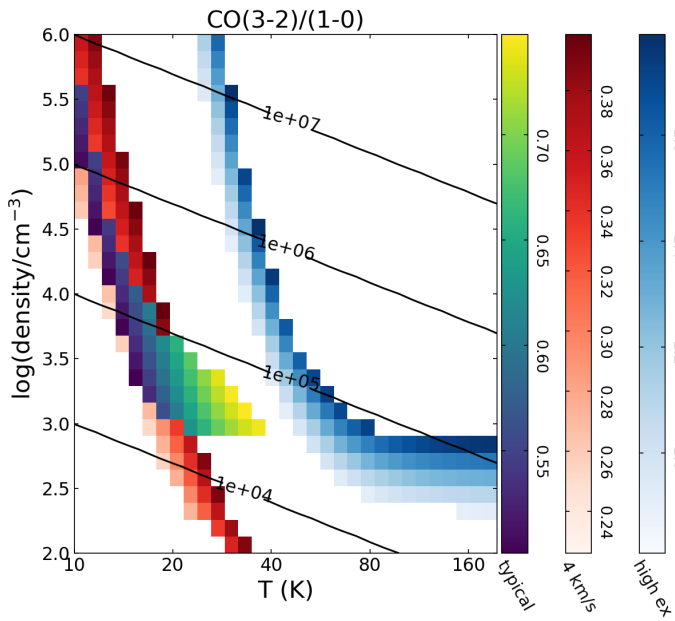
Fig. C.1. Parameter space of RADEX models reproducing the line intensities and line ratios found in the NGC 2023 and NGC 2024 region, for three diverse emission components. Line ratios of models reproducing the 'typical' emission are shown on a multi-colour scale, models corresponding to the emission component seen at ~4 km/s are shown on a red colour scale, and models reproducing the high-excitation component at the western cloud edge are shown on a blue colour scale. For each component, models for a column density in the (logarithmic) middle of the column density range reproducing the respective characteristic line ratios and intensities are shown: $N = 10^{18}$ cm^{-2} (typical emission), $N = 2 \cdot 10^{17}$ cm^{-2} (4 km/s component), and $N = 10^{16}$ cm^{-2} (high-excitation component). Straight lines mark locations of constant pressure $p = n \cdot T$. Top: RADEX models for the 'typical' emission.
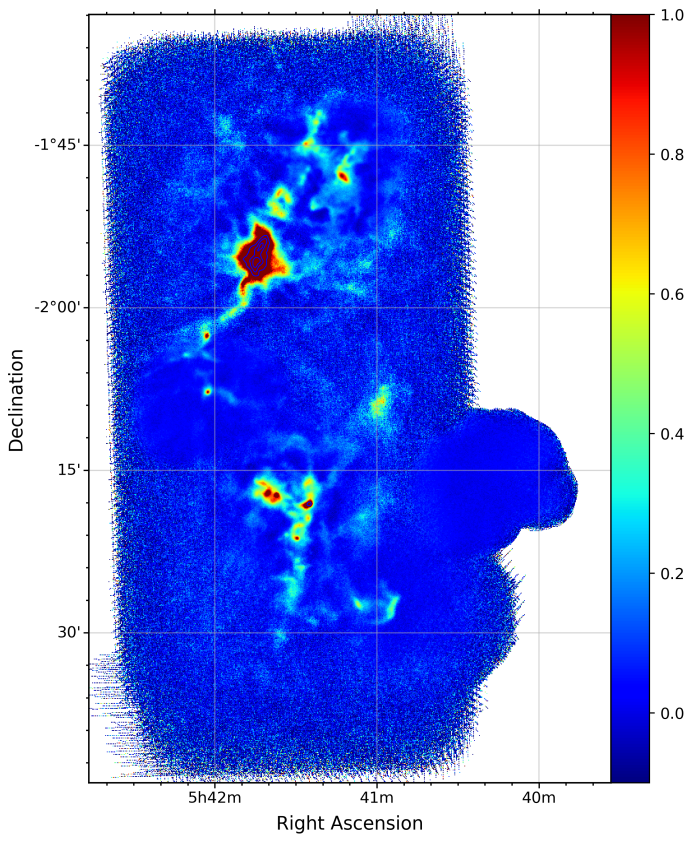

Fig. D.2. As Fig. D.1, but for the NGC 2068/NGC 2071 field.
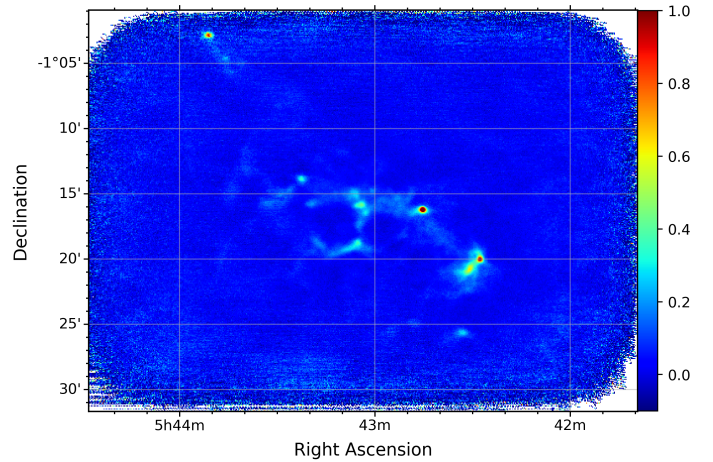
Fig. D.3. As Fig. D.1, but for the Ori B9 area (combining own observations with the data presented by Miettinen et al. (2009)).

Fig. D.1. APEX Laboca 870 μm dust continuum emission maps in L 1622. Brightness is given in units of Jy/beam. Contours (at 2, 4, 8, 16, and 32 Jy/beam) are used to represent the brightest features in the maps.

Fig. D.4. As Fig. D.1, but for the NGC 2023/NGC 2024 area.
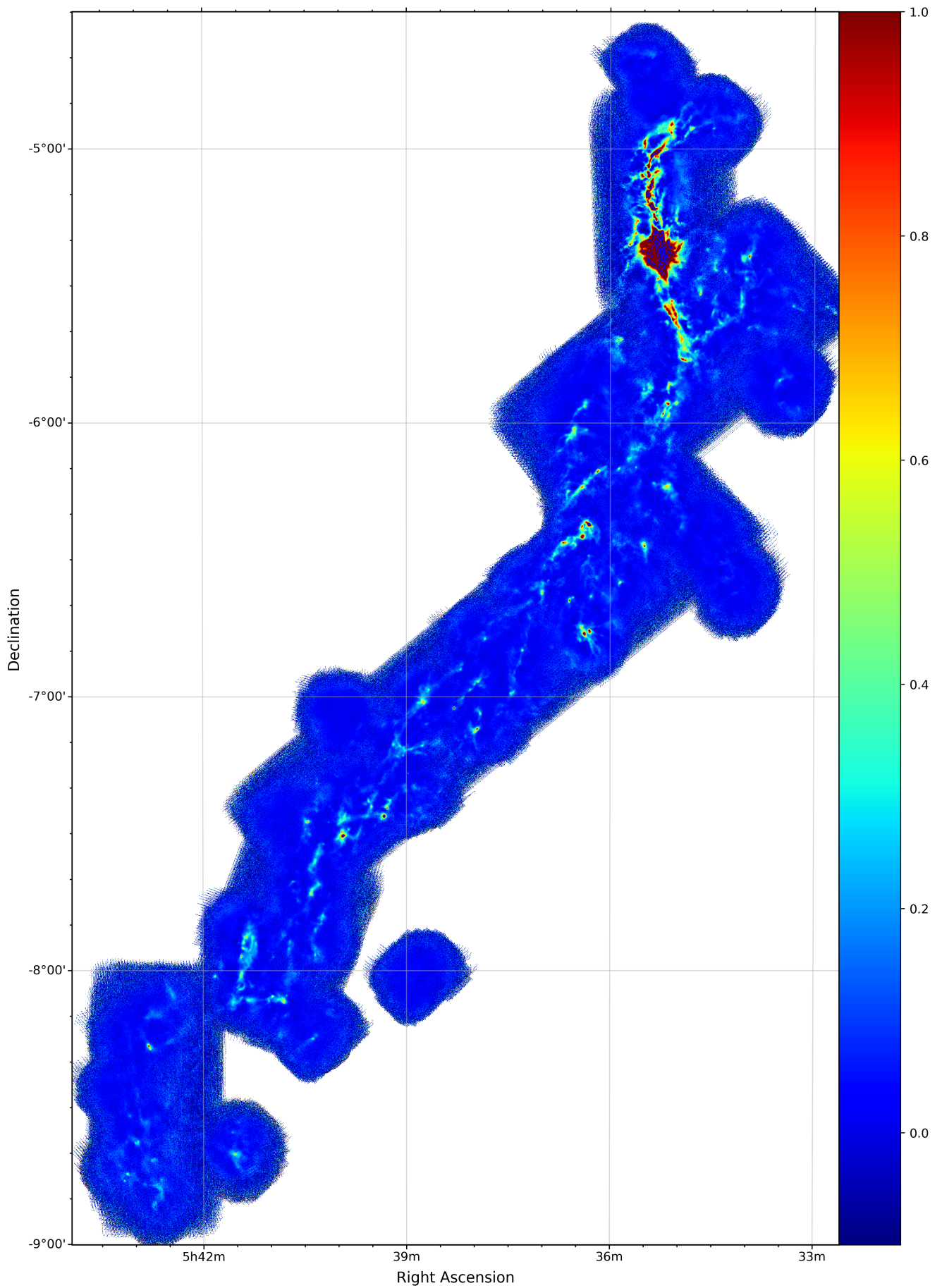
Fig. D.5. As Fig. D.1, but for Orion A (including the L 1641-S CO survey field in the south).